Development of triplet functional materials based on supramolecular chemistry

川嶋, 優介

Development of triplet functional materials based on supramolecular chemistry

Yusuke Kawashima

Department of Applied Chemistry
Graduate School of Engineering
Kyushu University

2023

Development of triplet functional materials based on supramolecular chemistry

Primary examiner: Associate Professor Nobuhiro Yanai

Secondary examiner:

Professor Tsuyohiko Fujigaya

Professor Nobuo Kimizuka

A thesis submitted in fulfillment of the requirements
for the degree of Doctor of Philosophy

in

Department of Applied Chemistry, Graduate School of Engineering
Kyushu University

September 2023

KYUSHU
UNIVERSITY

Preface

The research described herein was conducted under the supervision of Associate Professor Nobuhiro Yanai and Professor Nobuo Kimizuka in the Department of Applied Chemistry, Graduate School of Engineering, Kyushu University, between April 2017 and March 2022.

This thesis should be of interest due to the unique properties of photo-excited triplet states, especially triplet-triplet annihilation-based photon upconversion (TTA-UC), triplet dynamic nuclear polarization (triplet-DNP) and singlet fission (SF). In the field of physics, many phenomena related to excited triplet states have been studied. However, most of them have been studied only fundamentally. To overcome this situation, molecular design from the viewpoint of supramolecular systems is essential to promote the functionality. I hope my research provides an important initial step towards the practical use of TTA-UC, triplet DNP and SF.

Acknowledgements

Foremost, I would like to thank Professor Nobuo Kimizuka who guided me and continuously encouraged me in the past six years. I am grateful to him for introducing me to the wonders of scientific research and providing excellent research facilities and an outstanding research ambiance. Notably, I learned how to design molecular structures with remarkable functionality for molecular systems. I believe it is one of the original things I learned in Kimizuka Laboratory. And I warmly thank him for his precious advice, criticism and discussions on my work.

I am deeply indebted to Associate Professor Nobuhiro Yanai for providing invaluable guidance throughout my research. I got unique opportunity to learn how to set up a completely new research topic. And his diligent effort and training were the stepping stone behind each and every success I achieved, and will undoubtedly remain the prime asset for my future research.

My sincere thanks also go to Professor Teppei Yamada, Professor Shigenori Fujikawa and Assistant Professor Masa-aki Morikawa. They gave me a lot of advices and suggestions at every step of my research.

I express great gratitude to Associate Professor Kiyoshi Miyata Professor Ken Onda (Department of Chemistry, Kyushu University), Professor Go Watanabe (School of Frontier Engineering,, Kitasato University), Professor Yasuhiro Kobori (Molecular Photoscience Research Center and Department of Chemistry, Graduate School of Science, Kobe University), Dr. Tomohiro Uesaka and Dr. Kenichiro Tateishi (Cluster for Pioneering Research, RIKEN, RIKEN Nishina Center for Accelerator-Based Science) for their piercing suggestions and valuable discussions during the collaborations.

The computations were partially performed at the Research Center forComputational Science, Okazaki, Japan (Project: 21-IMS-C043, 22-IMS-C043). This work was partly supported by JSPS KAKENHI grant number(JP17H04799, JP16H06513, JP17H06375, JP19H02537, JP19H05718, JP19K15508, JP20H05106, JP20H02713, JP20K21211, JP22K19051 JP20H05676, JP19H00888,JP20H05831, JP22J21293, JP21J13049 and JP20J12469), and the JST-PRESTO program on “Creation of Life Science Basis by Using Quantum Technology” (JPMJPR18GB), JST-FOREST Program (JPMJFR201Y), the Sumitomo Foundation, the Shinnihon Foundation of Advanced Medical Treatment Research, the Innovation inspired by Nature Program of Sekisui Chemical Co., RIKEN-Kyushu Univ Science and Technology Hub Collaborative Research Program, the RIKEN Cluster for Science, Technology and Innovation Hub (RCSTI), and the RIKEN Pioneering Project “Dynamic Structural Biology". Kyushu University Platform of Inter-/Transdisciplinary Energy Research(Q-PIT) through its “Module-Resarch Program.”

I would like to thank Technical staff Kazumi Matsuno, Ryo Maeda, Azusa Suematsu and Chihoko Fukakusa for their warm solicitudes. I sincerely appreciate Professor Tuyohiko Fujigaya for reviewing this thesis.

The author wishes to express his gratitude to Dr. Joseph Ka Ho Hui, Dr. Kouta Masutani, Dr. Rakesh Kumar Gupta, Dr. Pankaj Bharmoria, Dr. Biplab Joarder, Dr. Tejwant Singh, Dr. Arijit Mallick, Dr. Gurbir Singh, Dr. Baljeet Singh, Dr. Taku Ogawa, Dr. Kazuma Mase, Dr. Hisanori Nagatomi, Dr. Masaya Matsuki, Dr Masanori Hosoyamada, Dr. Shota Hisamitsu, Dr. Yimin Liang, Mr. Tsubasa Kashino, Dr. Hironori Kouno, Dr. Ryosuke Yamamoto, Dr. Keisuke Okumura, Mr. Shinya Uchino, Mr. Hirotaka Ohara, Dr. Yoichi Sasaki, Ms. Hanyu Yang, Mr. Toshiki Eguchi, Mr. Yuki Nagai, Ms. Nao Hirakawa, Mr. Saiya Fujiwara, Mr. Junji Miyano, , Ms. Fan Gao, Ms. Risa Okeda, Ms. Mika Kinoshita, Mr. Takashi Kobayashi, Mr. Tetsuro Kobayashi, Mr. Keisuke Hayashi, Ms. Rena Haruki, Mr. Koki Nishimura, Mr. Hirotaka Inoue, Ms. Risa Iwami, Ms. Mone Sakata, Mr. Yuichiro Seki, Mr. Naoyuki Harada, Ms. Kana Orihashi, Ms. Mio Koharagi, Mr. Donggyu Kwak, Mr. Issei Maruyama, Ms. Kanae Izumi, Mr. Jumpei Kondo, Mr. Kentaro Tanaka, Mr. Ryoichi Tomomatsu, Mr. Tomoyuki Hamachi, Mr. Fumitoshi Matoba, Mr. Akio Yamauchi, Ms. Naura Fakhira Antariksa, Ms. Hikari Ishihara, Mr. Masanori Uji, Ms. Tae Tamemoto, Mr. Udai Danyoshi, Ms. Yuka Masunaga, Mr. Naoto Matsumoto, Mr. Mai Lam Bac, Mr. Keita Sakamoto, Mr. Kodai Matsumoto, Mr. Reiya Yabuki, Mr. Yuta Yamanaka, Mr. Yuya Watanabe for warm supports and discussion.

Dr. Hironori Kouno has been great mentors to me. I received kind guidance of not only experimental technique but also the way to proceed research. I would be happy if I could pass on as much as I can of what you taught me to the younger students in our lab.

My family have furthermore contributed to this publication. I thank my grandparents Toshiko Kawasihma and Sueko Nakashige and my younger sister Yuka Kawashima and my dogs, Haru and Marron for their continuous support and encouragement. Last but not least, I would like to pay my regards to my parents Koji Kawashima and Naoko Kawashima, who have truly encouraged me in my life.

Yusuke Kawashima
Department of Applied Chemistry
Graduate School of Engineering, Kyushu University
March 2023

Contents

Chapter3
Singlet fission as a polarized spin generator for dynamic nuclear polarization 59

Chapter 1

Photo-excited triplet states and functions derived from their unique properties

1-1 Introduction of photo-excited triplet state

・1-1-1 Introduction

In recent years, various functions based on the unique properties of photoexcited triplet states have attracted much attention. Photon upconversion based on triplet-triplet annihilation (TTA-UC),[1-15] dynamic nuclear polarization based on triplet states (triplet-DNP),[16-23] and singlet fission (SF)[24-26] are typical examples. In this thesis, we describe the development of novel supramolecular materials that express these unique functions.

・1-1-2 Photo-excited triplet state

Organic molecules can be in various states depending on the energy of their electrons and the orientation of their spins (Figure 1-1).[27, 28]

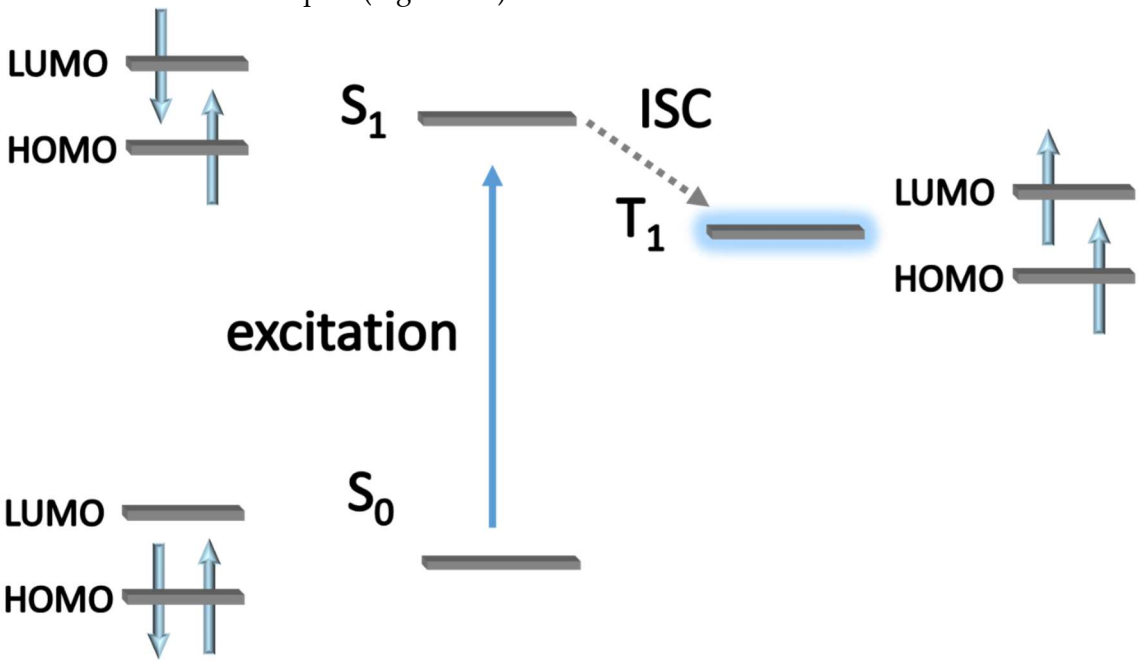

Figure 1-1. Energy diagram of photo-excited organic molecules.

In many molecules, based on Pauli's exclusion principle, the orientations of the electron spins in the highest occupied molecular orbital (HOMO) cancel each other in the ground state. This is called the ground singlet state and is denoted as S_0. When the molecule is excited from S_0, an electron is located in the lowest unoccupied molecular orbital (LUMO), but since the electron is in two different orbits, HOMO and LUMO, it can take two states depending on the spin orientation. The state in which the spin orientations cancel each other is called

the excited singlet state, and the lowest energy state among the excited singlet states is denoted as S_1. The state in which the spin orientations do not cancel each other is called an excited triplet state, and the lowest energy state among the excited triplet states is denoted as T_1. Since the excited triplet state has various unique properties as shown below, it has attracted attention for a wide variety of applications.

・1-1-3 Unique properties of excited triplet states

A common mechanism for the formation of excited triplet states is the intersystem crossing (ISC) from the excited singlet state S_1, since the direct transition from S_0 to T_1 is generally forbidden and rarely occurs. The same can be said for the deactivation of T_1 to S_0. For example, the lifetime of phosphorescence generated by the inactivation of T_1 to S_0 is much longer than that of fluorescence, which is the emission from S_1. Thus, the long lifetime due to the forbidden transition to S_0 is a key feature of the excited triplet state, which has the great advantage of holding the excitation energy for a longer time (Figure 1-2). For example, TTA-UC process, described below, takes advantage of this long lifetime.

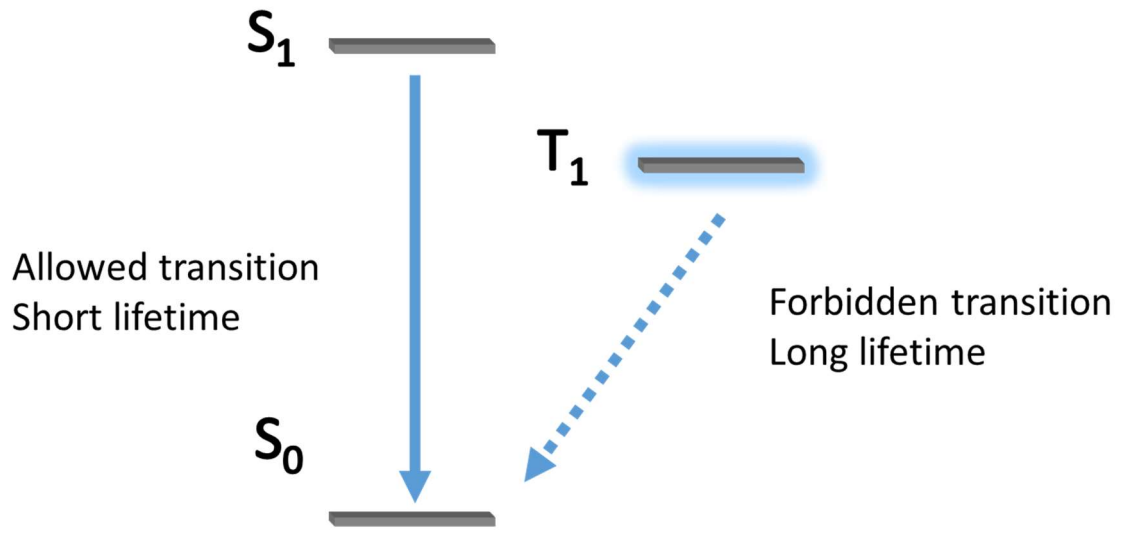

Figure 1-2. Lifetime of S_1 and T_1

Since the transition from S_1 to S_0 is allowed, the lifetime of S_1 is short, while the transition from T_1 to S_0 is forbidden, and the lifetime of the excited triplet state is generally longer than that of the singlet state.

Furthermore, the triplet state, as the name implies, is further subdivided into three states with slightly different energies depending on the combination of the spin orientations of the two electrons. Such fine levels are called sub-levels, and the energy difference between sub-levels of triplet electrons in a static magnetic field corresponds to the wavelength range of microwaves, making ESR observation possible.[27]

Magnetism is a property derived from the spin orientation of electrons and atomic nuclei. For example, in the energy level of iron, magnetism occurs when the electrons are arranged so that their spins are aligned on the condensed *d*-orbitals. Furthermore, it is known that oxygen molecules, which are triplet in the ground state, have paramagnetism derived from two electrons with aligned spins as well. In the excited triplet state, magnetism is expressed in exactly the same way as in iron and oxygen molecules, but unlike these materials, which have magnetism in the ground state, magnetism is observed only in the excited state and is lost by deactivation. This can be considered as a great advantage of the fact that the magnetism can be turned on and off at will by excitation. In addition, because of the non-equilibrium magnetism of the excited state, the spin orientation in the excited triplet state is biased independent of temperature, unlike the equilibrium state, and this non-equilibrium electronic spin polarization is utilized in triplet-DNP (Figure 1-3).[27, 29]

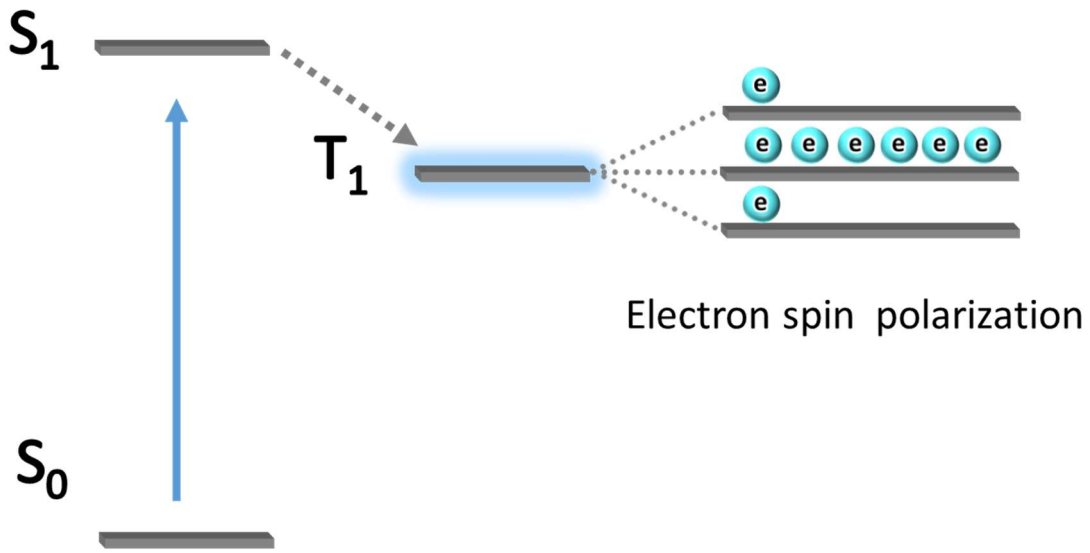

Figure 1-3. Electron spin polarization of T_1. Spin-selective intersystem crossing generates electron spin polarization in the excited triplet state. This spin-polarized state is not in equilibrium and is independent of temperature.

On the other hand, it is known that the triplet state is deactivated in the presence of oxygen.[30, 31] Oxygen molecules are known to have a triplet state T_0 in the ground state, which transitions to S_1 and S_2 upon excitation. It is known that the energy gap between T_0 and S_1 of oxygen molecules is 762 nm, and that between T_0 and S_2 is 1274 nm, which are smaller than the energy gap between S_0 and T_1 of many organic molecules.[32, 33] Therefore, it is easy to receive energy from molecules in the excited triplet state, which acts as a deactivation path for T_1. In addition, the oxygen molecules in the excited singlet state that receive energy in this process are highly reactive and oxidize the surrounding molecules. Because the excited

triplet state is easily lost in the presence of oxygen molecules due to these two processes, experiments using the triplet state are usually performed under conditions where deaeration is used to remove oxygen or in solids where oxygen does not diffuse, where deactivation does not occur.

As described above, the excited triplet state has various unique energetic and magnetic properties due to its spin, and because it is an excited state, it has the advantage of being able to be controlled by light irradiation. In the next section, we will introduce the various functions that are possible by utilizing this property.

1-2 Photon upconversion based on triplet-triplet annihilation

・1-2-1 Photon upconversion

Photon upconversion is a technique that converts low-energy light into higher-energy light by collecting the energy of multiple photons. In ordinary light-emitting processes such as fluorescence and phosphorescence, only light with lower energy than the incident energy is emitted due to energy loss, and the conversion of light wavelength is a one-way process from short wavelength to long wavelength. Photon upconversion, on the other hand, enables optical wavelength conversion in the opposite direction, making it possible to control optical energy freely and use it efficiently. Photon upconversion methods such as photon upconversion based on triplet-triplet annihilation (TTA-UC),[1-15] two-photon absorption,[34, 35] and multi-step excitation of rare earths[36-38] are known. Photon upconversion has been applied in a wide range of fields. For example, photon upconversion can be used to solve energy problems such as increasing the efficiency of photocatalysts and solar cells by expanding their usable wavelength range, and it is also expected to be applied to biological fields such as bio-imaging, photodynamic therapy, and optogenetics by converting the wavelength of near-infrared light, which has better penetration ability to biological tissues than visible light. Thus, the conversion of light energy is a useful technology that can be the basis of a wide range of fields.

An important factor in the practical application of photon upconversion is the intensity of excitation light that can be upconverted. If we consider the use of sunlight or light transmitted through a living body for upconversion, we will have to use excitation light on the mW/cm^2 scale. However, mechanisms such as multi-step excitation of rare-earth elements and two-photon absorption, which have been used in conventional photon upconversion, require the use of intense excitation light on a scale more than a thousand times larger (Figure 1-4)[9, 39] The reason for this is the low probability of the two-photon absorption and the low absorption coefficients of the rare-earth elements.

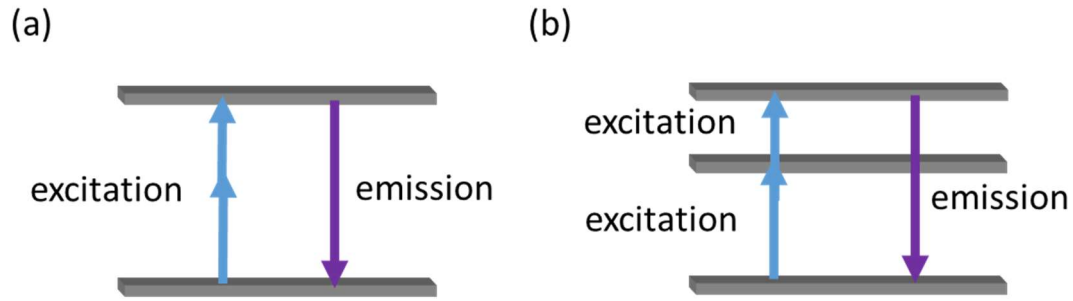

Figure 1-4. (a) mechanism of two-photon absorption,(b) multi-step excitation

TTA-UC is a photon upconversion mechanism consisting mainly of donor and acceptor components. The mechanism of TTA-UC is shown in Figure 1-5.

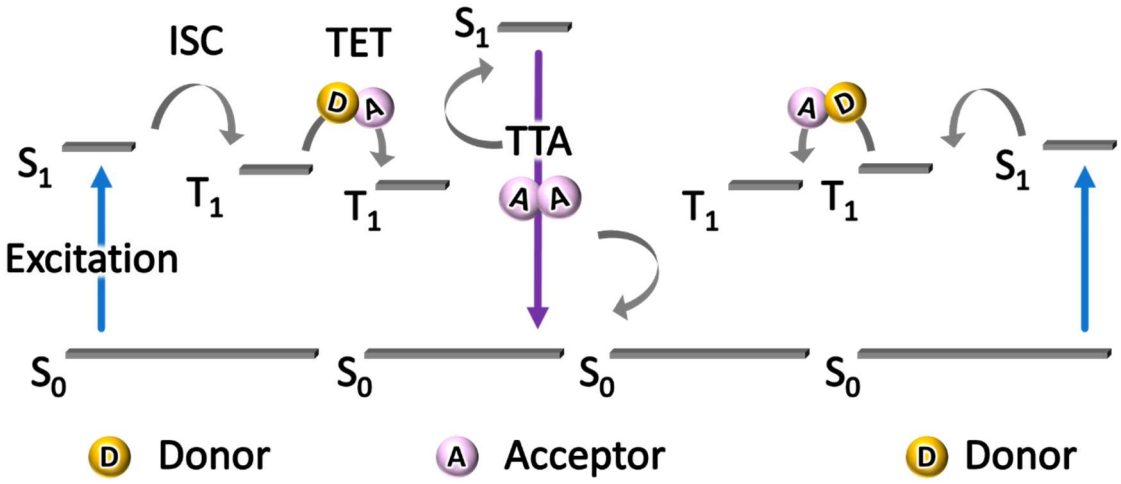

Figure 1-5. Mechanism of TTA-UC

1. Generation of donor T_1 by intersystem crossing (ISC) via S_1 generated by photoexcitation
2. Generation of T_1 of acceptor by triplet energy transfer (TET) from donor to acceptor
3. Generation of acceptor's S_1 and fluorescence by TTA between acceptors in the excited triplet state

---

By following the three steps described in Figure 1-5, the energy of two excited singlet states of the donor is converted to the excited singlet state of the acceptor, and the fluorescence from the acceptor is obtained. Triplet-triplet annihilation (TTA) is one of the deactivation processes of the excited triplet state, in which the excited singlet state S_1 and the ground singlet state S_0 are generated by the collision of two triplet excitons. Since TET and TTA are energy transfer processes based on the Dexter mechanism, the involved molecules must locate sufficiently close to each other. By setting the S_1 of the acceptor higher than the S_1 of the donor, it is possible to obtain light emission with higher energy than the incident light.

One of the advantages of TTA-UC is the wide variety of dyes that can be used as donor and acceptor. By selecting the appropriate combination of donor and acceptor, upconversion can occur at various wavelengths, making it possible to efficiently use light at various wavelengths according to the purpose, such as near-infrared light, which is permeable to living organisms, and ultraviolet light, which is necessary for photocatalysts.

・1-2-2 Brief history of TTA-UC

The mechanism of TTA itself has been known since the 1960s, but at that time it was only recognized as one of the main deactivation processes of the triplet state.[40] Starting with the report of highly efficient TTA-UC in solution systems,[1, 2, 4, 9, 41] various donor-acceptor combinations were reported. In addition to TTA-UC within the visible range, research has developed into more practical wavelengths such as near-infrared light to visible light and visible light to ultraviolet light.[42-44] In recent years, various donors have been developed with the aim of minimizing the energy loss due to the intersystem crossing of donor and maximizing the energy gain by UC, which has been a problem in these wavelength systems. Molecules exhibiting thermally activated delayed fluorescence (TADF)[45-47], inorganic material-based donors[48-53], and heavy metal complexes capable of direct excitation from S_0 to T_1[54, 55] are typical examples.

Schmidt et al. reported dye-sensitized solar cells with extended wavelength range by using TTA-UC.[56] Hanson et al. sensitized solar cells by TTA-UC using dyes arranged on metal oxide surfaces.[13] Castellano et. al. and Monguzzi et al. have reported highly efficient photocatalytic reactions using TTA-UC,[57, 58] and Campos et al. have reported photo-redox catalysis using TTA-UC.[59] These are mainly applications in the energy field, but many applications in the biological field have also been reported.

Since components that exhibit upconversion luminescence do not normally exist in living organisms, bioimaging using upconversion materials will enable imaging with a high signal-to-noise ratio. In addition, in the field of optogenetics, light with wavelengths shorter than 500 nm is necessary,[60] but these cannot penetrate biological tissues, which makes the experimental system bioinvasive. By converting the biotransparent near-infrared light into these shorter wavelengths using TTA-UC, these problems can be solved and a non-invasive experimental system can be constructed.

・1-2-3 Principle and parameters of TTA-UC

In TTA-UC, the quantum yield, which is the ratio of the number of photons originating from UC emission to the number of incident photons, is at most 50% because TTA-UC is a process consisting of two photons. In many papers, the quantum yield of TTA-UC, Φ_{UC}, is multiplied by 2 to express the TTA-UC efficiency Φ'_{UC} with the theoretical maximum of 100%. Φ'_{UC} is expressed as the product of the quantum yields of each process in TTA-UC as in the following equation,[2, 4]

$$\Phi_{UC}' = 2\Phi_{UC} = f\Phi_{ISC}\Phi_{TET}\Phi_{TTA}\Phi_{F,A} \quad (equation\ 1)$$

where Φ_{ISC}, Φ_{TET}, Φ_{TTA}, $\Phi_{F,A}$, and f are defined as follows, respectively

Φ_{ISC} : Intersystem crossing efficiency of donor
Φ_{TET} : Triplet energy transfer efficiency from donor to acceptor
Φ_{TTA} : TTA efficiency between acceptors in the T_1 state
$\Phi_{F,A}$: fluorescence quantum yield of acceptor
f : Probability that S_1 of acceptor is generated by TTA

One of the greatest advantages of TTA-UC is that it can be used even with light as weak as sunlight; in TTA-UC, the energy from the incident light is retained in the form of an excited triplet state T_1 of the acceptor. As mentioned above, the transition from T_1 to S_0 is forbidden because it involves spin flipping and T_1 has a long lifetime of μs to ms. This means that the photon energy is retained for such a long time, and hence the probability for T_1 of meeting each other within the excited lifetime is high. Therefore, in TTA-UC, fewer photons, i.e., lower intensity light, can be used to generate upconversion emission compared with other mechanisms. As mentioned above, this is a great advantage for the actual application of the photon upconversion phenomenon in various technologies.

Therefore, the most important factor in the practical application of TTA-UC is how low the intensity of the excitation light is to obtain UC emission. The value of I_{th} is defined as an index of the intensity of the excitation light at which $\Phi_{TTA} = 0.5$. In the low excitation intensity region where there are few acceptors of the T_1 state in the system, the UC emission intensity is proportional to the square of the excitation intensity. On the other hand, in the region where the excitation light intensity is sufficiently high, the UC intensity changes linearly because there are many acceptors of the T_1 state in the system and TTA is likely to occur. These behaviors can be expressed by the following rate equations for each excited state,[61, 62]

$$\frac{\partial T_D}{\partial t} = \alpha I_{exc} - k_D^T T_D - k_{tr} T_D$$

$(equation\ 2-1)$

$$\frac{\partial T_A}{\partial t} = k_{tr} T_D - k_A^T T_A - \gamma_{TTA} T_A^2$$

$(equation\ 2-2)$

$$\frac{\partial S_A}{\partial t} = 0.5 f \gamma_{TTA} T_A^2 - k_A^S S_A$$

$(equation\ 2-3)$

where T_D, T_A, and S_A are the concentrations of donor T_1, acceptor T_1, and acceptor S_1, respectively. α is the absorption coefficient of the donor, I_{exc} is the excitation light intensity, k is the rate constant of each process, and γ_{TTA} is the rate constant of TTA.

Since TTA is inferior as an acceptor deactivation process in the excited triplet state in the weak excitation light intensity region, we can assume that $\gamma_{TTA} T_A^2 \gg k_A^T T_A$. By modifying the above equation based on this assumption, we can see that S_A is proportional to the square of the excitation light intensity, which is expressed by the following equation,

$$S_A = 0.2 \frac{\gamma_{TTA}}{k_A^S} \left[\frac{\frac{k_{tr}}{k_A^T}}{k_D^T + k_{tr}} \right]^2 [\alpha I_{exc}]^2 \propto I_{exc}^2$$

$(equation\ 3)$

On the other hand, when the excitation light intensity is sufficiently strong, TTA becomes the dominant process for the deactivation of the acceptor in the triplet state, and it can be regarded as $\gamma_{TTA} T_A^2 \gg k_A^T T_A$. Based on this assumption, the S_A can be described as follows:

$$S_A = 0.2 \frac{1}{k_A^S} \left[\frac{k_{tr}}{k_D^T + k_{tr}} \right]^2 \alpha I_{exc} \propto I_{exc}$$

$(equation\ 4)$

In the region where the excitation light intensity is strong, the UC emission intensity is proportional to the excitation light intensity.

The excitation light intensity at which the equations based on the equations 4 and 5 are equal is defined as I_{th}, and I_{th} is expressed as the following equation (Figure 1-6),[63]

$$I_{th} = \frac{1}{\alpha \Phi_{TTET} \gamma_{TTA} \tau_{A,T}^2} = \frac{1}{8\pi a_0 \alpha \Phi_{TTET} D_T \tau_{A,T}^2}$$

$(equation\ 5)$

where a_0 is the distance at which TTA occurs and D_T is the exciton diffusion coefficient, and $\gamma_{TTA} = 8\pi a_0 D_T$ for the three-dimensional diffusion system. From the above equation, we can see that I_{th} is highly dependent on the triplet lifetime of the acceptor. The longer the triplet lifetime, the lower the I_{th}, which is a measure of the excitation light intensity at which UC emission can be efficiently obtained, and the more practical the system is. In the most efficient system, the I_{th} value is on the scale of several mW/cm^2, which is about the same as the intensity of sunlight on the ground.

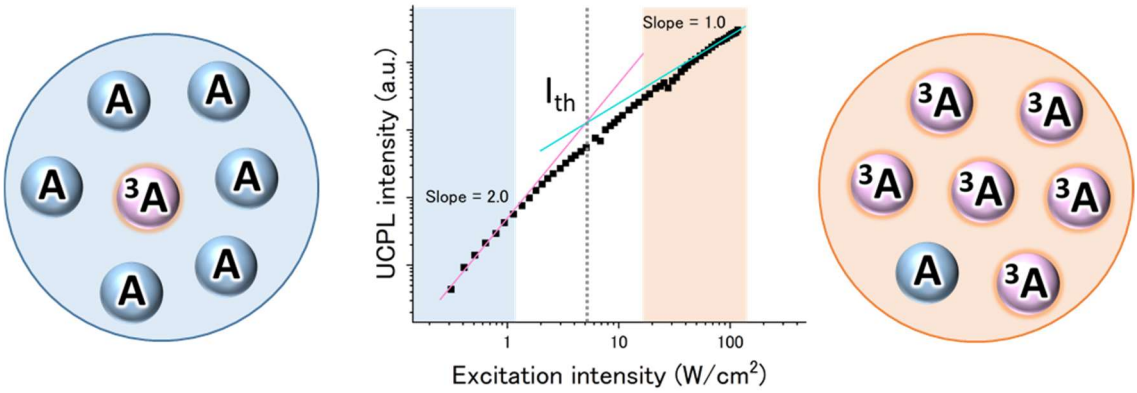

Figure 1-6. Typical excitation intensity of upconversion in a triplet-triplet annihilation-based upconversion mechanism. In the region of slope = 2.0, there are few acceptors in the T_1 state, and in the region of slope = 1.0, most of the acceptors are in the T_1 state.

Thus, TTA-UC enables photon upconversion with weaker light than the conventional method by taking advantage of the long lifetime characteristic of the triplet state and the deactivation process called TTA, which is desired for practical use.

・1-2-4 Deployment of TTA-UC in aqueous systems

TTA-UC is expected to be applied to a variety of aqueous systems, including bio-imaging and photocatalytic reactions. For such applications, it is inevitable that TTA-UC must be performed under atmospheric conditions, where oxygen coexists.

However, it is known that the triplet state is deactivated by oxygen in the presence of oxygen. Therefore, TTA-UC is usually carried out under degassed conditions. Two main strategies are known to prevent oxygen quenching: the first is the addition of molecules that act as oxygen quenchers,[39, 64 65-68] and the second is the use of physical barriers such as highly viscous solvents or polymers to suppress oxygen diffusion.[3, 30, 31]

Based on the first strategy, Fuyou Li et al. succeeded in performing TTA-UC in vivo using

nanocapsules doped with biocompatible oxygen quenchers such as oleic acid and limoneic acid, and demonstrated the bioimaging of mice.[64] Kim et al. reported TTA-UC in hexadecane/polyisobutylene microcapsules,[3, 69] and Monguzzi et al. reported TTA-UC in micelles.[70]

However, these systems rely on molecular diffusion for the triplet state diffusion, and the efficiency of TTA-UC is intrinsically limited by the viscosity of the solvent.

1-3 Nuclear Magnetic Resonance (NMR) and Its Applications

・1-3-1 Brief history of Nuclear Magnetic Resonance

In a static magnetic field, particles with spins such as electrons and atomic nuclei are divided into those with spins parallel to the magnetic field and those with spins opposite to the magnetic field, and their energy levels are slightly split according to their orientation. This phenomenon is known as Zeeman splitting. Nuclear magnetic resonance (NMR) is a resonance phenomenon between the energy levels of Zeeman-split nuclei, which was first observed by Purcell and Bloch in 1945[71] [72].

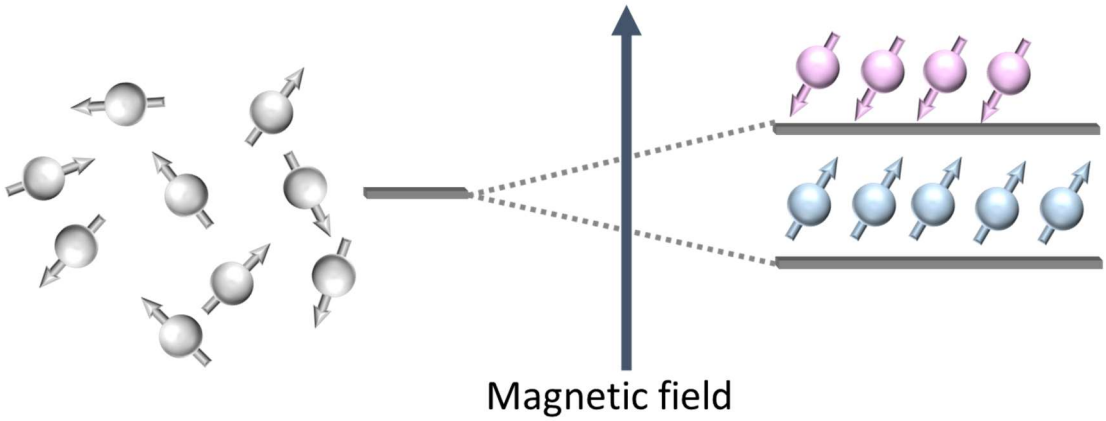

Figure 1-7. Schematic illustration of Zeeman splitting.
In the absence of a magnetic field, the spins are randomly oriented and there is only one energy level, but in a static magnetic field, the spins are aligned in parallel and anti-parallel to the magnetic field, and the energy levels are split due to the orientation of the spins.

The NMR signal contains two pieces of information: one is the frequency, which corresponds to the energy range of the Zeeman splitting, and the other is the relaxation time, which is the timescale on which the NMR signal is decaying. Since this information depends on the type of nucleus, the environment, and the strength of the magnetic field, it is possible to analyze the surrounding structure of the target at the atomic level by observing and analyzing NMR. For example, it is possible to analyze the molecular structure of a sample by applying a uniform magnetic field to the entire sample and observing the subtle shifts that vary depending on the environment of the nuclei, and this technique was established by Arnold et al. in 1951 as NMR spectroscopy[73] Furthermore, it is possible to perform NMR imaging by applying different magnetic fields to the sample according to space and analyzing the relaxation time for each spatial coordinate. It is now widely used in the medical field as nuclear magnetic resonance imaging (MRI)[74].

・1-3-2 Magnetization transfer and multidimensional NMR

In NMR spectroscopy, the phenomenon of magnetization transfer enables us to analyze not only the information surrounding the nucleus to be measured, but also the interaction between the nuclei. Magnetization transfer is a phenomenon in which radiofrequency irradiation causes an exchange of energy corresponding to the Zeeman splitting width between nuclei through magnetic interaction (Figure 1-8). The mechanism of magnetization transfer is known as the nuclear Overhauser effect (NOE)[75] and cross polarization (CP)[76 77], but they all have one thing in common: for magnetization transfer to occur, the nuclides must be in close proximity on the scale of a few Å. In other words, it is possible to discriminate between nuclei in close proximity by observing the magnetization transfer, and this technique has been applied as multidimensional NMR.[78,79]

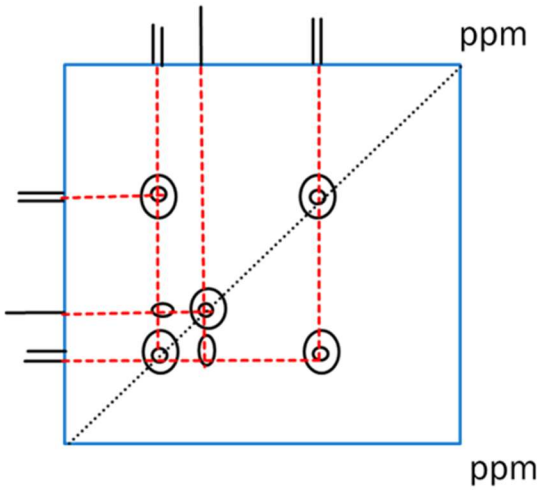

Figure 1-8. Typical two-dimensional NMR spectrum. The detection of cross peaks allows for more detailed structural analysis.

In 1986, Wuthrich et al. applied NMR spectroscopy to protein structure analysis, and NMR spectroscopy became a powerful tool in the field of molecular biology.[80] X-ray diffraction is widely used as a method for analyzing protein structures, but it only analyzes the structure in the crystalline state. On the other hand, structural analysis by NMR can be performed even in aqueous solution, making it possible to analyze protein structures in an environment closer to that of living systems. A further development is in-cell NMR, which was developed by Dötsch and his group in 2001.[81] Since in-cell NMR can analyze proteins in their active state, it can provide clues to the analysis of complex information networks composed of proteins in the cell. In-cell NMR is expected to provide clues to the analysis of complex information networks consisting of intracellular proteins. In particular, since the late 1990s, when the dynamic behavior of naturally denatured proteins, which do not have a specific

higher-order structure, was considered to be involved in the expression of more advanced cellular functions, there has been a strong demand to analyze the behavior of naturally denatured proteins using this technique. There is a strong need to analyze the behavior of naturally denatured proteins using this technique.[82] Thus, protein analysis by NMR has a great advantage over other analytical methods in that it allows us to see the behavior of proteins in their natural state, and it can be a very powerful tool for contributing to the development of molecular biology.

・1-3-3 Nuclear Magnetic Resonance Imaging (MRI)

MRI is a technique for non-destructive and detailed imaging of the interior of a sample using NMR. In MRI, a spatially inhomogeneous magnetic field is used to relate the Zeeman splitting width to spatial coordinates for imaging. The NMR signal contains not only the frequency but also the relaxation time, which varies depending on the environment in which the nucleus is placed, such as the structure of biological tissue (Figure 1-9).

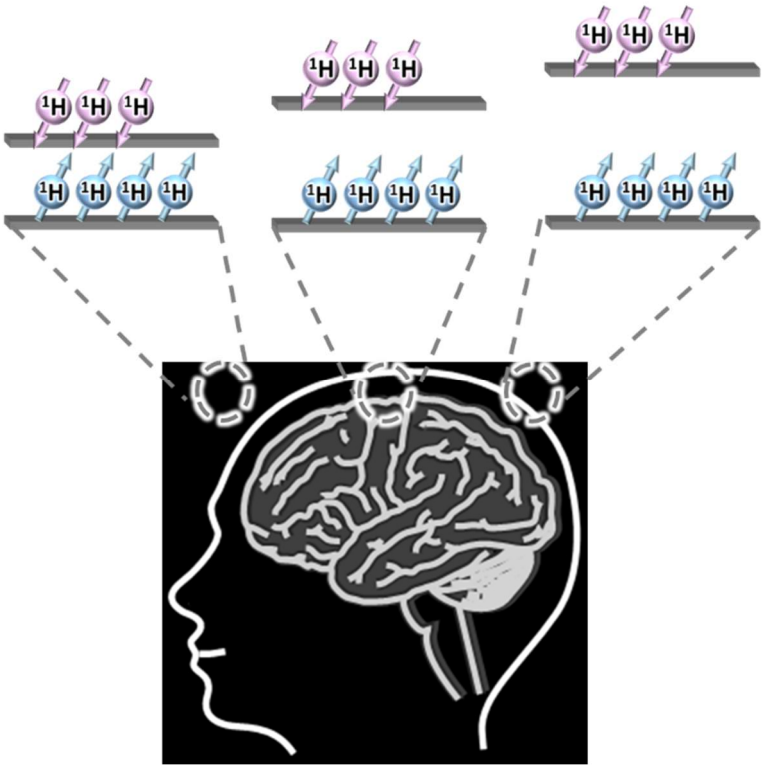

Figure 1-9. Schematic illustration of MRI. In MRI, NMR signals are observed for each coordinate using the difference in Zeeman splitting width caused by the inhomogeneous magnetic field. The state of the tissue is determined from the difference in relaxation time at each coordinate.

・1-3-4 Polarizing ratio

The sensitivity of NMR depends on the difference in the number of nuclear spins in the same direction as the magnetic field and those in the opposite direction. (Figure 1-10)

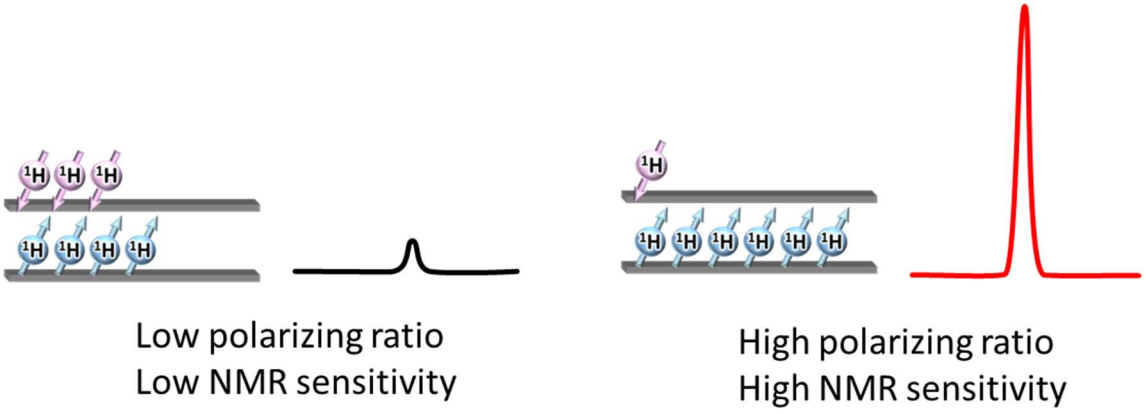

Figure 1-10. Relationship between polarizing ratio and NMR signal intensity. At low polarization ratio, the intensity of the NMR signal is weak, and the NMR signal intensity can be enhanced by increasing the polarizing ratio.

This value is called the polarizing ratio, and the polarizing ratio at thermal equilibrium condition, P_{th}, can be expressed using temperature T, magnetic field B, and gyromagnetic ratio γ, as in the following equation,[18]

$$P_{th} = \frac{N\uparrow - N\downarrow}{N\uparrow + N\downarrow} = \frac{exp\left(\frac{\gamma\hbar B}{2kT}\right) - exp\left(-\frac{\gamma\hbar B}{2kT}\right)}{exp\left(\frac{\gamma\hbar B}{2kT}\right) + exp\left(-\frac{\gamma\hbar B}{2kT}\right)} = \tanh\left(\frac{\gamma\hbar B}{2kT}\right)$$

$(equation\ 6)$

where $N\uparrow$ and $N\downarrow$ are the populations of the eigenstates $|+\frac{1}{2}>$ and $|-\frac{1}{2}>$, ħ is Dirac's constant and k is Boltzmann's constant. The polarizing ratio of ^{1}H nuclei at room temperature is known to be very low, less than one part in 100,000, and that of ^{13}C nuclei is even lower, with the natural abundance of the nucleus itself being as low as 1%, making detection difficult and requiring a large amount of integration. To solve this problem, ^{13}C NMR use the transfer of magnetization from ^{1}H to ^{13}C to increase the polarizing ratio and reduce the number of integration steps, thereby shortening the measurement time. However, since the polarization ratio of ^{1}H itself is low, a fundamental solution has not been reached. This problem is also inherent in MRI, and only ^{1}H nuclei of water molecules, which exist in large quantities in living organisms, are used for practical imaging.

・1-3-5 Dynamic Nuclear Polarization (DNP)

Dynamic nuclear polarization (DNP) is a method of NMR sensitization by increasing the polarization of nuclei through the transfer of magnetization from highly polarized electrons to nuclei by microwave irradiation. The existence of the Overhauser effect was theoretically predicted in 1953 and demonstrated by Craver and Slichter within the same year.[83] The magnitude of the polarizability depends largely on a particle-specific value called the gyromagnetic ratio. The gyromagnetic ratio of a nucleus is the largest at the ^{1}H nucleus, but the gyromagnetic ratio of an electron is approximately 660 times larger than that of the ^{1}H nucleus (Figure 1-11).

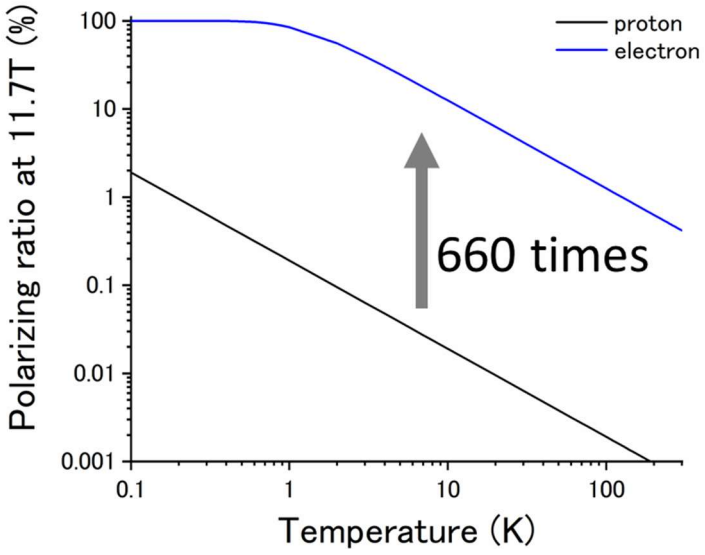

Figure 1-11. Polarizing ratio of proton and electron at thermal equilibrium state in a typical 500 MHz NMR spectrometer (11.7 T).

The use of dissolution-DNP, developed by Larsen et al. in 2003, has greatly expanded the range of applications of DNP.[84] This method involves freezing the polarizing agent and the polarization target, transferring the polarization by DNP, and then rapidly thawing them to a solution state. In this way, highly polarized materials can be obtained even in the solution state, and DNP can be used to increase the sensitivity of solution NMR and MRI.[85,86]

On the other hand, there are several problems with the conventional method of DNP. The occupation numbers of electrons and nuclei in the Zeeman level follow the Boltzmann distribution, i.e., the polarization ratio is affected by temperature. Therefore, if we want to increase the polarization ratio by biasing the occupation number in the thermal equilibrium state, we need a cryogenic state, which is a practical problem because it requires a large-scale apparatus. In addition, the theoretical limit of sensitivity for DNP using electrons in thermal

equilibrium is 660 times for ^{1}H nuclei. In addition, in order to increase the nuclear polarization by the transfer of magnetization from electrons to nuclei, the sum of the quantum numbers of the electron spins of the polarizing agent molecule must not be zero. In other words, the polarizing agent molecule must have unpaired electrons and be a paramagnetic species. In general, stable radicals such as TEMPO and its bound TOTAPOL are used as polarizing agents in DNP.[87] The free induced decay(FID) signal in NMR is expressed as follows,[88]

$$S(t) = S_0 \cos(\omega_0 t) e^{-\frac{t}{T_2}}$$

$(equation\ 7)$

where ω_0 is Larmor frequency, T_2 is the spin-spin relaxation time, which corresponds to the time when the coherence of the magnetization vector (the sum of the vectors of the nuclear spins in the system) is maintained. Fourier transforming this equation yields a Lorentzian spectrum of the form,

$$S(\omega) = \frac{\lambda}{\lambda^2 + (\omega - \omega_0)^2}$$

$(equation\ 8)$

where the line width of the spectrum is expressed as $2\lambda = \frac{2}{T_2}$. Therefore, as T_2 becomes shorter, the line width of the NMR spectrum increases. This causes problems such as difficulty in discriminating peaks and the inability to observe peaks.[89]

・1-3-6 Dynamic nuclear polarization using excited triplet state (triplet-DNP)

As an innovative DNP method that solves these problems, the dynamic nuclear polarization method using excited triplet state (triplet-DNP) devised by Deimling et al. in 1980 has recently attracted attention.[90] In triplet-DNP, molecules in the excited triplet state are used as the polarizing agent instead of radical in the thermal equilibrium. In some molecules, such as pentacene, the number of occupied Zeeman levels in the excited triplet state is biased, and in triplet-DNP, this electronic spin polarization is transferred to the nuclear spin by the transfer of magnetization (Figure 1-12).

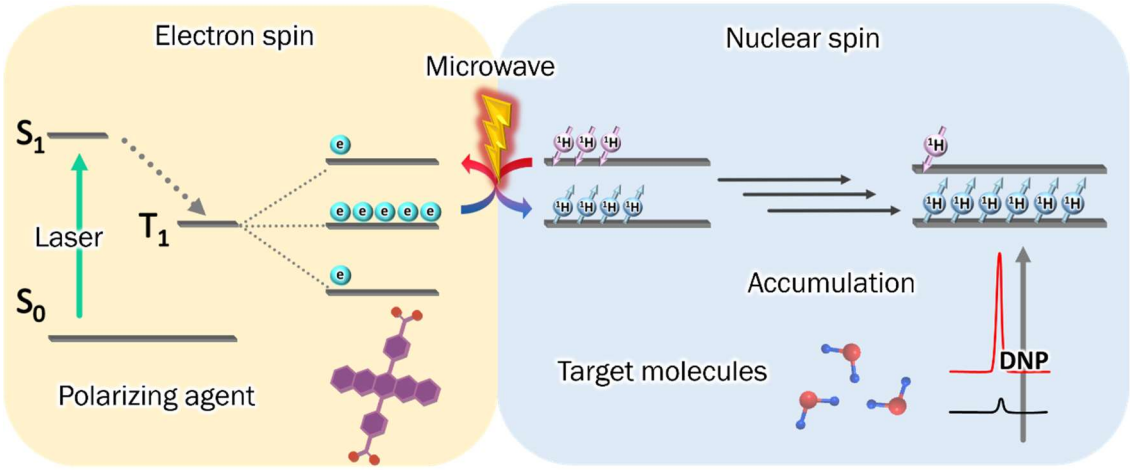

Figure 1-12. Mechanism of triplet-DNP

1. Generation of T_1 in the polarizing agent by intersystem crossing via S_1 generated by optical excitation.
2. Transfer of magnetization from the electron spins of the polarizing agent molecule to the nuclear spins of the polarization target by microwave irradiation.
3. Accumulation of polarization by repeating the above two processes.

Since the Zeeman order is equal between homogeneous nuclei, diffusion of the polarization state occurs, and by repeating this step, the entire system can be polarized.

・1-3-7 Parameter of triplet-DNP

In the process of polarization accumulation by triplet-DNP, the following differential equation is established, taking into account the build-up time constant T_B, which is the efficiency of accumulating the polarization, and the spin-lattice relaxation time T_1, which is a measure of the time in which the polarization can be retained.[91]

$$\frac{dP_H(t)}{dt} = \frac{1}{T_B}[P_e - P_H(t)] + \frac{1}{T_1}[P_H(t) - P_{H\,therm}\ \ ]$$

$(equation\ 9)$

The final polarization ratio in the system achieved by triplet-DNP is shown in this equation.

$$P_H(t) = P_f\left\{1 - exp\left[-\left(\frac{1}{T_B} + \frac{1}{T_1}\right)\right]t\right\}$$

$(equation\ 10)$

and P_f is defined by this equation. (Figure 1-13)

$$P_f = \frac{1}{1 + \frac{T_B}{T_1}}P_e$$

$(equation\ 11)$

This expression is valid under the fast diffusion limit where the polarization diffusion is sufficiently fast.[18]

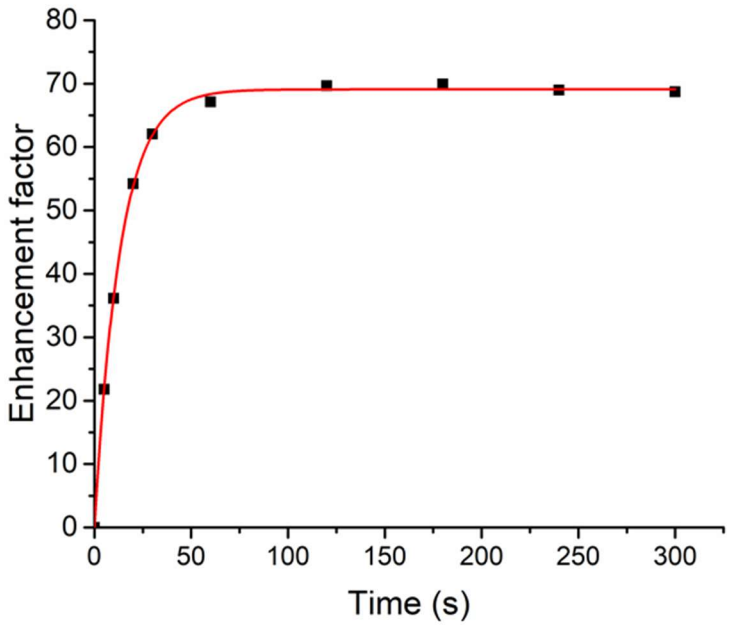

Figure 1-13. An example of build-up behavior.

The final enhancement factor is determined by the spin-lattice relaxation time (T_1), which is a measure of the ease of maintaining the polarized state of the sample, and the build-up rate (T_B), which is a measure of the efficiency of DNP.

The enhancement factor ε, which is the degree of signal enhancement, is expressed as follows,

$$\varepsilon = \frac{N_{ref}}{N_{DNP}} \frac{T_{DNP}}{T_{ref}} \frac{g_{ref}}{g_{DNP}} \frac{E_{DNP}}{E_{ref}}$$

$(equation\ 12)$

where N is the number of proton nuclei present in the system, T is the temperature, g is the receiver gain, and E is the recorded voltage.

In addition, this technique generally uses cross polarization (CP) as a principle for the transfer of polarization from electrons to nuclei. The magnetic field on each nucleus in the rotational coordinate system can be adjusted by varying the intensity of the radiofrequency irradiation that resonates with each nuclide. At this time, as shown in the following equation, by adjusting the intensity of the radiofrequency irradiation so that the chapter frequencies (Rabi frequencies) of the two nuclei in the rotational coordinate system coincide, the polarization diffuses in the same way as between homogeneous nuclei, and the magnetization can be shifted. The intensity condition is called the Hartmann-Hahn condition,

$$\omega_1 = B_1\gamma_1 = \omega_2 = B_2\gamma_2$$

$(equation\ 13)$

where ω_1, ω_2 is the Rabi frequency, γ_1, γ_2 is the gyro magnetic ratio, and B_1, B_2 is the magnetic field of nuclei 1 and 2, respectively.

For the transfer from electron to nucleus in Triplet-DNP, the method of integrated solid effect (ISE) or called as integrated cross polarization (ICP) is used for polarization transfer from electron to nuclei. In this method, the Hartmann-Hahn condition is satisfied between the Rabi frequency of the electron spins and the rotational frequency of the nuclear spins in the static magnetic field (Larmor frequency), which is expressed as follows,

$$\omega_{effe} = \omega_{0H}$$

$(equation\ 14)$

where $\omega_{effe} = \sqrt{\omega_{1e}^2 + \Delta\omega_e^2}$ is the effective magnetic field strength of the electron spin, ω_{1e} is the Rabi frequency of the electron spin, and $\Delta\omega_e$ is the offset frequency. The electron spins are broadened by the interaction with the nucleus, as shown by the ESR signal, and only a part of the electron spins with matching frequencies can undergo the polarization transfer.

To solve this problem, a method of sweeping the static magnetic field has been used.[92, 93] The sequence of triplet-DNP is as follows: after laser irradiation, microwaves resonating with electron spins are irradiated under the Hartmann-Hahn condition, and the static magnetic field is swept simultaneously (Figure 1-14).

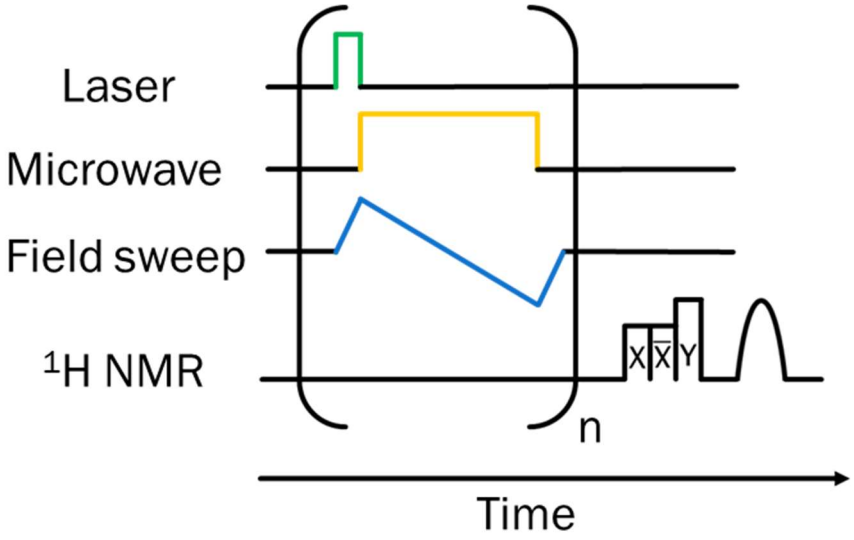

Figure 1-14. A typical DNP sequence.

After generating the excited triplet state by laser irradiation, the electron spin polarization is transferred to the nuclear spin by microwave irradiation with magnetic field sweep. After repeating this operation many times, the enhanced NMR signal is observed.

One of the greatest advantages of triplet-DNP is that the polarization of the electron spins in the triplet state, which is the source of the polarization, does not depend on the magnetic field or temperature (Figure 1-15). It is known that the mechanism of the generation of electron spin polarization in the triplet state is due to the difference in the speed of the intersystem crossing from S_1 to higher excited states such as T_2 and T_3.[94] Since the generation of electron spin polarization is a non-equilibrium process, it does not follow a Boltzmann distribution, unlike the electron spin of radicals. In 1990, Wenckebach et al. achieved 5,000-fold sensitization of NMR signals in pentacene-doped naphthalene crystals, and more recently, by doping pentacene in deuterated p-terphenyl crystals, a very large polarizing ratio of 30% was achieved at room temperature.[16, 20]

Another advantage of triplet-DNPs is that broadening of NMR due to paramagnetic relaxation can be suppressed. As mentioned above, in conventional DNP, paramagnetic species such as radicals are used as the polarizing agent. Therefore, paramagnetic relaxation of the polarized state always occurs in the system, resulting in broadening of the signal. On the other hand, in triplet-DNP, the excited triplet state, which is the polarizing agent, has a

microsecond lifetime and is immediately deactivated to the ground singlet state, losing its magnetism. Therefore, the magnetic relaxation is minimized not only during the measurement but also during the accumulation of the polarization.

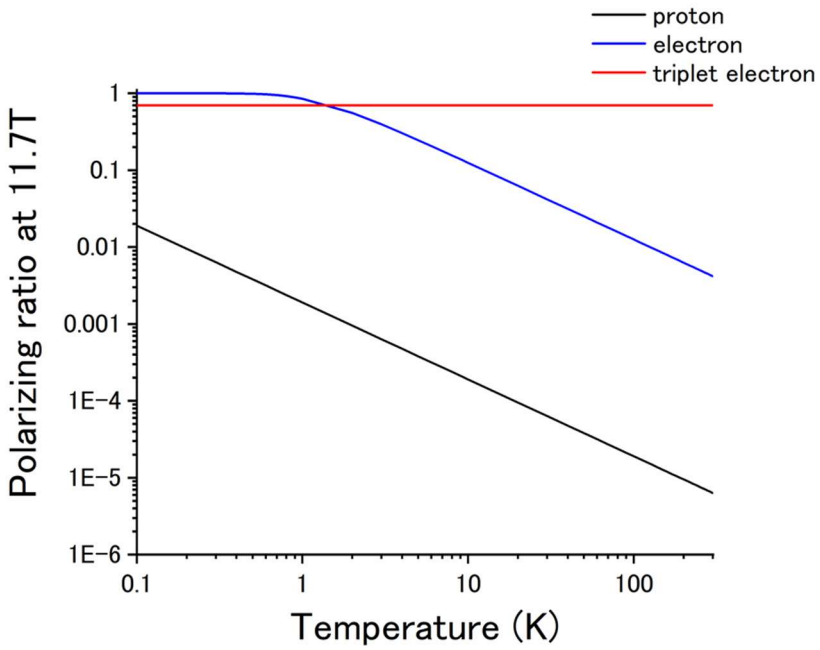

Figure 1-15. Polarizing ratio of electron of triplet state and proton and electron at thermal equilibrium state in a typical 500 MHz NMR spectrometer (11.7 T).

Thus, triplet-DNP can achieve high NMR sensitivity under conditions that are impossible with conventional methods, such as room temperature and low magnetic field. This advantage is essential for the wider application of DNP technology, and it is highly desirable to use this technique to highly polarize a variety of objects. In recent years, examples of the application of DNP have been reported, such as a system in which 5-fluorouracil with a ^{19}F nucleus is doped into a glass solid as a polarization target, and a system in which pentacene is incorporated into metal-organic framework (MOF), a porous solid in which the introduction of a polarization target guest is relatively easy.[19,95]

・1-3-8 Necessity of Application of Triplet-DNP in Water

The triplet-DNPs can be used to increase the sensitivity of NMR signals at room temperature without broadening by using the microsecond triplet lifetime of the excited triplet state and the non-equilibrium electron spin polarization between triplet sublevels. The application of triplet-DNPs is expected in fields such as protein behavior analysis and bioimaging using MRI.

As mentioned above, multidimensional NMR can be a very powerful tool for analyzing the higher-order structure of proteins. On the other hand, due to the low sensitivity of NMR,

long measurement times of several hours or even a day are currently required, which may lead to degradation of proteins and cells, and makes it difficult to analyze dynamic behavior through time-resolved measurements on the millisecond scale. In addition, it is difficult to analyze the dynamic behavior of proteins by time-resolved measurements on the millisecond scale. Using triplet-DNP to enhance NMR signals at room temperature would solve this problem and enable the analysis of the dynamic behavior of proteins in water and in cells, which is expected to bring great progress in these fields.

The problem of low NMR sensitivity is also prominent in MRI, and practical imaging is limited to the ^{1}H nuclei of water molecules, which exist in large quantities in the body. If DNP can be used to increase the sensitivity, it will not only provide clearer images, but also make it possible to image substances in the body other than water. For example, if pyruvate and its metabolites used in metabolic reactions in the body can be identified and imaged by each chemical shift, it will be possible to comprehensively track metabolic reactions in the body. This will allow for more multifaceted analysis, such as identifying areas of active metabolism, for example, cancer tumors.[96] Thus, it can be said that MRI has the potential to be more than just a non-destructive imaging technique, but also a revolutionary medical tool that can scan various substances in the body and detect abnormalities.

On the other hand, conventional DNP, which uses electrons in thermal equilibrium as a polarizing agent, requires the cryogenic temperatures of about 1 K to generate polarization, which requires a large and expensive device. Because of this problem, the application of DNP in the field of biology has been severely limited. If the dissolution-DNP described above can be performed at higher temperatures, such equipment will not be necessary, and the method will become more general. In this respect, there is a strong need to use triplet-DNP, which can achieve high sensitivity regardless of temperature. Furthermore, if triplet-DNPs can be used to achieve high polarization at room temperature, the process of freezing itself becomes unnecessary. This eliminates the need to dissolve the hyperpolarized material and inject it into the measurement target, which is conventionally done with dissolution-DNP. In other words, DNP can be performed in living cells or even in vivo.

Thus, triplet-DNP is expected to be applied in the field of biotechnology. On the other hand, due to the insolubility of the pentacene derivative, which is the common polarizing agent, in water, most research has been conducted using organic solids in which the polarizing agent is dispersed. There has been limited examples of polarizing water molecules.[97] Despite the importance of the expected applications, this field remains largely unexplored.

1-4 Singlet Fission

・1-4-1 introduction of singlet fission

While photo-excited triplet states is usually populated by ISC from S_1 in the ns time scale, it is possible to produce an excited triplet state in much shorter time scale by a process called singlet fission[24-26]. This is a phenomenon in which a dye in the S_1 state forms a TT dimer consisting of two triplet states with the surrounding dye in the ground state, resulting in two molecules in the T_1 state, corresponding to the reverse process of TTA.

・1-4-2 brief history

The existence of singlet fission itself was proposed in 1965,[98] and was also used in 1969 [99, 100] as a reason for the low fluorescence quantum yield in tetracene crystals. The application of singlet fission to photovoltaics, which will be discussed later, was proposed in 1979[101] and 2006[102], and it has attracted a great deal of attention since then, mainly for its application in the energy field through the 2010s.

・1-4-3 Mechanism of singlet fission

The process of singlet fission can be roughly divided into the following two steps. The general condition for the formation of TT dimers is that the energy gap between S_1 and S_0 must be at least twice as large as the energy gap between T_1 and S_0. Molecules with an acene backbone, such as pentacene [103-108] and tetracene [109, 110], are typical examples of molecules that satisfy this energetic condition. The resulting TT dimer is in a triplet state as an individual molecule, but as a dimer of two molecules coupled together, it has a singlet character and can be regarded as a transition process from singlet S_1 to singlet TT dimer. Therefore, it can be treated as a kind of spin permissive transition, which is known to occur earlier than spin forbidden processes involving spin reversal, such as intersystem crossing. The competition with the recombination can also affect the quantum yield of T_1 after singlet splitting [111]. The TT dimer then splits from the singlet through the quintet into two T_1 (Figure 1-16). [112-119]

$$S_1 + S_0 \leftrightarrows {}^1(T_1T_1) \leftrightarrows {}^5(T_1T_1) \leftrightarrows T_1 + T_1$$

$(equation\ 15)$

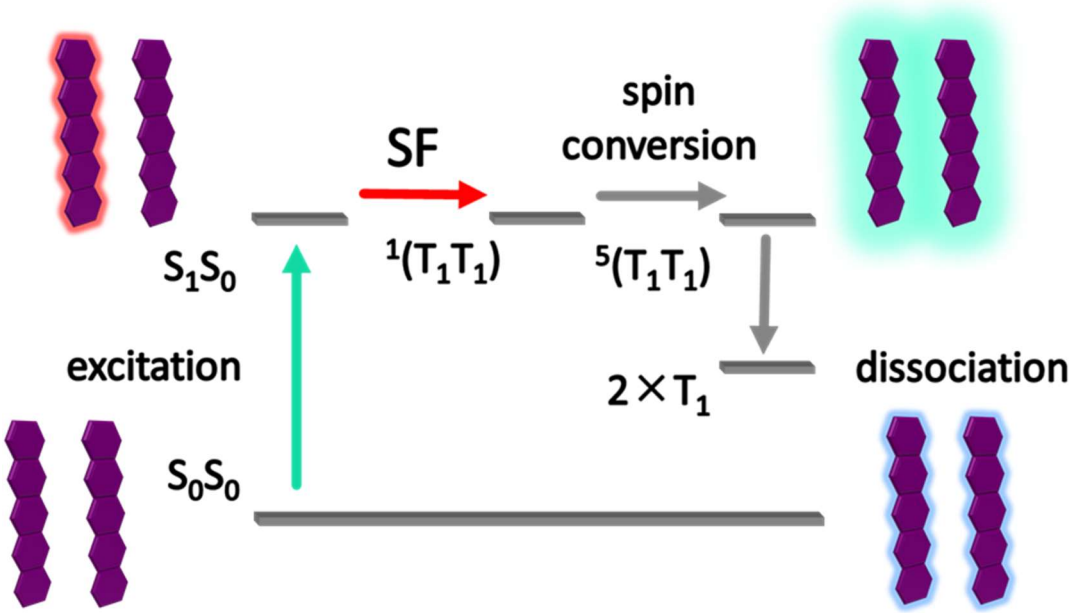

Figure 1-16. Schematic illustration of singlet fission

After the excited singlet state of a single molecule is passed through the TT dimer in the singlet and quintet states, the excited triplet state of two molecules is generated.

Since singlet fission is a picosecond process, pump-probe transient absorption measurements with high time resolution have been used for the characterization.[120-123] The absorption spectra derived from various excited states are detected by subtracting the absorption spectra with and without excitation light, and it is possible to confirm that singlet fission is occurring from the decay of the peak derived from S_1 and the generation of the peak derived from T_1. The TT dimer in the singlet state has no magnetism, but the TT dimer in the quintet state and the final T_1 state have magnetism because the sum of the spin quantum numbers is not zero, and the occurrence of singlet fission can also be observed using electron resonance (ESR) spectroscopy (Figure 1-17).[112-119]

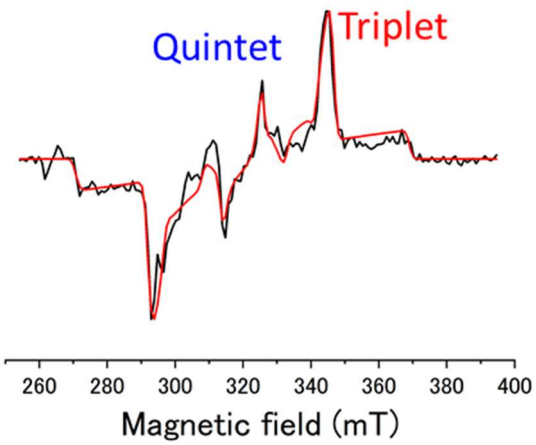

Figure 1-17. Example of a time-resolved ESR spectrum of a material showing singlet fission.
The characteristic feature is that in addition to the peak from triplet, the peak from quintet is observed.

・1-4-4 Application of singlet fission

Since singlet fission is a very fast process, T_1 can be obtained from S_1 before deactivation.[124] In addition, if we take into account the fact that two T_1 can be obtained from a single photon, the quantum yield can be as high as 200%.[125, 126] Since the quantum yield of T_1 in singlet fission far exceeds the conventional theoretical limit, it can be regarded as a method for efficiently utilizing the energy from T_1, and is actually attracting attention in the fields of photovoltaics[102, 127-131] and OLED[132]. In photovoltaic power generation, energy in excess of the band gap of the semiconductor is lost as heat, resulting in a loss during energy conversion. For this reason, the energy conversion efficiency limit of conventional photovoltaics is 33%, which is known as the Shockley-Queisser limit.[133] In singlet fission, light with energy more than twice the band gap can be used efficiently, and the Shockley-Queisser limit becomes 44%,[134] which is a significant improvement over the conventional theoretical limit. In addition, in the OLED field, singlet fission from the electrically excited S_1 state can be used to efficiently generate T_1 and increase the quantum efficiency.

Thus, by designing a system that focuses on singlet fission, which is one of the triplet generation processes, the quantum yield of the excited triplet state can be expected to be greatly improved. Therefore, it is a notable advantage that various functions based on the triplet state itself can be made more efficient by using the singlet fission.

1-5 Overview

In this thesis, we focus on various optical functions related to the excited triplet state and try to solve various problems by incorporating these functions into supramolecular materials.

Chapter 2 describes the TTA-UC from visible light to UV light based on supramolecular assembly under practical conditions of air-saturated water. We designed an amphiphilic acceptor with fluorescence in the UV region and co-assembled it with a fatty acid in water to make a dense structure that suppresses the diffusion of oxygen. To this aggregate, a donor with absorption in the visible region were added to form a ternary supramolecular aggregate. By irradiating the aggregate with a visible laser at 445 nm, upconversion emission was observed around 390 nm in the UV region. This emission was stable for more than one hour even in a sample prepared under atmospheric conditions.

Chapter 3 describes the first example of nuclear spin polarization of water molecules by using the electron spin polarization generated by SF. The aggregation state of the polarizing agent molecules was controlled in various ways in aqueous solvents using supramolecular chemistry approach, and their SF properties were evaluated using pump-probe transient absorption and time-resolved ESR measurements. We have succeeded in enhancing the NMR signal of water molecules more than several tens of times by using the electron polarization of SF-generated triplet as well as quintet state. In the DNP using the quintet state, the high Rabi frequency of the quintet was utilized to drive the DNP at a weaker microwave power than that of ordinary triplet-based DNP.

1-6 Conclusion

In this chapter, we have described the unique properties of photoexcited triplet states and various functions that utilize them. The application of these functions can bring about significant progress in various fields, such as the highly efficient use of optical energy and bioimaging. On the other hand, these functions require multiple components to appear in the system and their assembly structures to be controlled. In this paper, we focus on the supramolecular chemistry approach to assemble multiple molecules and describe the development of supramolecular functional materials exhibiting various functions of the excited triplet state.

1-7 References

1. S. Baluschev, T. Miteva, V. Yakutkin, G. Nelles, A. Yasuda and G. Wegner, *Phys. Rev. Lett.*, 2006, **97**, 143903.
2. T. N. Singh-Rachford and F. N. Castellano, *Coord. Chem. Rev.*, 2010, **254**, 2560-2573.
3. J. H. Kim and J. H. Kim, *J. Am. Chem. Soc.*, 2012, **134**, 17478-17481.
4. A. Monguzzi, R. Tubino, S. Hoseinkhani, M. Campione and F. Meinardi, *Phys. Chem. Chem. Phys.*, 2012, **14**, 4322-4332.
5. Y. C. Simon and C. Weder, *J. Mater. Chem.*, 2012, **22**.
6. K. Börjesson, D. Dzebo, B. Albinsson and K. Moth-Poulsen, *J. Mater. Chem. A*, 2013, **1**.
7. S. H. Askes, A. Bahreman and S. Bonnet, *Angew. Chem., Int. Ed. Engl.*, 2014, **53**, 1029-1033.
8. T. F. Schulze and T. W. Schmidt, *Energy Environ. Sci.*, 2015, **8**, 103-125.
9. J. Zhou, Q. Liu, W. Feng, Y. Sun and F. Li, *Chem. Rev.*, 2015, **115**, 395-465.
10. C. Fan, W. Wu, J. J. Chruma, J. Zhao and C. Yang, *J. Am. Chem. Soc.*, 2016, **138**, 15405-15412.
11. N. Yanai and N. Kimizuka, *Chem. Commun.*, 2016, **52**, 5354-5370.
12. J. Han, Y. Jiang, A. Obolda, P. Duan, F. Li and M. Liu, *J. Phys. Chem. Lett.*, 2017, **8**, 5865-5870.
13. S. P. Hill and K. Hanson, *J. Am. Chem. Soc.*, 2017, **139**, 10988-10991.
14. Z. Huang and M. L. Tang, *J. Am. Chem. Soc.*, 2017, **139**, 9412-9418.
15. W. Xu, W. Liang, W. Wu, C. Fan, M. Rao, D. Su, Z. Zhong and C. Yang, *Chemistry*, 2018, **24**, 16677-16685.
16. A. Henstra, T.-S. Lin ', J. Schmidt and W. T. Wenckebach, *Chem. Phys. Lett.*, 1990, **165**, 6-10.
17. M. Iinuma, Y. Takahashi, I. Shake, M. Oda, A. Masaike, T. Yabuzaki and H. M. Shimizu, *J. Magn. Reson.*, 2005, **175**, 235-241.
18. K. Takeda, *Triplet State Dynamic Nuclear Polarization*, VDM Verlag Dr. Mu̇eller: Saarbru̇cken, Germany, 2009.
19. K. Tateishi, M. Negoro, A. Kagawa and M. Kitagawa, *Angew. Chem., Int. Ed. Engl.*, 2013, **52**, 13307-13310.
20. K. Tateishi, M. Negoro, S. Nishida, A. Kagawa, Y. Morita and M. Kitagawa, *Proc. Natl. Acad. Sci. USA*, 2014, **111**, 7527-7530.
21. M. Negoro, A. Kagawa, K. Tateishi, Y. Tanaka, T. Yuasa, K. Takahashi and M. Kitagawa, *J. Phys. Chem. A*, 2018, **122**, 4294-4297.
22. K. Tateishi, M. Negoro, H. Nonaka, A. Kagawa, S. Sando, S. Wada, M. Kitagawa and T. Uesaka, *Phys. Chem. Chem. Phys.*, 2019, **21**, 19737-19741.
23. K. Nishimura, H. Kouno, Y. Kawashima, K. Orihashi, S. Fujiwara, K. Tateishi, T. Uesaka, N. Kimizuka and N. Yanai, *Chem. Commun.*, 2020, **56**, 7217-7232.

24. M. B. Smith and J. Michl, *Chem. Rev.*, 2010, **110**, 6891–6936.
25. B. J. Walker, A. J. Musser, D. Beljonne and R. H. Friend, *Nat. Chem.*, 2013, **5**, 1019-1024.
26. K. Miyata, F. S. Conrad-Burton, F. L. Geyer and X. Y. Zhu, *Chem. Rev.*, 2019, **119**, 4261-4292.
27. S. P. McGlynn;, T. Azumi; and M.Kinoshita, *Molecular spectroscopy of the triplet state*, Prentice-Hall, U.S.: Englewood cliffs, New Jersey,, 1969.
28. N. J. Turro, V. Ramamurthy and J. C. Scaiano, *Modern Molecular Photochemistry of Organic Molecules*, University Science Books, 2010.
29. S. L. Bayliss, F. Kraffert, R. Wang, C. Zhang, R. Bittl and J. Behrends, *J. Phys. Chem. Lett.*, 2019, **10**, 1908-1913.
30. M. A. Filatov, S. Baluschev and K. Landfester, *Chem. Soc. Rev.*, 2016, **45**, 4668-4689.
31. S. H. C. Askes and S. Bonnet, *Nat. Rev. Chem.*, 2018, **2**, 437-452.
32. N. Dam, T. Keszthelyi, L. K. Andersen, K. V. Mikkelsen and P. R. Ogilby, *J. Phys. Chem. A* 2002, **106**, 5263-5270.
33. C. Schweitzer and R. Schmidt, *Chem. Rev.*, 2003, **103**, 1685−1757.
34. F. Helmchen and W. Denk, *Nat. Methods*, 2005, **2**, 932-940.
35. M. Pawlicki, H. A. Collins, R. G. Denning and H. L. Anderson, *Angew. Chem., Int. Ed. Engl.*, 2009, **48**, 3244-3266.
36. F. Auzel, *Chem. Rev.*, 2004, **104**, 139−173.
37. F. Wang and X. Liu, *Chem. Soc. Rev.*, 2009, **38**, 976-989.
38. F. Wang, D. Banerjee, Y. Liu, X. Chen and X. Liu, *Analyst*, 2010, **135**, 1839-1854.
39. L. Huang, Y. Zhao, H. Zhang, K. Huang, J. Yang and G. Han, *Angew. Chem., Int. Ed. Engl.*, 2017, **56**, 14400-14404.
40. C. A. Parker, C. G. Hatchard and T. A. Joyce, *Nature*, 1965, **205**, 1282-1284.
41. J. Zhao, S. Ji and H. Guo, *RSC Adv.*, 2011, **1**.
42. V. Yakutkin, S. Aleshchenkov, S. Chernov, T. Miteva, G. Nelles, A. Cheprakov and S. Baluschev, *Chemistry*, 2008, **14**, 9846-9850.
43. T. N. Singh-Rachford, A. Nayak, M. L. Muro-Small, S. Goeb, M. J. Therien and F. N. Castellano, *J. Am. Chem. Soc.*, 2010, **132**, 14204-14211.
44. P. Duan, N. Yanai and N. Kimizuka, *Chem. Commun.*, 2014, **50**, 13111-13113.
45. T. C. Wu, D. N. Congreve and M. A. Baldo, *Appl. Phys. Lett.*, 2015, **107**.
46. N. Yanai, M. Kozue, S. Amemori, R. Kabe, C. Adachi and N. Kimizuka, *J. Mater. Chem. C*, 2016, **4**, 6447-6451.
47. Q. Chen, Y. Liu, X. Guo, J. Peng, S. Garakyaraghi, C. M. Papa, F. N. Castellano, D. Zhao and Y. Ma, *J. Phys. Chem. A*, 2018, **122**, 6673-6682.
48. Z. Huang, X. Li, M. Mahboub, K. M. Hanson, V. M. Nichols, H. Le, M. L. Tang and C. J.

Bardeen, *Nano Lett.*, 2015, **15**, 5552-5557.

49. M. Wu, D. N. Congreve, M. W. B. Wilson, J. Jean, N. Geva, M. Welborn, T. Van Voorhis, V. Bulović, M. G. Bawendi and M. A. Baldo, *Nat. Photonics*, 2015, **10**, 31-34.
50. C. Mongin, S. Garakyaraghi, N. Razgoniaeva, M. Zamkov and F. N. Castellano, *Science*, 2016, **351**, 369-372.
51. K. Okumura, K. Mase, N. Yanai and N. Kimizuka, *Chemistry*, 2016, **22**, 7721-7726.
52. K. Mase, K. Okumura, N. Yanai and N. Kimizuka, *Chem. Commun.*, 2017, **53**, 8261-8264.
53. L. Nienhaus, J.-P. Correa-Baena, S. Wieghold, M. Einzinger, T.-A. Lin, K. E. Shulenberger, N. D. Klein, M. Wu, V. Bulović, T. Buonassisi, M. A. Baldo and M. G. Bawendi, *ACS Energy Lett.*, 2019, **4**, 888-895.
54. S. Amemori, Y. Sasaki, N. Yanai and N. Kimizuka, *J. Am. Chem. Soc.*, 2016, **138**, 8702-8705.
55. Y. Sasaki, S. Amemori, H. Kouno, N. Yanai and N. Kimizuka, *J. Mater. Chem. C*, 2017, **5**, 5063-5067.
56. Y. Y. Cheng, B. Fückel, T. Khoury, R. G. C. R. Clady, M. J. Y. Tayebjee, N. J. Ekins-Daukes, M. J. Crossley and T. W. Schmidt, *J. Phys. Chem. Lett.*, 2010, **1**, 1795-1799.
57. R. S. Khnayzer, J. Blumhoff, J. A. Harrington, A. Haefele, F. Deng and F. N. Castellano, *Chem. Commun.*, 2012, **48**, 209-211.
58. A. Monguzzi, A. Oertel, D. Braga, A. Riedinger, D. K. Kim, P. N. Knusel, A. Bianchi, M. Mauri, R. Simonutti, D. J. Norris and F. Meinardi, *ACS Appl. Mater. Interfaces*, 2017, **9**, 40180-40186.
59. B. D. Ravetz, A. B. Pun, E. M. Churchill, D. N. Congreve, T. Rovis and L. M. Campos, *Nature*, 2019, **565**, 343-346.
60. S. L. Hopkins, B. Siewert, S. H. Askes, P. Veldhuizen, R. Zwier, M. Heger and S. Bonnet, *Photochem. Photobiol. Sci.*, 2016, **15**, 644-653.
61. A. Monguzzi, J. Mezyk, F. Scotognella, R. Tubino and F. Meinardi, *Phys. Rev. B*, 2008, **78**.
62. A. Haefele, J. Blumhoff, R. S. Khnayzer and F. N. Castellano, *J. Phys. Chem. Lett.*, 2012, **3**, 299-303.
63. J. Jortner, S.-i. Choi, J. L. Katz and S. A. Rice, *Phys. Rev. Lett.*, 1963, **11**, 323-326.
64. Q. Liu, B. Yin, T. Yang, Y. Yang, Z. Shen, P. Yao and F. Li, *J. Am. Chem. Soc.*, 2013, **135**, 5029-5037.
65. F. Marsico, A. Turshatov, R. Pekoz, Y. Avlasevich, M. Wagner, K. Weber, D. Donadio, K. Landfester, S. Baluschev and F. R. Wurm, *J. Am. Chem. Soc.*, 2014, **136**, 11057-11064.
66. S. H. Askes, N. Lopez Mora, R. Harkes, R. I. Koning, B. Koster, T. Schmidt, A. Kros and S. Bonnet, *Chem. Commun.*, 2015, **51**, 9137-9140.
67. D. Dzebo, K. Moth-Poulsen and B. Albinsson, *Photochem. Photobiol. Sci.*, 2017, **16**, 1327-1334.

68. J. Ma, S. Chen, C. Ye, M. Li, T. Liu, X. Wang and Y. Song, *Phys. Chem. Chem. Phys.*, 2019, **21**, 14516-14520.
69. J.-H. Kim, F. Deng, F. N. Castellano and J.-H. Kim, *ACS Photonics*, 2014, **1**, 382-388.
70. S. Mattiello, A. Monguzzi, J. Pedrini, M. Sassi, C. Villa, Y. Torrente, R. Marotta, F. Meinardi and L. Beverina, *Adv. Funct. Mater.*, 2016, **26**, 8447-8454.
71. E. M. Purcell, H. C. Torrey and R. V. Pound, *Phys. Rev.*, 1946, **69**, 37-38.
72. F. Bloch, W. W. Hansen and M. Packard, *Phys. Rev.*, 1946, **69**, 127-127.
73. J. T. Arnold, S. S. Dharmatti and M. E. Packard, *J. Chem. Phys.*, 1951, **19**, 507-507.
74. P. C. Lauterbur, *Nature*, 1973, **242**, 190-191.
75. A. W. Overhauser, *Phys. Rev.*, 1953, **92**, 411-415.
76. A. Pines, M. G. Gibby and J. S. Waugh, *J. Chem. Phys.*, 1973, **59**, 569-590.
77. S. R. Hartmann and E. L. Hahn, *Phys. Rev.*, 1962, **128**, 2042-2053.
78. Anil Kumar, Dieter Welti and R. R. Ernst, *J. Magn. Reson.*, 1975, **18**, 69-83.
79. W. P. Aue, E. Bartholdi and R. R. Ernst, *J. Chem. Phys.*, 1976, **64**, 2229-2246.
80. K. Wuthrich, *NMR of proteins and nucleic acids*, Wiley, 1986.
81. Z. Serber, A. T. Keatinge-Clay, R. Ledwidge, A. E. Kelly, S. M. Miller and V. Dötsch, *J. Am. Chem. Soc.*, 2001, **123**, 2446-2447.
82. P. E. Wrigh and H. J. Dyson, *J. Mol. Biol.* , 1999, **293**, 321-331.
83. T. R. Carver and C. P. Slichter, *Phys. Rev.*, 1953, **92**, 212-213.
84. J. H. Ardenkjær-Larsen, B. Fridlund, A. Gram, G. Hansson, L. Hansson, M. H. Lerche, R. Servin, M. Thaning and K. Golman, *Proc. Natl. Acad. Sci. USA*, 2003, **100**, 10158–10163.
85. K. Golman, R. I. Zandt, M. Lerche, R. Pehrson and J. H. Ardenkjaer-Larsen, *Cancer Res.*, 2006, **66**, 10855-10860.
86. F. A. Gallagher, M. I. Kettunen, S. E. Day, D. E. Hu, J. H. Ardenkjaer-Larsen, R. Zandt, P. R. Jensen, M. Karlsson, K. Golman, M. H. Lerche and K. M. Brindle, *Nature*, 2008, **453**, 940-943.
87. C. Song, K.-N. Hu, C.-G. Joo, T. M. Swager and R. G. Griffin, *J. Am. Chem. Soc.*, 2006, **128**, 11385-11390.
88. M. H. Levitt, *Spin Dynamics: Basics of Nuclear Magnetic Resonance*, Wiley, The University of Southampton, UK, 2nd edn., 2008.
89. S. Lange, A. H. Linden, U. Akbey, W. T. Franks, N. M. Loening, B. J. van Rossum and H. Oschkinat, *J. Magn. Reson.*, 2012, **216**, 209-212.
90. M. Deimling, H. Brunner, K. P. Dinse and K. H. Hawser, *J. Magn. Reson.*, 1980, **39**, 185-202.
91. M. Iinuma, Y. Takahashi, I. Shaké, M. Oda, A. Masaike and T. Yabuzaki, *Phys. Rev. Lett.*, 2000, **84**, 171-174.

92. A. Henstra and W. T. Wenckebach, *Mol. Phys.*, 2013, **112**, 1761-1772.
93. T. V. Can, R. T. Weber, J. J. Walish, T. M. Swager and R. G. Griffin, *Angew. Chem., Int. Ed. Engl.*, 2017, **56**, 6744-6748.
94. T. Yago, G. Link, G. Kothe and T. S. Lin, *J. Chem. Phys.*, 2007, **127**, 114503.
95. S. Fujiwara, M. Hosoyamada, K. Tateishi, T. Uesaka, K. Ideta, N. Kimizuka and N. Yanai, *J. Am. Chem. Soc.*, 2018, **140**, 15606-15610.
96. P. Dutta, G. V. Martinez and R. J. Gillies, *Biophys. Rev.*, 2013, **5**, 271-281.
97. H. Kouno, K. Orihashi, K. Nishimura, Y. Kawashima, K. Tateishi, T. Uesaka, N. Kimizuka and N. Yanai, *Chem. Commun.*, 2020, **56**, 3717-3720.
98. S. Singh, W. J. Jones, W. Siebrand, B. P. Stoicheff and W. G. Schneider, *J. Chem. Phys.*, 1965, **42**, 330-342.
99. N. Geacintov, M. Pope and F. Vogel, *Phys. Rev. Lett.*, 1969, **22**, 593-596.
100. R. E. Merrifield, P. Avakian and R. P. Groff, *Chem. Phys. Lett.*, 1969, **3**, 386-388.
101. D. L. Dexter, *J. Lumin.*, 1979, **18**, 779-784.
102. M. C. Hanna and A. J. Nozik, *J. Appl. Phys.*, 2006, **100**, 074510.
103. S. N. Sanders, E. Kumarasamy, A. B. Pun, M. T. Trinh, B. Choi, J. Xia, E. J. Taffet, J. Z. Low, J. R. Miller, X. Roy, X. Y. Zhu, M. L. Steigerwald, M. Y. Sfeir and L. M. Campos, *J. Am. Chem. Soc.*, 2015, **137**, 8965-8972.
104. S. N. Sanders, E. Kumarasamy, A. B. Pun, M. L. Steigerwald, M. Y. Sfeir and L. M. Campos, *Chem*, 2016, **1**, 505-511.
105. S. Khan and S. Mazumdar, *J. Phys. Chem. Lett.*, 2017, **8**, 4468-4478.
106. S. Refaely-Abramson, F. H. da Jornada, S. G. Louie and J. B. Neaton, *Phys. Rev. Lett.*, 2017, **119**, 267401.
107. M. T. Trinh, A. Pinkard, A. B. Pun, S. N. Sanders, E. Kumarasamy, M. Y. Sfeir, L. M. Campos, X. Roy and X.-Y. Zhu, *Sci. Adv.* , 2017, **3**, e1700241.
108. B. D. Folie, J. B. Haber, S. Refaely-Abramson, J. B. Neaton and N. S. Ginsberg, *J. Am. Chem. Soc.*, 2018, **140**, 2326-2335.
109. C.E.Swenberg and W.T.Stacy, *Chem. Phys. Lett.*, 1968, **2**, 327-328.
110. A. A. Kazzaz and A. B. Zahlan, *J. Chem. Phys.*, 1968, **48**, 1242-1245.
111. V. I. Klimov, J. A. McGuire, R. D. Schaller and V. I. Rupasov, *Phys. Rev. B*, 2008, **77**.
112. M. J. Y. Tayebjee, S. N. Sanders, E. Kumarasamy, L. M. Campos, M. Y. Sfeir and D. R. McCamey, *Nat. Phys.*, 2016, **13**, 182-188.
113. L. R. Weiss, S. L. Bayliss, F. Kraffert, K. J. Thorley, J. E. Anthony, R. Bittl, R. H. Friend, A. Rao, N. C. Greenham and J. Behrends, *Nat. Phys.*, 2016, **13**, 176-181.
114. B. S. Basel, J. Zirzlmeier, C. Hetzer, B. T. Phelan, M. D. Krzyaniak, S. R. Reddy, P. B. Coto, N. E. Horwitz, R. M. Young, F. J. White, F. Hampel, T. Clark, M. Thoss, R. R. Tykwinski,

M. R. Wasielewski and D. M. Guldi, *Nat. Commun.*, 2017, **8**, 15171.

115. D. Lubert-Perquel, E. Salvadori, M. Dyson, P. N. Stavrinou, R. Montis, H. Nagashima, Y. Kobori, S. Heutz and C. W. M. Kay, *Nat. Commun.*, 2018, **9**, 4222.
116. H. Nagashima, S. Kawaoka, S. Akimoto, T. Tachikawa, Y. Matsui, H. Ikeda and Y. Kobori, *J. Phys. Chem. Lett.*, 2018, **9**, 5855-5861.
117. H. Sakai, R. Inaya, H. Nagashima, S. Nakamura, Y. Kobori, N. V. Tkachenko and T. Hasobe, *J. Phys. Chem. Lett.*, 2018, **9**, 3354-3360.
118. Y. Matsui, S. Kawaoka, H. Nagashima, T. Nakagawa, N. Okamura, T. Ogaki, E. Ohta, S. Akimoto, A. Sato-Tomita, S. Yagi, Y. Kobori and H. Ikeda, *J. Phys. Chem. C*, 2019, **123**, 18813-18823.
119. A. B. Pun, A. Asadpoordarvish, E. Kumarasamy, M. J. Y. Tayebjee, D. Niesner, D. R. McCamey, S. N. Sanders, L. M. Campos and M. Y. Sfeir, *Nat. Chem.*, 2019, **11**, 821-828.
120. C. Jundt, G. Klein, B. Sipp, J. Le Moigne, M. Joucla and A. A. Villaeys, *Chem. Phys. Lett.*, 1995, **241**, 84-88.
121. M. W. Wilson, A. Rao, J. Clark, R. S. Kumar, D. Brida, G. Cerullo and R. H. Friend, *J. Am. Chem. Soc.*, 2011, **133**, 11830-11833.
122. L. Ma, K. Zhang, C. Kloc, H. Sun, M. E. Michel-Beyerle and G. G. Gurzadyan, *Phys. Chem. Chem. Phys.*, 2012, **14**, 8307-8312.
123. M. W. Wilson, A. Rao, K. Johnson, S. Gelinas, R. di Pietro, J. Clark and R. H. Friend, *J. Am. Chem. Soc.*, 2013, **135**, 16680-16688.
124. E. J. Bowen, E. Mikiewicz and F. W. Smith, *Proc. Phys. Soc. A*, 1949, **62**, 26-31.
125. Jean-Luc Brédas, David Beljonne, Veaceslav Coropceanu and J. Cornil, *Chem. Rev.*, 2004, **104**, 4971−5003.
126. J. J. Burdett, A. M. Muller, D. Gosztola and C. J. Bardeen, *J. Chem. Phys.*, 2010, **133**, 144506.
127. D. N. Congreve, J. Lee, N. J. Thompson, E. Hontz, S. R. Yost, P. D. Reusswig, M. E. Bahlke, S. Reineke, T. V. Voorhis and M. A. Baldo, *Science*, 2013, **340**, 334-337.
128. M. Tabachnyk, B. Ehrler, S. Gelinas, M. L. Bohm, B. J. Walker, K. P. Musselman, N. C. Greenham, R. H. Friend and A. Rao, *Nat. Mater.*, 2014, **13**, 1033-1038.
129. N. J. Thompson, M. W. Wilson, D. N. Congreve, P. R. Brown, J. M. Scherer, T. S. Bischof, M. Wu, N. Geva, M. Welborn, T. V. Voorhis, V. Bulovic, M. G. Bawendi and M. A. Baldo, *Nat. Mater.*, 2014, **13**, 1039-1043.
130. M. Einzinger, T. Wu, J. F. Kompalla, H. L. Smith, C. F. Perkinson, L. Nienhaus, S. Wieghold, D. N. Congreve, A. Kahn, M. G. Bawendi and M. A. Baldo, *Nature*, 2019, **571**, 90-94.
131. Y. Jiang, M. P. Nielsen, A. J. Baldacchino, M. A. Green, D. R. McCamey, M. J. Y. Tayebjee, T. W. Schmidt and N. J. Ekins-Daukes, *Prog. Photovolt.: Res. Appl*, 2021, **29**, 899-906.

132. R. Nagata, H. Nakanotani, W. J. Potscavage, Jr. and C. Adachi, *Adv. Mater.*, 2018, DOI: 10.1002/adma.201801484, e1801484.
133. W. Shockley and H. J. Queisser, *J. Appl. Phys.*, 1961, **32**, 510-519.
134. C. A. Nelson, N. R. Monahan and X.-Y. Zhu, *Energy Environ. Sci.*, 2013, **6**, 3508–3519.

Chapter2

Visible-to-UV photon upconversion in air-saturated water by multicomponent co-assembly

Abstract :

Air-stable, visible-to-UV photon upconversion based on triplet-triplet annihilation (TTA-UC) in water has been an outstanding issue despite its importance in a wide range of applications. This is achieved by giving oxygen barrier property to cationic acceptor self-assemblies through an ion complex formation with anionic fatty acids, i.e, supramolecular crowding.

2-1 Introduction

The efficient utilization of solar energy is the key to solve current energy problems. Water-splitting photocatalysts can convert solar energy into molecular hydrogen, which is anticipated as a clean energy source. Highly efficient water-splitting reactions occur under the illumination of ultraviolet (UV) light, however, the portion of UV light is limited to only ca. 5% in whole solar irradiance.[1] Therefore, the visible (vis)-to-UV photon energy conversion is expected to expand the available wavelength range for the water-splitting photocatalysis. Photon upconversion (UC) is a method to convert lower-energy photons to higher-energy photons by combining the energy of multiple photons. For solar energy applications, photon upconversion based on triplet-triplet annihilation (TTA-UC) is particularly promising since it can operate under low-intensity light comparable to sunlight.[2-23] As summarized in Fig. 2-1, TTA-UC is composed of two kinds of chromophores, a donor (triplet sensitizer) and an acceptor (emitter). Donor triplets are generated via intersystem crossing (ISC) from photo-excited singlets. Triplet energy transfer (TET) from the donor to the acceptor populates acceptor triplets. Two acceptor triplets generate a higher-energy singlet state of the acceptor through TTA, which results in the upconverted delayed fluorescence. As noted, the vis-to-UV TTA-UC is expected to boost the efficiency of photocatalytic reactions.[24-39] However, TTA-UC has a fatal problem that the photo-excited triplets are easily quenched by molecular oxygen dissolved in water. The common strategy to avoid the oxygen quenching is to employ viscous droplets or polymers,[5, 40, 41] which inevitably makes the diffusion of large TTA chromophores slow.

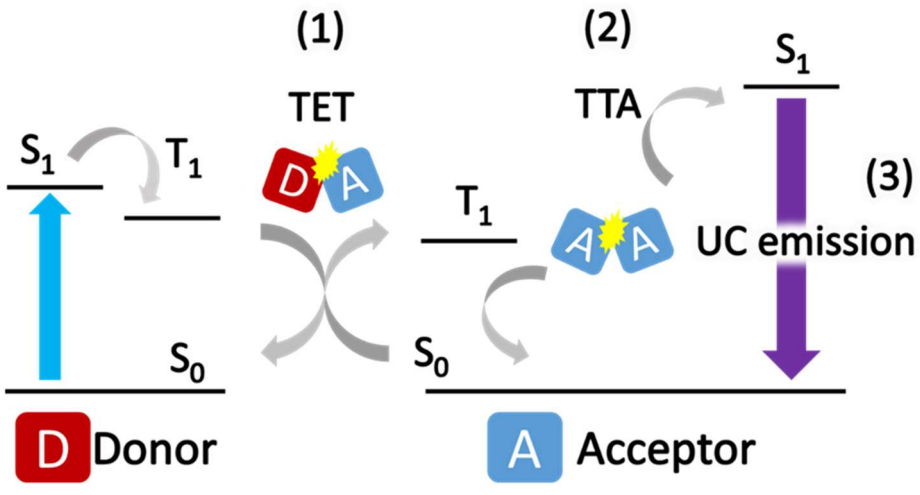

Figure 2-1. An outline of the TTA-UC process.

As an alternative strategy, we have reported that the self-assembly of amphiphilic chromophores enables TTA-UC even in air-saturated water.[15, 42-44] In this mechanism, TTA-UC occurs via triplet energy migration in densely self-assembled chromophore arrays and is not dependent on the conventional molecular diffusion. The high oxygen blocking ability was achieved by co-assembly of cationic amphiphilic acceptors with anionic fatty acids, which increased the molecular density around the chromophores, so-called supramolecular crowding.[44] Meanwhile, the demonstration of this strategy has been limited to the model vis-to-vis (green-to-blue) TTA-UC.

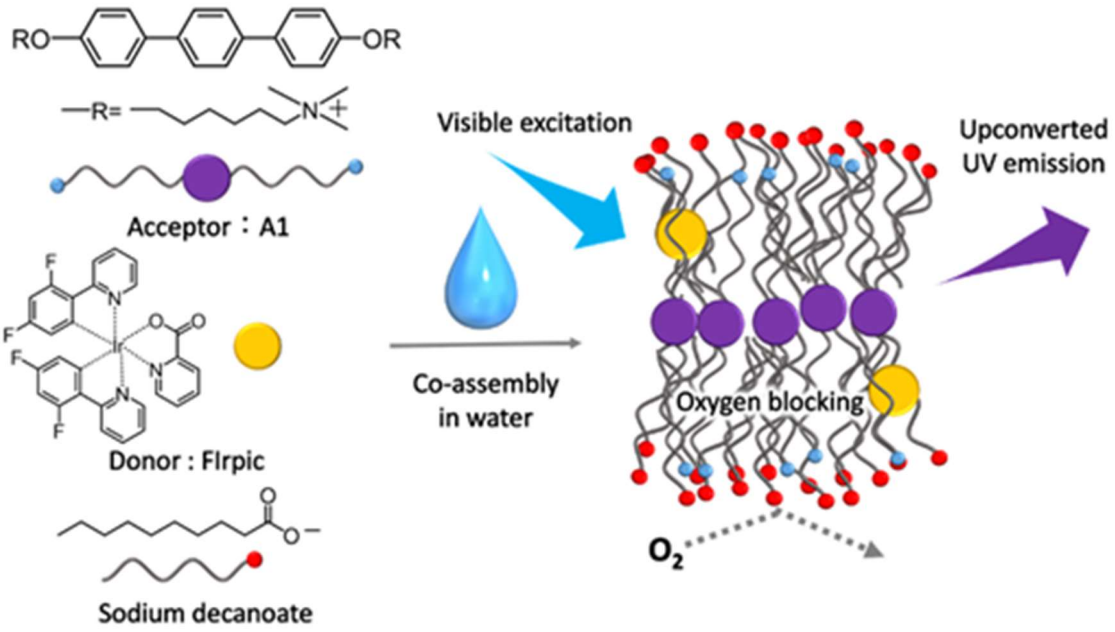

Figure 2-2. Schematic illustration of supramolecular system for air-stable aqueous vis-to-UV TTA-UC. Cationic acceptor **A1**, donor FIrpic, and anionic sodium decanoate (Dec) form aqueous co-assemblies with oxygen blocking ability.

Here, we report the first example of air-stable vis-to-UV TTA-UC in water by generalizing the supramolecular design concept. We designed a novel UV-emitting bola-type amphiphile **A1** in which a *p*-terphenyl chromophore was introduced as an acceptor to pursuit vis-to-UV TTA-UC (Figure 2-2).[31] Alkyl chains and quaternary ammonium groups are attached to the *p*-terphenyl skeleton as hydrophobic spacers and hydrophilic groups, respectively. Following our successful design for air-stable green-to-blue TTA-UC,[44] the cationic **A1** was co-assembled with anionic decanoate (Dec) whose alkyl chain length is close to the alkyl spacer of **A1**. By introducing a visible light absorbing triplet donor FIrpic,[45] the ternary co-assemblies showed a stable vis-to-UV TTA-UC even in air-saturated water.

2-2 Experimental section

・2-2-1 Materials.

All reagents and solvents for synthesis were used as received without further purification otherwise noted. 4-bromophenol, 1,4-phenylenediboronic acid, tetrakis (triphenylphosphine) palladium(0), and trimethylamine (ca. 25% in ethanol) were purchased from TCI, sodium hydride (60 % oil dispersion) and Na_2SO_4 was purchased form Wako, and potassium carbonate was purchased from KISHIDA.

All reagents and solvents for measurement were used as received without further purification. Bis[2-(4,6-difluorophenyl)pyridinato-C2,N](picolinato)iridium(III) (FIrpic) was purchased from Sigma-Aldrich. Sodium decanoate (Dec) was purchased from TCI Analytical grade methanol was purchased from Wako Pure Chemical and deionized water was generated by Direct-Q UV (Merck Millipore). For sample preparation of TTA-UC measurements, all the solids (**A1**, FIrpic and Dec) were first dissolved in methanol. After evaporating methanol, deionized water was added, and the aqueous dispersions were generated via ultrasonication and heating. The deaeration of the aqueous dispersion was conducted by repeated freeze-pump-thaw cycles.

・2-2-2 Characterizations.

^{1}H NMR (400 MHz) spectra were measured on a JEOL JNM-ECZ 400 using TMS as the internal standard. Elemental analysis was conducted by using Yanaco CHN Corder MT-5 at the Elemental Analysis Center, Kyushu University. UV-vis absorption spectra were recorded on JASCO V-670 and V-770 spectrophotometers. Luminescence spectra were measured by using an FP-8300 fluorescence spectrometer. The absolute fluorescence quantum yield was measured in an integrating sphere using a Hamamatsu Photonics absolute quantum yield measurement system. Dynamic light scattering (DLS) and zeta potential measurements were carried out by using a Malvern Nano-ZS ZEN3600. Scanning electron microscopy (SEM) images were measured by using a HITACHI FE-SEM SU9000. The supramolecular dispersion was cast on the carbon-coated cupper grid and dried in air.

・**2-2-3 TTA-UC measurements.**

For TTA-UC emission measurements, a diode laser (445 nm, 75 mW, RGB Photonics) was used as the excitation laser source. The laser power was controlled by combining a software (Ltune) and a variable neutral density filter and measured using a PD300-UV photodiode sensor (OPHIR Photonics). The laser beam was focused on the sample using a lens. The diameter of the laser beam ($1/e^2$) was measured at the sample position using a CCD beam profiler (SP620, OPHIR Photonics). The typical laser size was 3.93×10^{-4} cm^2. The emitted light was collimated by an achromatic lens, the excitation light was removed using short pass filters (425 nm and 400 nm), and the emitted light was again focused by an achromatic lens to an optical fiber connected to a multichannel detector (MCPD-9800, Otsuka Electronics). UC Photoluminescence decays of **A1** were measured using a UNISOKU TSP-2000 system. The TTA-UC efficiency (100% is set as a maximum) was measured by using an absolute quantum yield measurement system specially built by Hamamatsu Photonics. The sample was held in an integrating sphere and excited by the laser excitation source (445 nm, 75 mW, RGB Photonics). The scattered excitation light was removed using a 420 nm short-pass filter and emitted light was monitored with a multichannel detector. The spectrometer was calibrated including the integration sphere and short-pass filter by Hamamatsu Photonics.

・2-2-4 Synthesis of acceptor

Scheme 2-1. Synthesis of Acceptor (A1)

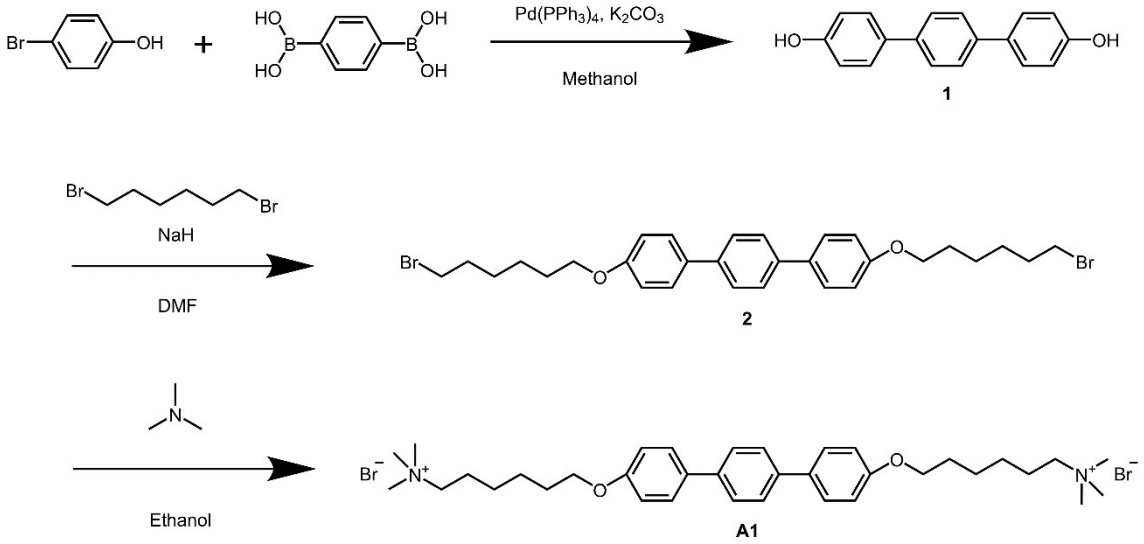

・2-2-4-1 Synthesis of 1

A dispersion of 4-bromophenol (519 mg, 3.0 mmol), 1,4-phenylenediboronic acid (166 mg, 1.0 mmol), potassium carbonate (829 mg, 6.0 mmol), and tetrakis (triphenylphosphine) palladium(0) (60 mg, 0.052 mmol) in 5.0 ml methanol was heated by microwave at 80 °C for 12 h. The resulting dispersion was washed several times with ethyl acetate and water, dried over anhydrous Na_2SO_4. The solvent was removed under reduced pressure, and the product was purified by silica gel column chromatography (Hexane/THF = 1/1). The product was purified by recrystallization in acetonitrile to give colorless crystals of **1**. (yield: 46 %).

^{1}H NMR (400 MHz, DMSO-d_6, TMS standard): δ (ppm) = 6.86-6.84, (d, 4H), 7.52-7.50, (d, 4H), 7.61, (s, 4H), 9.53, (s, 2H).

・2-2-4-2 Synthesis of 2

1 (50 mg, 0.19 mmol) was placed in a 100 ml flask under N_2, and 15 ml of dehydrated DMF was added. The solution was stirred at 0 °C under N_2, and then sodium hydride (28 mg, 1.15 mmol) was added. After 30 minutes, 1,6-dibromohexane (464 mg, 1.9 mmol) was added and stirred at 65 °C for a day. The resulting dispersion was washed several times with chloroform and water, and the organic layer was condensed by evaporation. Methanol was added into this dispersion and filtered. Resulting solid was recrystallized in toluene to obtain colorless crystal of **2** (yield: 63 %).

^{1}H NMR (400 MHz, $CDCl_3$, TMS standard): δ (ppm) = 1.93-1.81, (m, 8H), 3.45-3.42, (t, 3H), 4.03-4.00, (t, 3H), 6.99-6.96, (d, 4H), 7.57-7.54, (d, 4H), 7.60, (s, 4H).

・**2-2-4-3 Synthesis of A1**

2 (30 mg, 0.051 mmol) was dispersed in 5 ml of trimethylamine ethanol solution. The dispersion was heated by microwave at 80 °C for 24 h. The resulting dispersion was dried by evaporation and dispersed in hot methanol. The dispersion was filtered and the filtrate was evaporated to obtain **A1** (yield: 88 %).

^{1}H NMR (400 MHz, methanol-d_4, TMS standard): δ (ppm) = 1.42-1.35, (m ,4H), 1.57-1.49, (m, 4H), 1.80-1.71, (m, 8H), 3.03, (s, 18H), 3.97-3.94, (t, 4H), 6.91-6.89, (d, 4H), 7.49-7.47, (d, 4H), 7.52, (s, 4H).

Elemental analysis for $C_{72}H_{110}Br_4N_4O_5$: calculated (%) H 7.75 C 60.42 N 3.91 ; found (%) H 7.81 C 60.47 N 3.78.

2-3 Results and discussion

・2-3-1 Characterization of A1 in molecularly dispersed state

The new amphiphilic acceptor **A1** was synthesized and characterized by ^{1}H NMR and elemental analysis (Scheme 2-1). **A1** was molecularly dispersed in methanol, as confirmed by its concentration dependence of absorption spectra (Figure. 2-3).

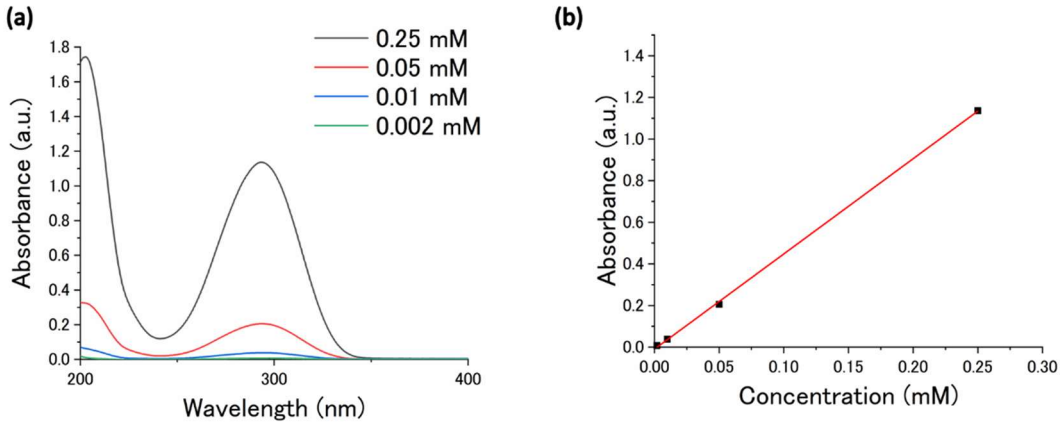

Figure 2-3. (a) Concentration-dependent UV-vis absorption spectra of **A1** in methanol ([**A1**] = 0.25-0.002 mM in methanol). (b) The absorbance of **A1** at 293.5 nm at different concentrations. The fitting result is shown as a red line according to the following equation, y = Ax+B. The observed linearity supports the molecularly-dispersed state of **A1** in methanol in the examined concentration range.

The molecularly-dispersed **A1** in methanol ([**A1**] = 0.25 mM) showed a fluorescence peak at 358 nm (Figure. 2-4) and a fluorescence quantum yield of 86%.

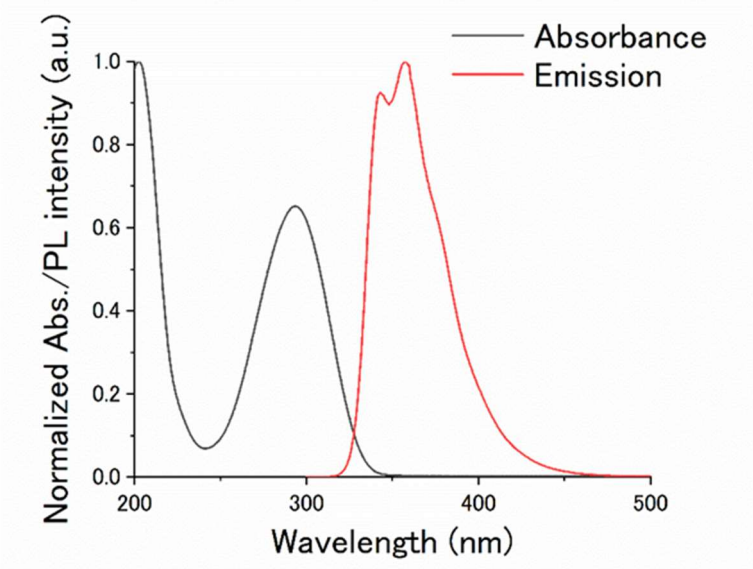

Figure 2-4. UV-vis absorption and fluorescence spectra of A1 in methanol ([A1] = 0.25 mM, λ_{ex} = 241 nm).

・2-3-2 Formation of supramolecular co-assembly of A1, FIrpic and Dec

To form the vis-to-UV upconverting ternary molecular system, **A1** was co-assembled with FIrpic and Dec. The three components **A1**, FIrpic and Dec were mixed by dissolving in methanol and the ternary mixture was obtained by removing the solvent under reduced pressure. After adding water, the ultrasonication and heating treatment of the mixture gave a pale-yellow translucent dispersion (Figure 2-5, [**A1**] = 10 mM, [FIrpic] = 100 μM and [Dec] = 80 mM). The appearance of this **A1**-FIrpic-Dec ternary dispersion is totally different from aqueous Dec and **A1** (Figure 2-5). Since the concentration of Dec is below its critical micellar concentration (cmc) of 86 mM, Dec provided a transparent solution.[46] **A1** was poorly soluble in water, and some precipitates were observed. This result suggests that A1 by itself is not suitable for UC measurement in water, and improvement of dispersibility is required. On the other hand, a stable dispersion was obtained when Dec (80 mM) was added in excess as compared to the concentration of **A1** (10 mM). Apparently, the co-assembly of **A1** with Dec through electrostatic and hydrophobic interactions improved the dispersibility of **A1** in water.

In the previous study, four hydrophilic functional groups were modified on the acceptor dye[44], while in this study, only two hydrophilic functional groups were modified at the para-position from the viewpoint of maintaining the luminescent properties of the dye, and the acceptor alone had low solubility. These results suggest that methods to control solubility, such as the addition of excess fatty acids for solubilize aggregation, are needed to generalize the technique of forming dense supramolecular aggregates for oxygen-blocking ability.

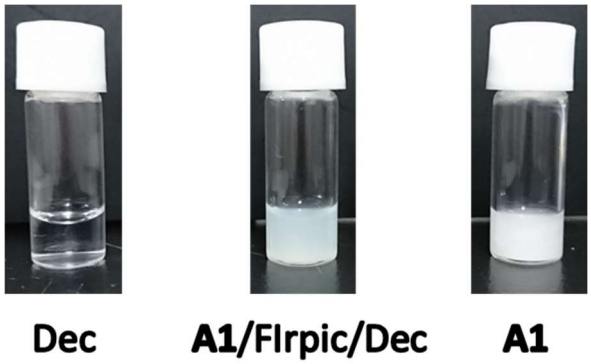

Figure 2-5. Photographs of Dec ([Dec] = 80 mM), **A1**-FIrpic-Dec ([**A1**] = 10 mM, [FIrpic] = 100 μM, [Dec] = 80 mM), and **A1** ([**A1**] = 10mM) in water.

• 2-3-3 Characterization of supramolecular co-assembly of A1, FIrpic and Dec

Dynamic light scattering (DLS), zeta potential, UV-vis absorption, fluorescence measurements, and SEM observation were performed to obtain further information about the ternary assembly. The DLS profile of the ternary dispersion of **A1**-FIrpic-Dec showed a particle size of 871±28 nm (Figure 2-6), and this aggregate showed comparable particle size even in the absence of donor molecule (Figure. 2-7).

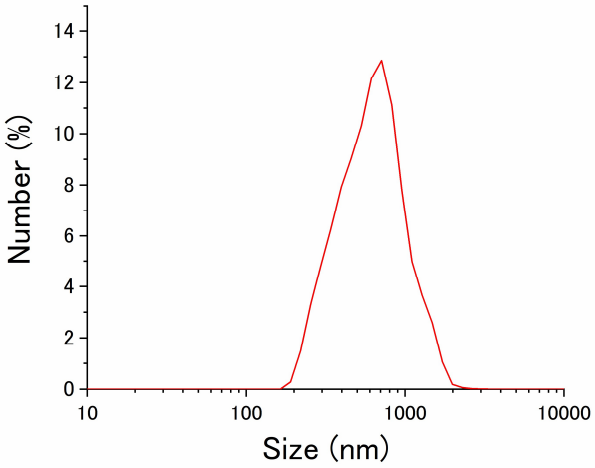

Figure 2-6. DLS profile of **A1**-FIrpic-Dec in water ([**A1**] = 10 mM, [FIrpic] = 100 μM, [Dec] = 80 mM). The result showed a particle size of 871±28 nm

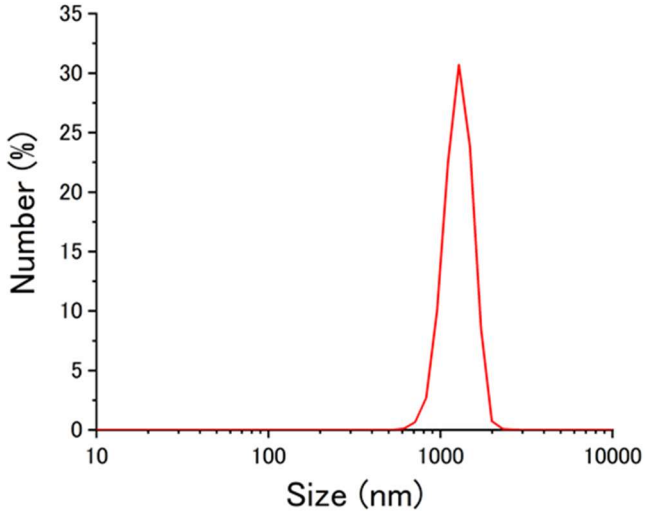

Figure 2-7. DLS profile of **A1**-Dec in water ([**A1**] = 10 mM, [Dec] = 80 mM).The data showed a particle size of 1282±40nm. This result suggests that the particle size is the same scale before and after encapsulation of FIrpic.

SEM observation results showed good agreement with DLS profile (Figure. 2-8). Under conditions without fatty acids, precipitation was observed as shown in Figure 2-5, and particles of around 1 μm were obtained by adding a large excess of fatty acids. From these results, it is thought that the excess fatty acids solubilize the aggregate with the structure shown in Figure 2-2 as the unit structure by surrounding it with the excess fatty acids.

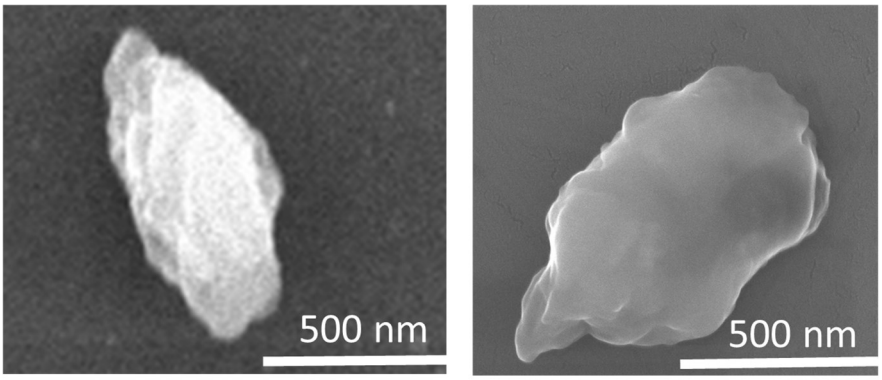

Figure 2-8. SEM images of ternary co-assembly of **A1**-FIrpic-Dec. The aqueous dispersion of **A1**-FIrpic-Dec ([**A1**] = 10 mM [FIrpic] = 100 μM [Dec] = 80 mM) was cast on a TEM grid and dried in air. Particles like these pictures were observed to be sparsely present.

The co-assembly of **A1** with excess Dec anions was further supported by the negative zeta potential of –24.7 mV observed for **A1**-FIrpic-Dec. Compared with the fluorescence peak at 358 nm of the molecularly-dispersed **A1** in methanol, a fluorescence spectrum of the **A1**-FIrpic-Dec ternary dispersion showed a redshift to 391 nm, which is still in the UV range (Figure 2-9).

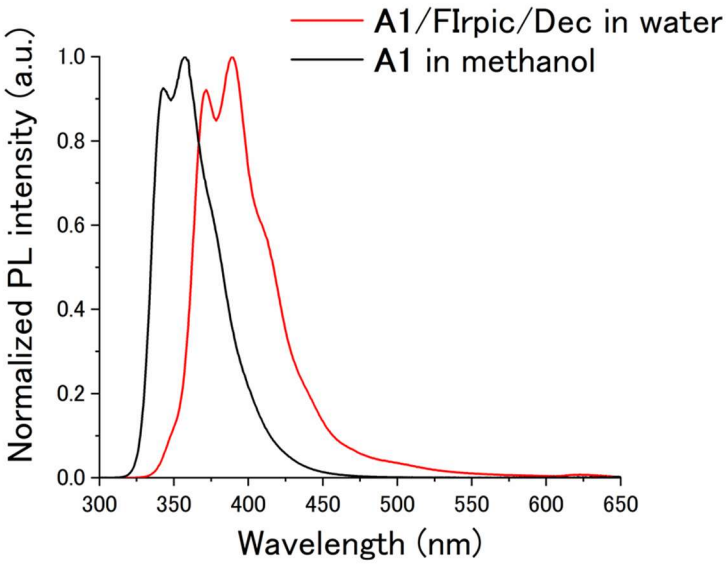

Figure 2-9. Fluorescence spectra of **A1** in methanol (black, [**A1**] = 0.25 mM, λ_{ex} = 241 nm) and **A1**-FIrpic-Dec in water (red, [**A1**] = 10 mM, [FIrpic] = 100 μM, [Dec] = 80 mM, λ_{ex} = 280 nm).

We also observed red-shifts in the excitation spectrum of aqueous **A1**-FIrpic-Dec as compared to that of **A1** in methanol (Figure 2-10). These results suggest the presence of excitonic interactions among the terphenyl chromophores in the aqueous co-assemblies.

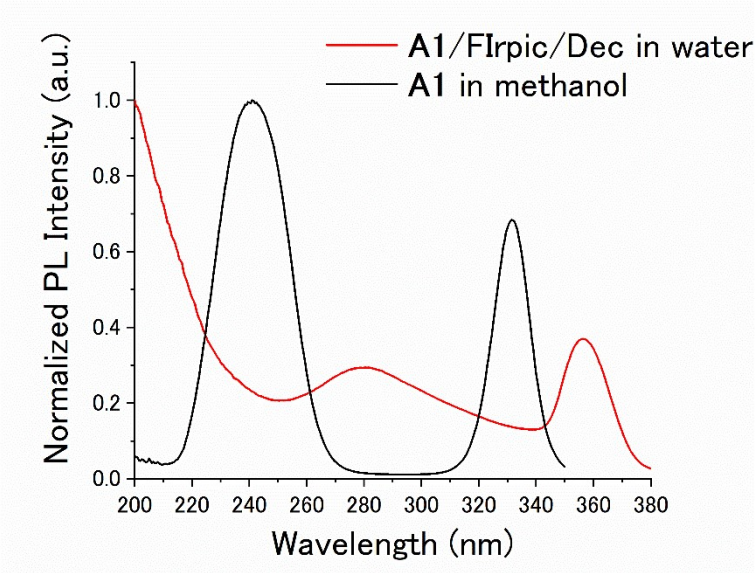

Figure 2-10. Excitation spectra of **A1** in methanol (black, [**A1**] = 0.25 mM, λ_{dt} = 360 nm) and **A1**-FIrpic-Dec in water (red, [**A1**] = 10 mM, [FIrpic] = 100 μM, [Dec] = 80 mM, λ_{dt} = 390 nm).

・2-3-4 TTA-UC property at deaerated condition

The TTA-UC properties of the A1-FIrpic-Dec ternary co-assemblies were then characterized in deaerated water. The aqueous dispersion of A1-FIrpic-Dec ([A1] = 10 mM, [FIrpic] =100 μM and [Dec] = 80 mM) was deaerated by repeated freeze-pump-thaw cycles. Under the irradiation of visible laser at 445 nm, the aqueous dispersion showed upconverted UV emission at around 390 nm (Figure 2-11).

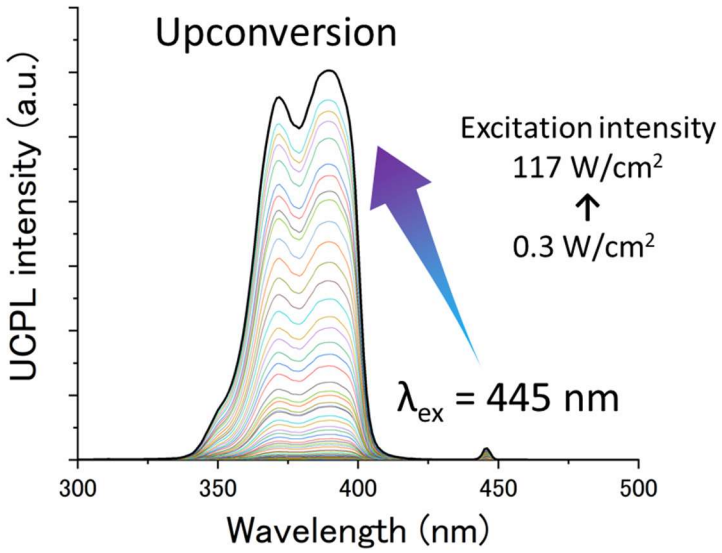

Figure 2-11. Photoluminescence (PL) spectra of **A1**-FIrpic-Dec in deaerated water ([**A1**] = 10 mM, [FIrpic] = 100 μM, [Dec] = 80 mM, λ_{ex} = 445 nm). Scattered excitation laser light was removed by 400 and 425 nm short-pass filters.

Double logarithmic plots of the UC emission intensity at 390 nm against the excitation intensity showed a slope change from 2 to 1, which is a typical characteristic of TTA-UC (Figure 2-12).[47-49]

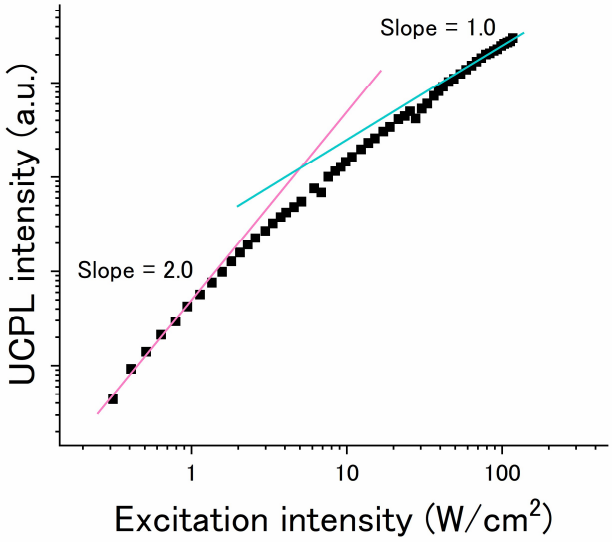

Figure 2-12. Excitation intensity dependence of UCPL intensity of **A1**-FIrpic-Dec in deaerated water at 390 nm. The red and blue lines are fitting results with slope 2.0 and 1.0, respectively.

Furthermore, the upconverted emission was observed for the microsecond scale, supporting the delayed fluorescence mechanism via the long-lived triplet state (Figure 2-13).

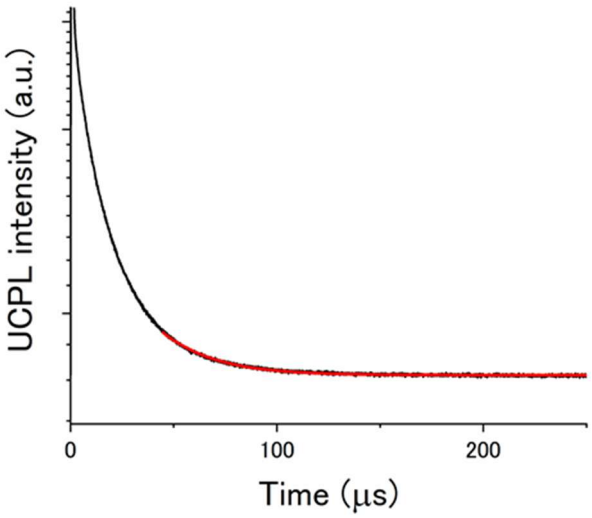

Figure 2-13. Photoluminescence (PL) spectra of **A1**-FIrpic-Dec in deaerated water ([**A1**] = 10 mM, [FIrpic] = 100 μM, [Dec] = 80 mM, λ_{ex} = 445 nm). Scattered excitation laser light was removed by 400 and 425 nm short-pass filters.

Although the TTA-UC efficiency was not high (0.1 % at 10 W/cm^2) compared with the previous vis-to-UV TTA-UC systems,[24-39] this is partly due to a reduced fluorescence quantum yield (~26%) in the aqueous co-assemblies. It is also possible that the deactivation of triplets occurred at strongly interacting sites.[50] The optimization of the chemical structure of amphiphilic acceptors and the co-assembly conditions to improve TTA-UC efficiency is an important future task.

・2-3-5 TTA-UC property at aerated condition

Significantly, the ternary **A1**-FIrpic-Dec co-assemblies showed a stable vis-to-UV TTA-UC emission even in air-saturated water (Figure 2-14).

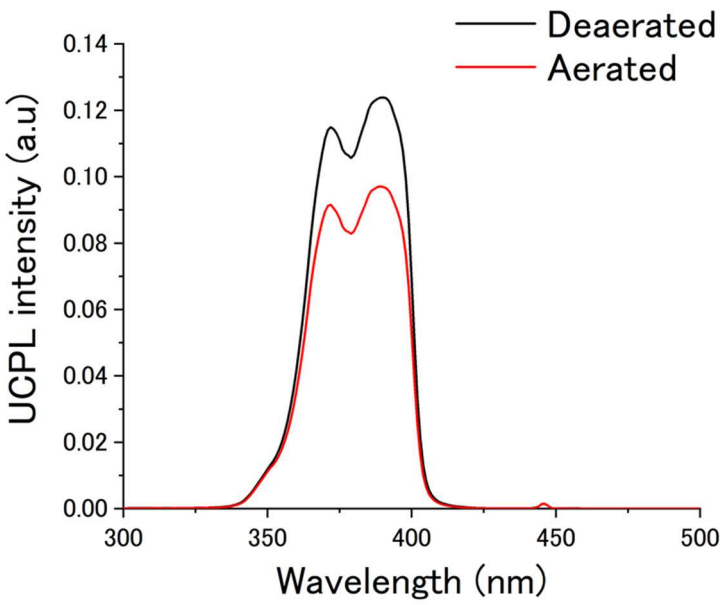

Figure 2-14. PL spectra of **A1**-FIrpic-Dec in deaerated (black) and aerated (red) water under 445 nm excitation ([**A1**] = 10 mM, [FIrpic] = 100 μM, [Dec] = 80 mM). Scattered excitation laser light was removed by 400 and 425 nm short-pass filters.

Oxygen-barrier efficiency (Φ_{OB}) was estimated by the time dependence of UC emission intensity at 390 nm. It was found that the UC emission was maintained for more than one hour even in aerated water (Figure 2-15).

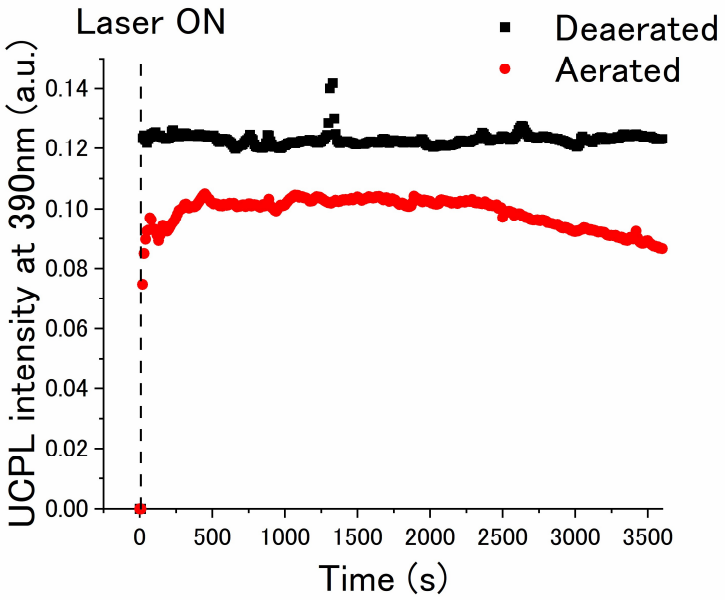

Figure 2-15. Time dependence of UCPL intensity of **A1**-FIrpic-Dec in deaerated (black) and aerated (red) water at 390 nm.

By comparing the time-averaged UC emission intensity of the degassed and aerated samples, the Φ_{OB} was calculated as $\Phi_{OB} = I_{UC,\ aerated} / I_{UC,\ deaerated} = 80\%$, which is comparable to our previous aqueous co-assembled system showing air-stable green-to-blue TTA-UC.[44] In our previous work, we have shown that the oxygen blocking ability can be endowed by enhancing the packing density of chromophores and alkyl chains in the aqueous co-assemblies. It is notable that such supramolecular crowding strategy which takes advantage of ion-paring-based co-assembly is generalized for the single-chained, bola-type acceptor amphiphiles that lead to the aqueous vis-to-UV TTA-UC even under the aerated conditions.

2-4 Conclusion

In this work, we showed the first example of air-stable vis-to-UV TTA-UC in water. The novel anionic amphiphilic acceptor **A1** was co-assembled with the donor Flrpic and the cationic lipid Dec in water. The ternary aqueous co-assemblies showed a high oxygen barrier efficiency Φ_{OB} of 80%. The current system clarified the generality of our previous supramolecular crowding strategy in which the enhancement in molecular packing density in aqueous co-assemblies endowed the remarkable oxygen blocking ability.[44] This work provides important design guidelines to protect air-sensitive species in water for various applications, including visible-light-driven water splitting.

2-5 References

1. A. Kudo and Y. Miseki, *Chem. Soc. Rev.*, 2009, **38**, 253-278.
2. S. Baluschev, T. Miteva, V. Yakutkin, G. Nelles, A. Yasuda and G. Wegner, *Phys. Rev. Lett.*, 2006, **97**, 143903.
3. T. N. Singh-Rachford and F. N. Castellano, *Coord. Chem. Rev.*, 2010, **254**, 2560-2573.
4. J. Zhao, S. Ji and H. Guo, *RSC Adv.*, 2011, **1**, 937-950.
5. J. H. Kim and J. H. Kim, *J. Am. Chem. Soc.*, 2012, **134**, 17478-17481.
6. A. Monguzzi, R. Tubino, S. Hoseinkhani, M. Campione and F. Meinardi, *Phys. Chem. Chem. Phys.*, 2012, **14**, 4322-4332.
7. Y. C. Simon and C. Weder, *J. Mater. Chem.*, 2012, **22**, 20817-20830.
8. K. Börjesson, D. Dzebo, B. Albinsson and K. Moth-Poulsen, *J. Mater. Chem. A*, 2013, **1**, 8521-8524.
9. S. H. C. Askes, A. Bahreman and S. Bonnet, *Angew. Chem., Int. Ed.*, 2014, **53**, 1029-1033.
10. R. Andernach, H. Utzat, S. D. Dimitrov, I. McCulloch, M. Heeney, J. R. Durrant and H. Bronstein, *J. Am. Chem. Soc.*, 2015, **137**, 10383-10390.
11. M. Häring, R. Pérez-Ruiz, A. J. von Wangelin and D. D. Díaz, *Chem. Commun.*, 2015, **51**, 16848-16851.
12. T. F. Schulze and T. W. Schmidt, *Energy Environ. Sci.*, 2015, **8**, 103-125.
13. J. Zhou, Q. Liu, W. Feng, Y. Sun and F. Li, *Chem. Rev.*, 2015, **115**, 395-465.
14. C. Fan, W. Wu, J. J. Chruma, J. Zhao and C. Yang, *J. Am. Chem. Soc.*, 2016, **138**, 15405-15412.
15. N. Yanai and N. Kimizuka, *Chem. Commun.*, 2016, **52**, 5354-5370.
16. S. P. Hill and K. Hanson, *J. Am.Chem. Soc*, 2017, **139**, 10988-10991.
17. Z. Huang and M. L. Tang, *J. Am. Chem. Soc.*, 2017, **139**, 9412-9418.
18. C. Duan, L. Liang, L. Li, R. Zhang and Z. P. Xu, *J. Mater. Chem. B*, 2018, **6**, 192-209.
19. C. Kerzig and O. S. Wenger, *Chem. Sci.*, 2018, **9**, 6670-6678.
20. W. Xu, W. Liang, W. Wu, C. Fan, M. Rao, D. Su, Z. Zhong and C. Yang, *Chem. Eur. J.*, 2018, **24**, 16677-16685.
21. D. Yang, P. Duan and M. Liu, *Angew. Chem., Int. Ed.*, 2018, **57**, 9357-9361.
22. L. Huang, E. Kakadiaris, T. Vaneckova, K. Huang, M. Vaculovicova and G. Han, *Biomaterials*, 2019, **201**, 77-86.
23. Z. Wang, J. Zhao, M. Di Donato and G. Mazzone, *Chem. Commun.*, 2019, **55**, 1510-1513.
24. W. Zhao and F. N. Castellano, *J. Phys. Chem. A*, 2006, **110**, 11440-11445.
25. T. N. Singh-Rachford, R. R. Islangulov and F. N. Castellano, *J. Phys. Chem. A*, 2008,

112, 3906-3910.

26. F. Deng, J. Blumhoff and F. N. Castellano, *J. Phys. Chem. A*, 2013, **117**, 4412-4419.
27. P. Duan, N. Yanai and N. Kimizuka, *Chem. Commun.*, 2014, **50**, 13111-13113.
28. M. Majek, U. Faltermeier, B. Dick, R. Pérez-Ruiz and A. J. von Wangelin, *Chem. Eur. J.*, 2015, **21**, 15496-15501.
29. X. Jiang, X. Guo, J. Peng, D. Zhao and Y. Ma, *ACS Appl. Mater. Interfaces*, 2016, **8**, 11441-11449.
30. J. Peng, X. Guo, X. Jiang, D. Zhao and Y. Ma, *Chem. Sci.*, 2016, **7**, 1233-1237.
31. N. Yanai, M. Kozue, S. Amemori, R. Kabe, C. Adachi and N. Kimizuka, *J. Mater. Chem. C*, 2016, **4**, 6447-6451.
32. K. A. El Roz and F. N. Castellano, *Chem. Commun.*, 2017, **53**, 11705-11708.
33. V. Gray, P. Xia, Z. Huang, E. Moses, A. Fast, D. A. Fishman, V. I. Vullev, M. Abrahamsson, K. Moth-Poulsen and M. Lee Tang, *Chem. Sci.*, 2017, **8**, 5488-5496.
34. M. Barawi, F. Fresno, R. Pérez-Ruiz and V. A. de la Peña O'Shea, *ACS Appl. Energy Mater.*, 2018, **2**, 207-211.
35. Q. Chen, Y. Liu, X. Guo, J. Peng, S. Garakyaraghi, C. M. Papa, F. N. Castellano, D. Zhao and Y. Ma, *J. Phys. Chem. A*, 2018, **122**, 6673-6682.
36. S. He, X. Luo, X. Liu, Y. Li and K. Wu, *J. Phys. Chem. Lett.*, 2019, **10**, 5036-5040.
37. S. Hisamitsu, J. Miyano, K. Okumura, J. K. H. Hui, N. Yanai and N. Kimizuka, *ChemistryOpen*, 2019, **8**, 1-5.
38. H. L. Lee, M. S. Lee, H. Park, W. S. Han and J. H. Kim, *Korean J. Chem. Eng.*, 2019, **36**, 1791-1798.
39. K. Okumura, N. Yanai and N. Kimizuka, *Chem. Lett.*, 2019, **48**, 1347-1350.
40. J. H. Kim, F. Deng, F. N. Castellano and J. H. Kim, *Chem. Mater.*, 2012, **24**, 2250-2252.
41. Q. Liu, B. Yin, T. Yang, Y. Yang, Z. Shen, P. Yao and F. Li, *J. Am. Chem. Soc.*, 2013, **135**, 5029-5037.
42. H. Kouno, T. Ogawa, S. Amemori, P. Mahato, N. Yanai and N. Kimizuka, *Chem. Sci.*, 2016, **7**, 5224-5229.
43. R. Haruki, H. Kouno, M. Hosoyamada, T. Ogawa, N. Yanai and N. Kimizuka, *Chem. Asian J.*, 2019, **14**, 1723-1728.
44. H. Kouno, Y. Sasaki, N. Yanai and N. Kimizuka, *Chem. Eur. J.*, 2019, **25**, 6124-6130.
45. R. J. Holmes, S. R. Forrest, Y. J. Tung, R. C. Kwong, J. J. Brown, S. Garon and M. E. Thompson, *Appl. Phys. Lett.*, 2003, **82**, 2422-2424.
46. F. E. Stanley, A. M. Warner, E. Schneiderman and A. M. Stalcup, *J. Chromatogr. A*, 2009, **1216**, 8431-8434.
47. A. Monguzzi, J. Mezyk, F. Scotognella, R. Tubino and F. Meinardi, *Phys. Rev. B*, 2008,

78, 195112.

48. Y. Y. Cheng, T. Khoury, R. G. C. R. Clady, M. J. Y. Tayebjee, N. J. Ekins-Daukes, M. J. Crossley and T. W. Schmidt, *Phys. Chem. Chem. Phys.*, 2010, **12**, 66-71.
49. A. Haefele, J. Blumhoff, R. S. Khnayzer and F. N. Castellano, *J. Phys. Chem. Lett.*, 2012, **3**, 299-303.
50. S. Hisamitsu, N. Yanai, H. Kouno, E. Magome, M. Matsuki, T. Yamada, A. Monguzzi and N. Kimizuka, *Phys. Chem. Chem. Phys.*, 2018, **20**, 3233-3240.

Chapter3

Singlet fission as a selective quantum state generator for nuclear hyperpolarization of biomolecules

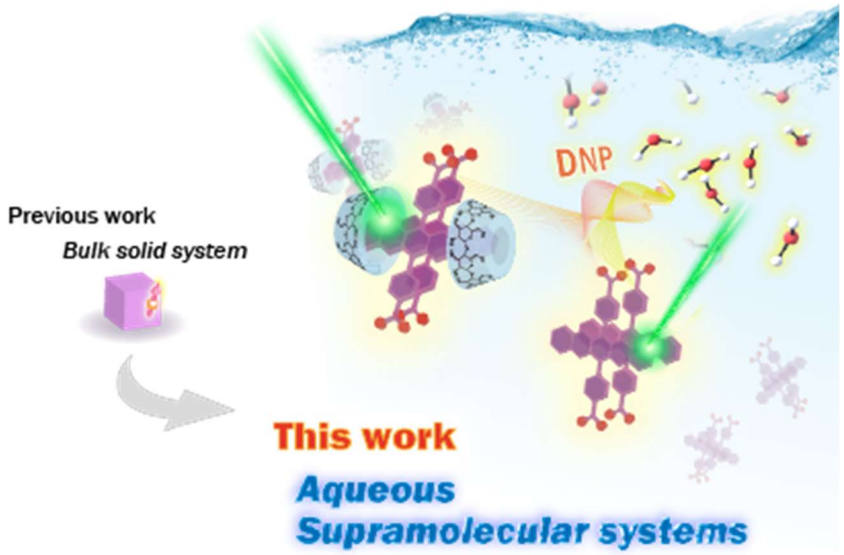

Abstract:

Singlet fission (SF), converting a singlet excited state into a spin-correlated triplet-pair state, is an effective way to generate a spin quintet state in organic materials. Although its application to photovoltaics as an exciton multiplier has been extensively studied, the use of its unique spin degree of freedom has been largely unexplored. Here, we demonstrate that the spin polarization of the quintet multiexcitons generated by SF improves the sensitivity of magnetic resonance of water molecules through dynamic nuclear polarization (DNP). We form supramolecular assemblies of a few pentacene chromophores and use SF-born quintet spins to achieve DNP of water-glycerol, the most basic biological matrix, as evidenced by the dependence of nuclear polarization enhancement on magnetic field and microwave power. Our demonstration opens a new use of SF as a "polarized spin generator" in bio-quantum technology.

Author:Yusuke Kawashima et al

Publication: Nature Communications

Publisher: Springer Nature

Date: Mar 1, 2023

3-1 Introduction

Photo-excited states of organic assemblies have brought a number of unique opportunities to optoelectronics, taking advantage of the dual nature of singlet and triplet molecular excitons [1]. In particular, singlet fission (SF) [2-12], which generates two triplet excitons from one singlet exciton, shows unique functions in terms of electron and spin degrees of freedom. SF is a multiexciton generation process that can potentially surpass the theoretical limit of a single-junction solar cell if the split excitons are harvested as free electrons and holes [5]. Its unique electron degree of freedom has attracted much attention and has been studied intensively for decades.

The basic SF process is as follows: the singlet exciton S_1 undergoes a spin-allowed ultrafast transition to a triplet-pair state with overall-singlet multiplicity, ^{1}(TT), followed by an intersystem crossing (ISC) to the highest spin multiplicity state, a *quintet* triplet-pair ^{5}(TT). When the molecular assembly is larger than two molecules, the triplet-pair states may dissociate into two free triplets [9, 13-16]. Note that the multiexcitonic nature offers a unique opportunity to construct quintet multiplicity owing to the presence of four half-filled orbitals. SF provides the effective method to create spin-polarized quintet states in organic systems without using heavy metals. However, how to use this unique quintet state has not been fully demonstrated.

We explore the unique spin degree of freedom of SF for quantum technologies [17, 18]. Among the five quintet spin sublevels, it has been reported that certain sublevels can be preferentially populated [13-16]. According to the *JDE* model, the $^5(TT)_0$ quintet state of chromophore dimers can be generated as a nearly pure quantum state by making the exchange interaction between two chromophores sufficiently large and by making the principal axes of the two chromophores parallel to each other and to the Zeeman field [19]. This model has explained well the experimental results of oriented crystalline samples [20, 21]. To date, the spin aspect of SF has only been used to explain the microscopic mechanisms of SF. Because organic spin materials have advantages with their extremely small size, down to nanometers, and excellent bio-compatibility, it is worthwhile to research applications of the unique quintet state in quantum information science (QIS) and quantum biotechnologies [17, 18 19].

Dynamic nuclear polarization (DNP) of biomolecules is one of the fields where polarized electron spins can play a pivotal role [22-29]. Nuclear magnetic resonance (NMR) and magnetic resonance imaging (MRI) are indispensable analytical techniques in modern life science and medicine, but their critically low sensitivity limits their applications. Many clinical trials of MRI diagnosis of cancer have been conducted by transferring the polarization of radical

electron spins, which are in thermal equilibrium at cryogenic temperatures near 1 K, to the nuclear spins of bioprobes, and then dissolving them and administering them to the human body [30]. However, the equipment is inevitably expensive and complicated because it requires cryogenic temperatures. Thus there is a strong need to develop DNP using polarized electron spins generated at higher temperatures. The triplet excited state generated by spin-preferential ISC from a photoexcited singlet has been used as a polarized spin source [31], but the polarization ratio of the triplet is usually far less than 100% [32]. However, SF has the potential to offer the ultimate polarization source because it can preferentially populate the $^5(TT)_0$ spin sublevel by appropriately controlling the structure and orientation of chromophore dimers [19].

This study demonstrates the first application of a SF-born polarized quintet state in DNP of water-based glass. Various small biomolecules and proteins can be hyperpolarized by dispersing them in an amorphous water-glycerol glass [22]. The key to successful DNP in a bio-oriented water-glycerol environment is to regulate the balance between aggregation and dispersion of SF molecular assembly; more than two molecules are needed for SF, but aggregation that is too large hampers the polarization transfer from the SF-generated electron spins to the nuclear spins. In essence, creating robust dimer aggregates would be promising to achieve both efficient SF and polarization transfer to the water-glycerol and eventually to dispersed biomolecules. We focus on a pentacene derivative, the most representative chromophore exhibiting SF [8]. We succeed in constructing discrete assemblies of pentacene moieties in water-glycerol using two distinct strategies: supramolecular assembly of an amphiphilic pentacene derivative and complexation with cyclodextrin (CD)[33]. The combination of ultrafast pump-probe transient absorption spectroscopy (TAS) and time-resolved electron spin resonance (ESR) measurements reveals that either pentacene assembly undergoes SF and generates electron spin polarization. We succeed in DNP of water-glycerol by transferring the polarization from quintet electron spins to nuclear spins upon microwave irradiation to satisfy the Hartmann-Hahn condition (Figure 3-1B, 3-1C). In addition, we show that the magnetic field dependence of nuclear polarization enhancement matches well with the ESR line shape and quintets with higher Rabi frequencies can cause DNP at lower microwave intensities than a conventional triplet [17], confirming the DNP based on the polarized quintet spins.

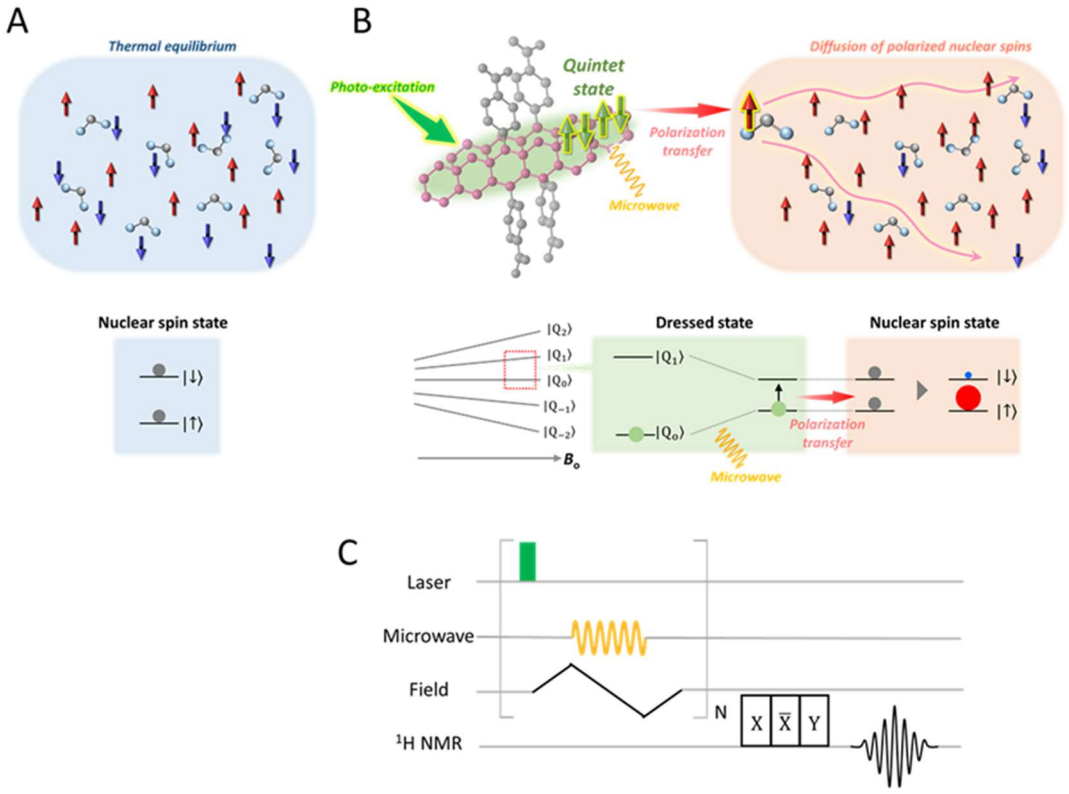

Figure. 3-1. Schematic illustration of DNP using SF-born quintet electron polarization. (A) Nuclear spins in the thermal equilibrium state. The red and blue arrows indicate α spin state and β spin state, respectively and the gray circles indicate the populations of each spin state. (B) Polarization transfer from electron spins in the quintet state ($|Q_0\rangle$ state, green arrows) generated by photo-induced SF to nuclear spins and the subsequent diffusion of hyperpolarized nuclear spins. The green circles indicate the populations of polarized quintet state. DNP increases the α spin population (red circle) and decrease the β spin population (blue circle), resulting in the hyperpolarized nuclear spin state (red square). (C) Pulse sequence of quintet/triplet-DNP.

3-2 Experimental section

・3-2-1 Materials

All reagents and solvents for measurements were used as received without further purification. Glycerol was purchased from Kishida chemical. Sodium 3-(Trimethylsilyl)-1-propanesulfonate was purchased from TCI. βCD and γCD were purchased from Wako Pure Chemical. Deuterium oxide and glycerol - d_8 were purchased from CIL. Deionized water was generated by Direct-Q UV (Merck Millipore). The synthesis and characterization of H_2PDBA have been reported in our previous work [34]. Analytical grade methanol and sodium hydroxide purchased from Wako Pure Chemicals were used to form the sodium salt NaPDBA in methanol, and the solvent was removed to form NaPDBA.

・3-2-2 Characterizations

^{1}H NMR (400 MHz) spectra were measured on a JEOL JNM-ECZ 400 and Bruker Ascend NMR 400 MHz using Sodium 3-(Trimethylsilyl)-1-propanesulfonate as the internal standard. UV-vis absorption spectra were measured by JASCO V-670 and V-770 spectrophotometers. Dynamic light scattering (DLS) was carried out using a DLS-8000DL (Otsuka Electronics).

・3-2-3 Pump-probe transient absorption

The fs-TAS and ns-TAS were conducted using home-built pump-probe setups. The light source was a Ti:sapphire regenerative amplifier (Spectra-Physics, Spitfire Ace, pulse duration: 120 fs, repetition rate: 1 kHz, pulse energy: 4 mJ/pulse, central wavelength: 800 nm) seeded by a Ti:sapphire femtosecond mode-locked oscillator (Spectra-Physics, Tsunami, pulse duration: 120 fs, repetition rate: 80 MHz, pulse energy: 10 nJ/pulse). The output of the amplifier was divided into two pulses. One of the outputs was led to a phase-matched BBO crystal for second harmonic generation and was used for the pump pulse (400 nm, 120 fs). The pump pulse was focused on the sample solution in a 1-mm path length quartz cell. The other output was focused on a sapphire crystal (3 mm thickness), and generated white light (450-750 nm) for the probe pulse. The angle between the pump and probe polarizations was set to the magic angle (~54.7 deg.). The probe pulse that passed through the sample solution was dispersed by a polychromator (JASCO, CT-10, 300 grooves / 500 nm), and the spectra were recorded by a multichannel detection system with a CMOS sensor (UNISOKU, USP-PSMM-NP).

The TAS measurements on the water-glycerol system were conducted under cryogenic temperature conditions. The glassy sample was prepared by the rapid cooling procedure and

was held in a cryostat for spectroscopy (UNISOKU, USP-203 Series) during the measurements. The output from the regenerative amplifier was led to an optical parametric amplifier system (Light Conversion, TOPAS-prime) to generate 500 or 600 nm pulses for the pump pulse of the fs-TAS. The output pulse from a nanosecond optical parametric oscillator system (EKSPLA, NT220) was employed for the pump pulse with a wavelength of 500 or 600 nm for the ns-TAS. We chose the lower excitation photon energy to suppress excess energy and transient heating in the excitation process because the glassy state was crystalized when too much heat was caused by photoexcitation. The probe white light was generated from the output of the Ti:sapphire amplifier focused on a sapphire crystal. The probe pulse passed through the sample solution was dispersed by a polychromator (JASCO, CT-10, 300 grooves / 500 nm), and the spectra were recorded by a multichannel detection system with a CMOS sensor (UNISOKU, USP-PSMM-NP). The recorded data were analyzed using a home-build program based on Python.

・3-2-4Time-resolved ESR setup and experiment

The time-resolved ESR measurement was performed on a home-built spectrometer (Figure 3-2), which has been described in our previous report [35].

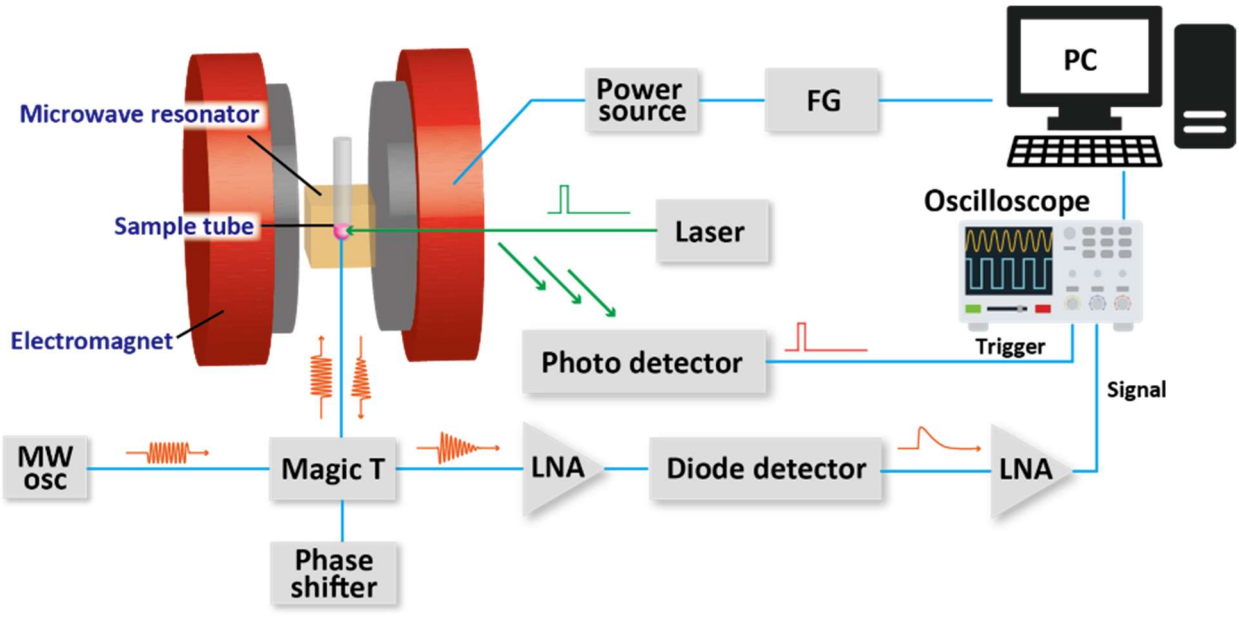

Figure 3-2. Setup for time-resolved ESR. LNA: low noise amplifier; MW osc: microwave oscillator; FG: function generator.

The samples were inserted into the dielectric resonator inside of an electromagnet (MC160-60G-0.8T, Takano Original Magnet) which is controlled by a function generator (33500B, Keysight). The sample was photo-excited by using a pulsed laser (Tolar-527, Beamtech Optronics). The pulse width, maximum repetition rate and maximum power of this laser are 200 ns, 5 kHz and 400 W, respectively. For samples, the repetition rate and the power of the laser were set to 100 Hz and 0.3 W.

A microwave was generated with the power of ~10 μW (SG24000H, DS Instruments) and amplified by using a power amplifier (ALN0905-12-3010, WENTEQ Microwave Corp), then converted to DC with a diode detector (DHM185AB, Herotek). ESR signal was also amplified and the noise was cut off by using two amplifiers (SA-230F5, NF ELECTRONIC INSTRUMENTS and 5305 differential amplifiers, NF ELECTRONIC INSTRUMENTS). The ESR signal was detected by an oscilloscope (DSOX3024T, Keysight). The temperature was controlled by flowing cold nitrogen gas into the microwave cavity.

The dielectric resonator was fabricated as shown in Figure 3-3. A ring-shaped dielectric ceramic (M29, MARUWA) with an outer diameter of 6.8 mm, an inner diameter of 2.1 mm, and a thickness of 2.5 mm was used. The hole with diameter of 14 mm was made on the copper blocks and closed with two copper clad laminate (CCL) boards to insert the dielectric ceramic. There is a hole with diameter of 2.1 mm on the top side CCL boards to insert the sample, and there are three holes on the center of front, back and side of copper blocks for microwave irradiation, laser irradiation and flowing the gas for temperature control with diameter of 8 mm, 6 mm and 5 mm, respectively. Two dielectric ceramics were hold by PTFE in the center of resonator. The waveguide was attached to the front of the resonator and a small copper plate, placed between the waveguide and the resonator, was controlled by a PTFE screw to adjust the microwave reflectivity. The resonance frequency of the fabricated cavity resonator was 9 GHz.

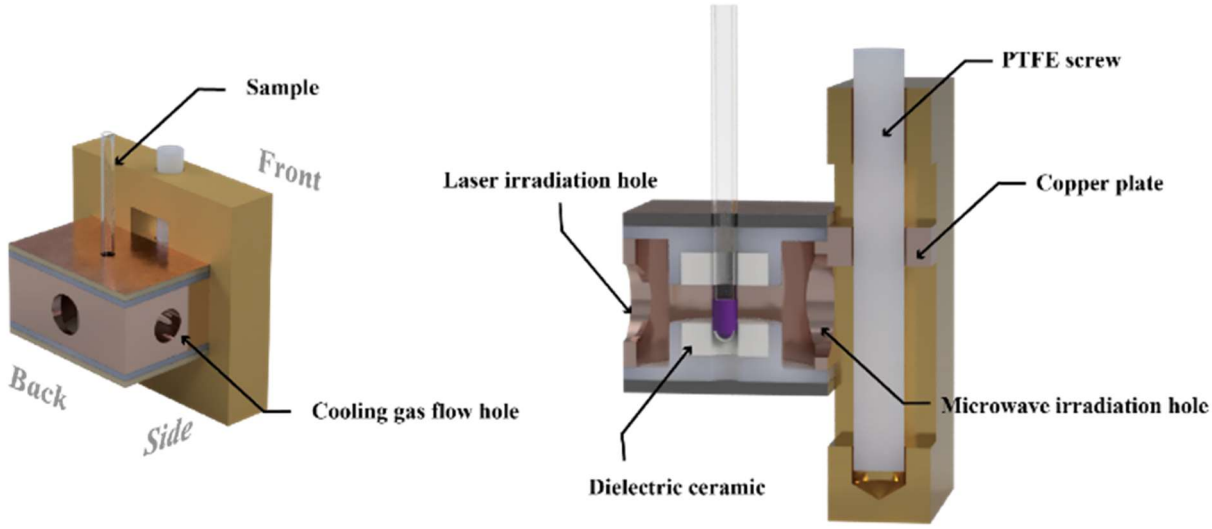

Figure 3-3. The cavity resonator in the time-resolved ESR setup. Overall view (left) and cross-sectional view (right).

ESR spectra were analyzed in Matlab version R2019b Update 8 (The Mathworks, Inc.) using the computational model shown in the previous report [16]. The polarization of the triplet state was assumed to be generated by only spin–orbit ISC, suggesting that no triplet dissociations occurred from the dimer. The spectra derived from quintet state were simulated by two strongly coupled TT conformations (TT_A and TT_B) which has different orientations and *J*-coupling. The fitting parameters are summarized in Figure 3-4 and Table 3-1, 3-2.

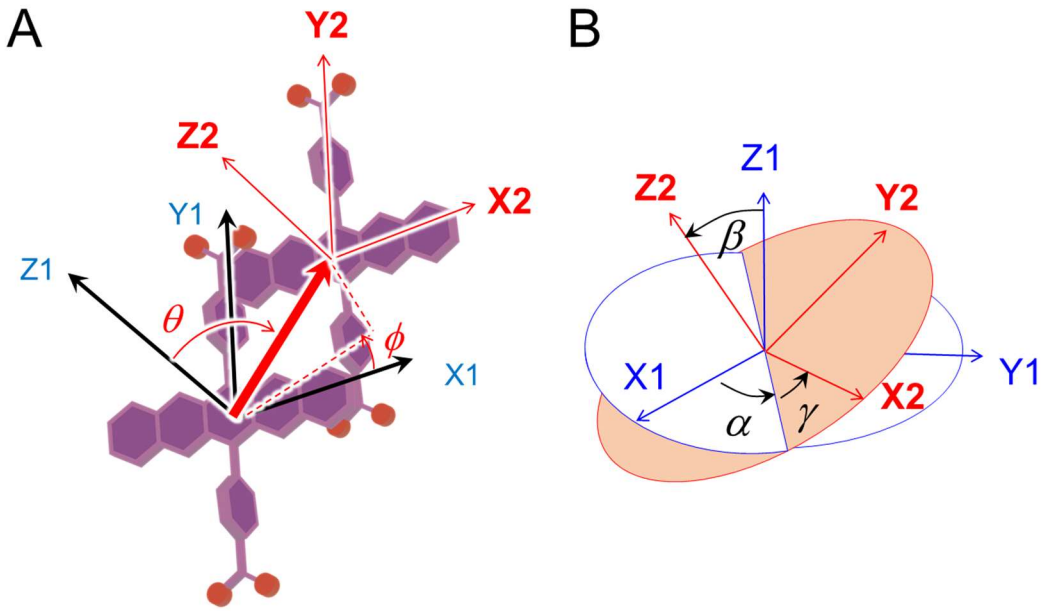

Figure 3-4. Angles defined for geometry of the triplet pair for the ZFS principal axes represented by X1, Y1, Z1 for triplet 1 and by X2, Y2, Z2 for triplet 2 in the TT multiexciton. (A) Polar angles, (θ, φ) and (B) Euler angles, (α, β, γ).

Table 3-1. Fitting parameters used for ISC-born triplet in the time-resolved ESR spectra (Figure 3-32 and 3-35).

State	Relative populations	*D* /MHz	*E* /MHz
NaPDBA	$T_x = 0.09$ $T_y = 0.91$ $T_z = 0$	1380	-20
NaPDBA-βCD	$T_x = 0.09$ $T_y = 0.91$ $T_z = 0$	1410	-15
NaPDBA-γCD	$T_x = 0.09$ $T_y = 0.91$ $T_z = 0$	1380	-15

Table 3-2. Fitting parameters used for SF-born quintet in the time-resolved ESR spectra (Figure 3-32 and 3-35).

State		Populations [a]	J /GHz	D /MHz	E /MHz	D_{SS} /MHz	Euler angles [b] /degrees	Polar angles [b] /degrees	$\tilde{\nu}_{vib}$ /cm^{-1}	k_{REC} /s^{-1} [c]
NaPDBA	TT_1	$Q_{+2} = 0.118$ $Q_{+1} = 0.024$ $Q_0 = 0.099$ $Q_{-1} = 0.027$ $Q_{-2} = 0.133$	-40	1180	-20	-120	$\alpha = 0$ $\beta = 0$ $\gamma = 0$	$\theta = 35$ $\varphi = 0$	21.5	1.0×10^6
	TT_2		-8				$\alpha = 90$ $\beta = 20$ $\gamma = -90$			-
NaPDBA-γCD	TT_1	$Q_{+2} = 0.087$ $Q_{+1} = 0.008$ $Q_0 = 0.074$ $Q_{-1} = 0.009$ $Q_{-2} = 0.103$	-60	1180	-20	-150	$\alpha = 0$ $\beta = 0$ $\gamma = 0$	$\theta = 35$ $\varphi = 0$	21.5	2.0×10^6
	TT_2		-20				$\alpha = 90$ $\beta = 10$ $\gamma = -90$			-

a) These values were obtained as ensemble averaged sublevel populations for the field orientations perpendicular to the Z principal axis of the zero-field splitting interaction of the triplet molecule in the multiexciton at $t = 0.4$ μs. This procedure was undertaken because the $^5(TT)_0 \rightarrow {}^5(TT)_1$ microwave transition in Figure 3-32 C-D was utilized for the DNP experiments and is dominantly contributed by these field orientations to satisfy the microwave resonance at the field strength. The residual populations were obtained in the excited complexes, as follows: $S_0S_0 = 0.541$, $^1(TT) = 0.057$ for NaPDBA and $S_0S_0 = 0.646$, $^1(TT) = 0.074$ for NaPDBA-γCD. To fit the entire ESR spectra, however, computed anisotropic spin polarization patterns were averaged for all the possible field orientations to obtain the powder-pattern spectra, as reported previously in Ref.(16) of the main text. Fitting parameters are also detailed in Ref.(16).

b) The polar angles correspond to θ and φ in Fig. S31A, and the Euler angles correspond to α, β and γ in Figure 3-34 B.

c) The singlet recombination constant k_{REC} represents the rate of singlet TT dimer $^1(TT)$ deactivation to the ground state. $^1(TT)$ and $^5(TT)$ are assumed to be in equilibrium. The k_{REC} value was estimated based on change in ESR signal intensity from immediately after photoexcitaton to 2-3 μs later. The change of ESR signal intensity was well explained with k_{REC} of 1.0×10^6 s^{-1} for NaPDBA and 2.0×10^6 s^{-1} for NaPDBA-γCD.

･3-2-5 Triplet-DNP setup and experiment

DNP experiment was carried out on a home-built spectrometer (Figure 3-5), which has been described in our previous report [35]. It consists of electromagnet (MC160-60G-0.8T, Takano Original Magnet), microwave resonator, coil for magnetic field sweep and pulsed laser. Sequence control and NMR signal detection were performed using the OPENCORE NMR spectrometer [36].

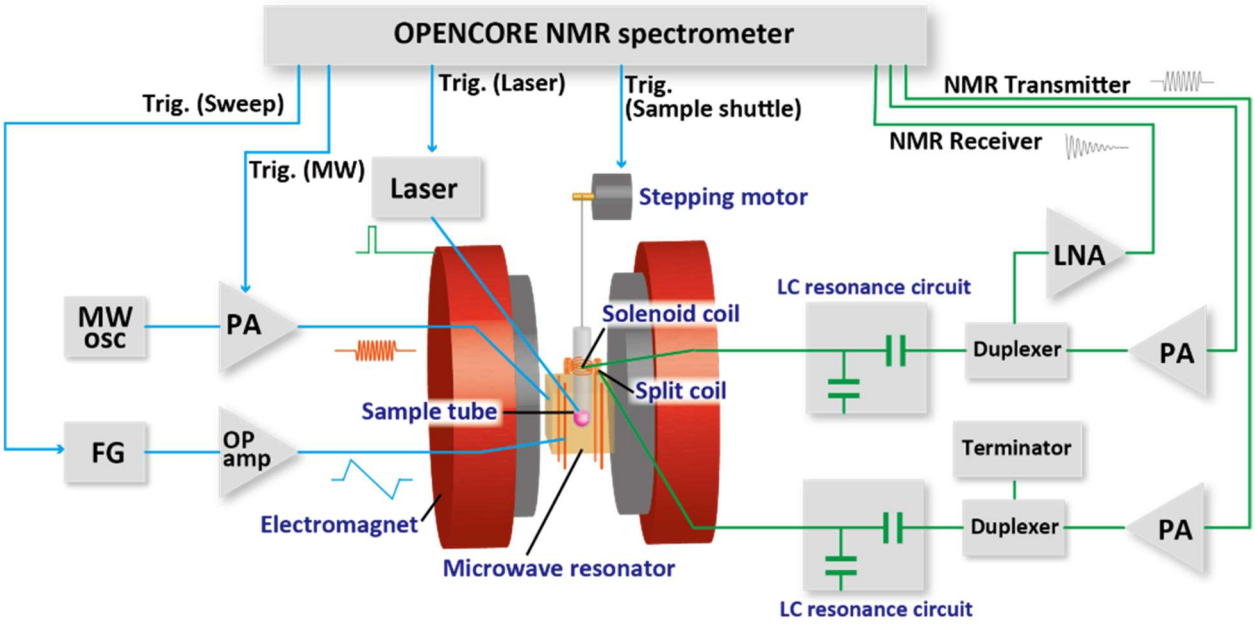

Figure 3-5. Setup for triplet-DNP. PA: power amplifier; MW osc: microwave oscillator; FG: function generator; Trig.: TTL trigger signal; LNA: low noise amplifier.

The cavity was fabricated as shown in Figure 3-6. The hole with diameter of 21.5 mm was made on the copper blocks and closed by two CCL boards to adjust the resonant frequency of Ku-band. There is a hole with diameter of 5 mm on the top side CCL boards to insert the samples, and there are three holes on the center of front, back and side of copper blocks for microwave irradiation,, laser irradiation and flow of cold nitrogen gas to keep the sample temperature, with diameter of 7 mm,, 6 mm and 5 mm, respectively. The microwave reflectivity was adjusted by a Teflon screw as with time-resolved ESR setup. the resonance frequency of the fabricated cavity resonator was about 17.3 GHz. 1-turn saddle coil, four enamel wires which were connected to each other, were inserted into the resonator to surround the sample. An induced magnetic field was applied to the sample by a current flowing in the copper wire, and the induced field direction is parallel to the static magnetic field. The magnetic field was swept from a high field to a low field over a few tens of

microseconds. The coils for the NMR detection were installed on the top of the resonator. The coil was made by winding enameled wire. The oscillating magnetic field from the coil and the static magnetic field from the electromagnet were arranged perpendicular to each other.

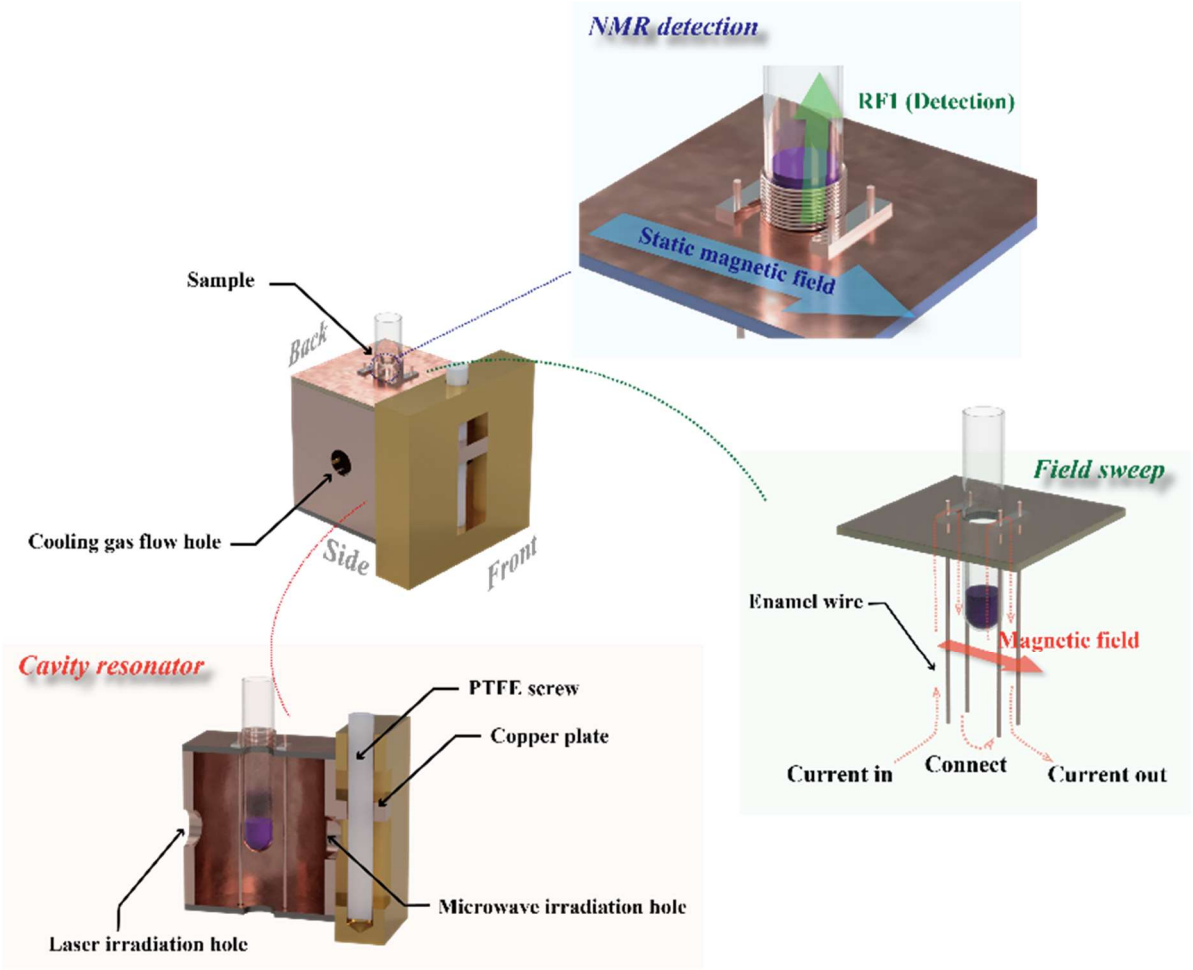

Figure 3-6. The resonator used in triplet-DNP. NMR detection part (blue), field sweep part (green) and cavity resonator (red).

The sample was photo-excited by using pulsed laser (Tolar-527, Beamtech Optronics) and kept the temperature by flowing cold nitrogen gas, same as time-resolved ESR setup. For triplet-DNP experiments, the repetition rate and the power of the laser were set to 500 Hz and 1.5-2.7 W. The continuous microwave was generated (SG24000H, DS Instruments) and converted to a pulsed wave using a pin diode (S1517D, L3HARRIS). The pulsed wave was amplified by using a power amplifier (AMP4081P-CTL, EXODUS ADVANCED COMMUNICATIONS) and sent into the resonator by a coaxial cable with the transmission loss of ~1dB. The magnetic field sweep was performed by applying an amplified triangular wave to a copper wire built in the resonator (Figure 3-6). The source triangular wave was generated from the function generator (WF1974, NF ELECTRONIC INSTRUMENTS). This triangular wave was amplified tenfold using an operational amplifier (137-PA05, Apex Microtechnology) and applied to the copper wire to reach a maximum of ±50 V. NMR signals were obtained by OPENCORE NMR spectrometer. The solenoid coil was used as NMR probe coil and mounted on the top of resonator (Figure 3-6). The sample was rifted up to the probe coil by using stepping motor within 1 s before NMR detection. In the case of protons in solid samples, a magic echo sequence was used because the short T_2 relaxation time and strong dipole interaction make it difficult to detect them with ordinary single pulses or spin echoes. The sweep width of the magnetic field when performing the ISE sequence is shown in SI. According to Figure 3-7, a voltage application of 1 V generates a magnetic field of 0.2 mT from the field sweep circuit. Thus, a 50 V sweep in the ISE sequence in this study corresponds to a 10 mT sweep. This value is narrow enough to selectively use only one ESR peak for DNP.

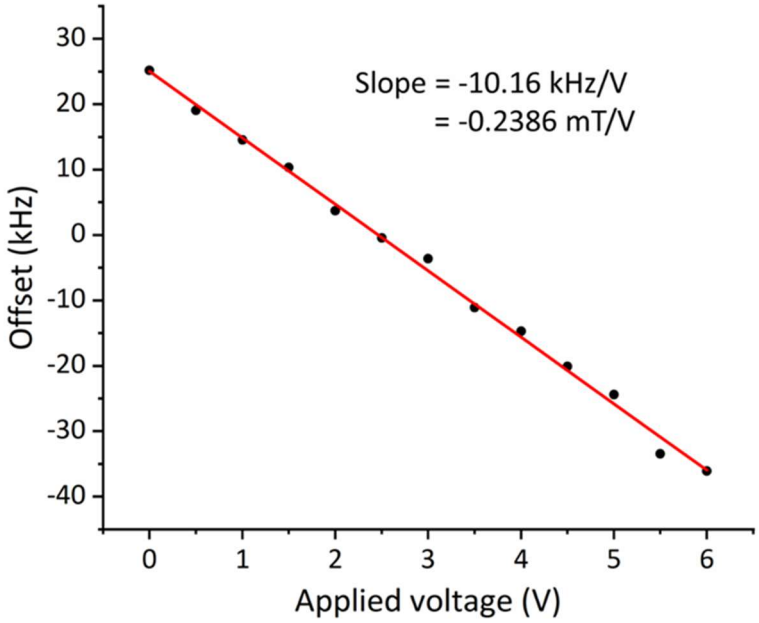

Figure 3-7. Offsets from the NMR resonance frequency at 27.98 MHz when various voltages are applied to the field sweep circuit. Deionized water was used for NMR measurement. A 50 V sweep in the ISE sequence in this study corresponds to a 10 mT sweep.

・3-2-6 Molecular dynamics simulations.

All-atom MD simulations in this study were performed by using the MD program GROMACS 2016.3. In the initial structure of the systems of NaPDBA in water : glycerol = 1 : 1 ([NaPDBA] = 1 mM [βCD] = 5 mM, [NaPDBA] = 1 mM, [γCD] = 5 mM, and [NaPDBA] = 5 mM), the complexes of NaPDBA with β/γCD or NaPDBA molecules were assembled close to each other and solvents and isolated β/γCD were placed in the surrounding space to fill the cubic MD cell. For the system of NaPDBA in water ([NaPDBA] = 1 mM [βCD] = 5 mM, [NaPDBA] = 1 mM, and [γCD] = 5 mM), the complexes and isolated β/γCD molecules were randomly inserted in the MD cell filled with water molecules. The number of molecules in each system is listed in Table 3-3. The generalized Amber force field [37] parameters were used for the force field parameters of NaPDBA, βCD, glycerol, and γCD and the TIP4P-Ew [38] model was used for the water molecules. As NaPDBA is composed of sodium ion and $PDBA^-$, their partial atomic charges were separately assigned. The atomic charges of $PDBA^-$, βCD, and γCD were calculated using the restrained electrostatic potential (RESP) [39] methodology, based on DFT calculations (B3LYP/6-31G(d,p)) using the GAUSSIAN 16 revision C01 program. (Gaussian, Inc., Wallingford CT, 2016)

Table 3-3. Number of molecules used for each MD simulations.

System	Number of molecules			
	NaPDBA	β/γCD	water	glycerol
NaPDBA in water	20	0	167054	0
NaPDBA in water-glycerol	20	0	74487	18500
NaPDBA-βCD in water-glycerol	4	20	97423	24300
NaPDBA-γCD in water-glycerol	4	20	97055	24300
NaPDBA-βCD in water	4	20	215005	0
NaPDBA-γCD in water	4	20	214845	0

In the present MD simulations, preequilibration and equilibration runs at room temperature (300 K) were sequentially carried out after the steepest energy minimization. The pre-equilibration and equilibration for the 2:2 inclusion complex of NaPDBA-γCD in water-glycerol at a lower temperature (243 K) were performed after the equilibration at room temperature. During the 5 ns preequilibration, the temperature and pressure of the system were kept constant using Berendsen thermostat and barostat [40] with the relaxation times of 0.2 and 2.0 ps, respectively. The equilibration was run for 20 ns using the Nosé-Hoover thermostat [41] and Parrinello-Rahman barostat [42] with the relaxation times of 1.0 and 5.0 ps, respectively. The pressure of the system for all MD simulations was kept at 1 bar. All bonds connected to hydrogen atoms were constrained with LINCS [43] algorithm. The time step of preequilibration and equilibration was set to 2 fs. The long-range Coulomb interactions were calculated with the smooth particle-mesh Ewald method [44] with a grid spacing of 0.30 nm. The real space cutoff for both Coulomb and van der Waals interactions was 1.2 nm.

The PMF for pulling away one of γCD forming the complex with NaPDBA were calculated for the quantitative comparison of the stability of the complex in water-glycerol between NaPDBA-γCD at 300 K and 243 K. According to the previous study[45], the PMF for each

system was obtained from a series of umbrella sampling (US) simulations, where the energy minima of their umbrella potentials were located at equal intervals along the direction of pulling γCD and the calculated probability density distributions were overlapped. For preparing the initial positions of two series of the US simulations, nonequilibrium steered MD simulations were performed using the structure after the 20 ns equilibration runs. The center of the mass of one molecule of γCD molecules forming the complex was pulled away in one direction using an umbrella potential with a force constant of 1,000 kJ/mol/nm^2. The pulling rate was 0.35 nm/ns and 0.80 nm/ns for NaPDBA-γCD in water-glycerol at 300 K and 243 K, respectively. During the 3 ns steered MD simulations using the Nosé-Hoover thermostat and Parrinello-Rahman barostat, the atoms of NaPDBA except sodium ions and hydrogen atoms were constrained to the intial positions by a harmonic potential with a force constant of 1,000 kJ/mol/nm^2. In the US simulation with the structures selected from the trajectory of the steered MD run, the 1 ns preequilibration run using the Berendsen thermostat and barostat and the 2 ns equilibration run using the Nosé-Hoover thermostat and Parrinello-Rahman barostat were performed. The number of the US simulations was 6 both for NaPDBA-γCD at 300 K and at 243 K. The force constant of the umbrella potential used in the US simulations was also 1,000 kJ/mol/nm^2. The values of the PMF were calculated from each set of the US simulations by the weighted histogram method (WHAM) [46, 47].

3-3 Results and discussion

• 3-3-1 Evaluation of aggregate formation of pentacene derivative NaPDBA

To construct supramolecular assemblies showing SF, we used our previously developed amphiphilic sodium 4,4′-(pentacene-6,13-diyl)dibenzoate (NaPDBA, Figure 3-8A): a hydrophobic pentacene modified with hydrophilic carboxyl groups. We molecularly dispersed 1-mM NaPDBA in methanol and obtained an absorption peak at 593.5 nm. In water-glycerol, the absorption peak was clearly red-shifted to 604 nm, suggesting the formation of supramolecular assemblies (Figure 3-8B).

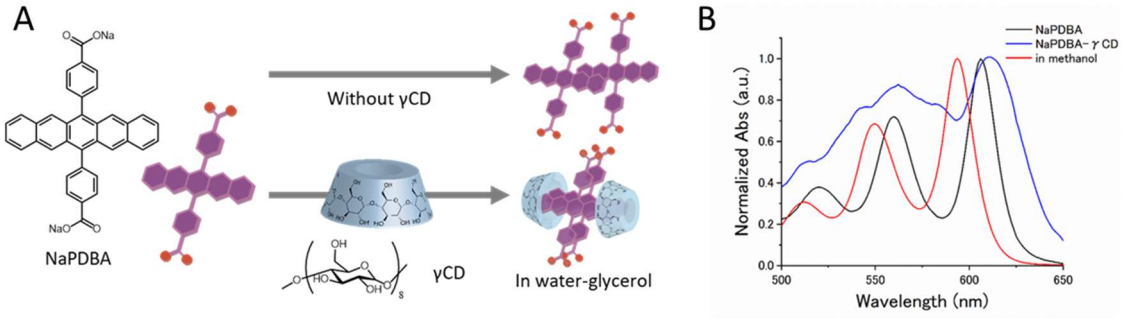

Figure 3-8. Schematic illustration of DNP using SF-born quintet electron polarization. (A) Molecular structures of NaPDBA and γ-cyclodextrin (γCD) and supramolecular assembly of only NaPDBA and the NaPDBA-γCD inclusion complex. (B) Absorption spectra of NaPDBA in water-glycerol at 143 K (black), NaPDBA-γCD in water-glycerol (1:1) at 143 K (blue), and NaPDBA in methanol at room temperature (red). The concentrations of NaPDBA and γCD were 1 mM and 5 mM, respectively.

We adjusted the mixing ratio of water and glycerol and used a 1:1 mixture by volume because it maintains the glassy state in the DNP-relevant condition, i.e., low temperature under laser irradiation. Molecular dynamics (MD) simulation was performed for an initial structure of 20 molecules of NaPDBA in close proximity to each other in water-glycerol. The simulation showed that the structure split into multiple dimers and a few monomers (Figure 3-9A,B).

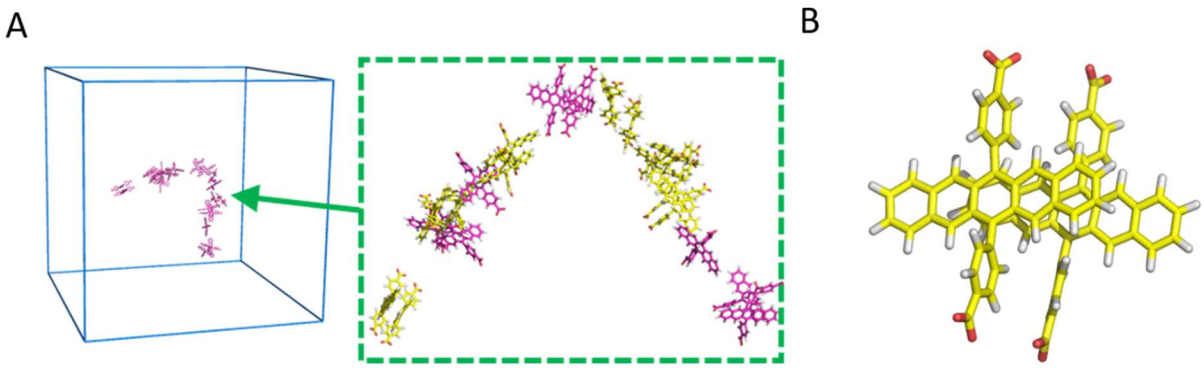

Figure 3-9. MD simulation of the supramolecular assemblies. (A,B) MD simulation snapshots of NaPDBA ([NaPDBA] = 1 mM) in water-glycerol (1:1) at 300 K. Parallel oriented dimers are shown in yellow.

Figure 3-10 shows the time variation of the distance between the centers of the mass (d_{COM}) of pentacene and the angle (θ) between d_{COM} and the nearest distance between the pentacene units (d_{min}) obtained from the MD simulations of NaPDBA in water-glycerol at 300 K. The distance between pentacene units is relatively far with various orientations, which probably gave a slightly red-shifted and sharp absorption peaks.

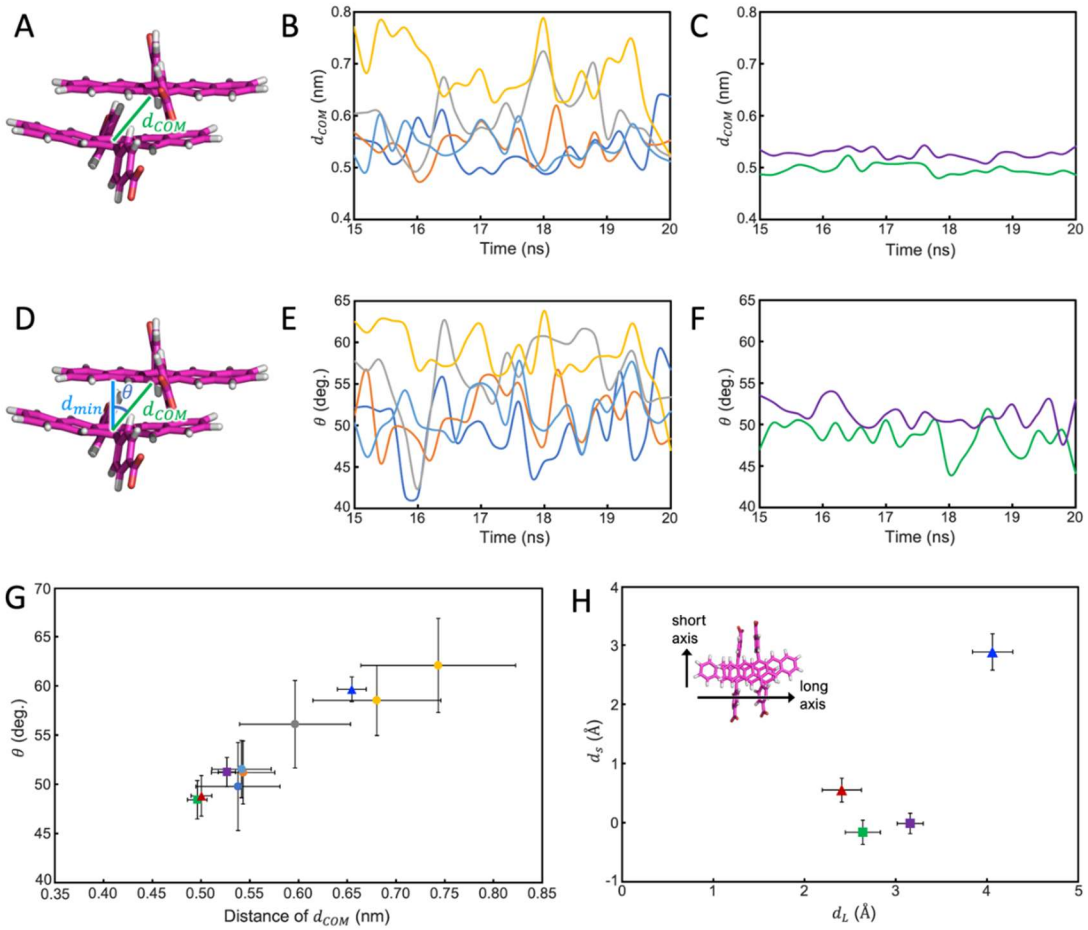

Figure 3-10. (A) Definition of distance between the pentacene centers of the mass (d_{COM}) and time dependences of d_{COM} of (B) NaPDBA in water-glycerol at 300 K and (C) NaPDBA-γCD in water-glycerol at 243 K for the last 5 ns of MD simulations. (D) Definition of angle between d_{COM} and d_{min} which denotes the nearest distance between the pentacene units (θ) and time dependences of θ of (E) NaPDBA in water-glycerol at 300 K and (F) NaPDBA-γCD in water-glycerol at 243 K for the last 5 ns of MD simulations. (G) Time averaged of d_{COM} and θ: circles and squares represent those values of NaPDBA in water-glycerol at 300 K and NaPDBA-γCD in water-glycerol at 243 K, respectively; triangles represent those values of NaPDBA-γCD in water-glycerol at 243 K using initial structure in which d_{COM} is different. (H) Time averaged of d_{COM} along the direction of the short axis (d_s) and of the long axis (d_L). The curves and plots in different colors indicate different pentacene dimers in the system. The horizontal and vertical bars show the standard deviations of time series of the values during the last 5 ns of MD simulations.

The formation of small dimeric structures agrees well with the fact that dynamic light scattering (DLS) measurements of NaPDBA in water-glycerol did not show any significant scattering intensity derived from large aggregates. However, DLS measurements showed that NaPDBA forms larger structures in pure water without glycerol (Figure 3-11). MD simulations also confirmed the formation of stable NaPDBA multimers in water (Figure 3-12). The addition of glycerol may have weakened the hydrophobic interactions between NaPDBA monomers and prevented the formation of larger aggregates, leading to the formation of NaPDBA dimers[48].

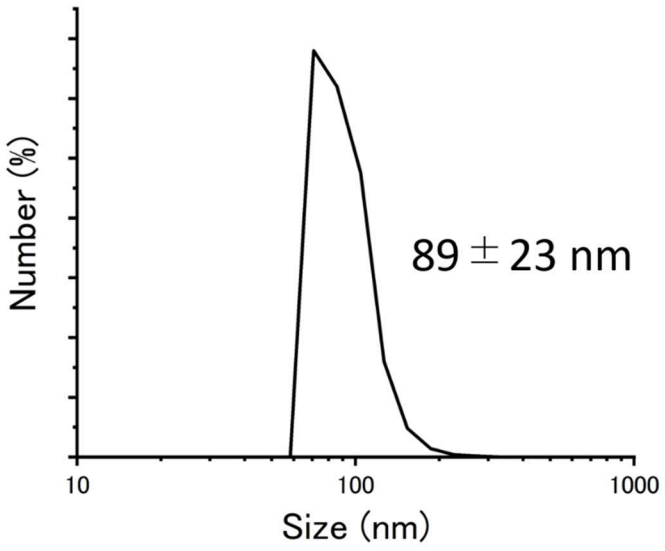

Figure 3-11. DLS profile of NaPDBA in water ([NaPDBA] = 1 mM). [NaPDBA] = 1 mM dispersion was degassed by freeze pump thew cycle prior to the measurement. The data showed a particle size of 89±23 nm.

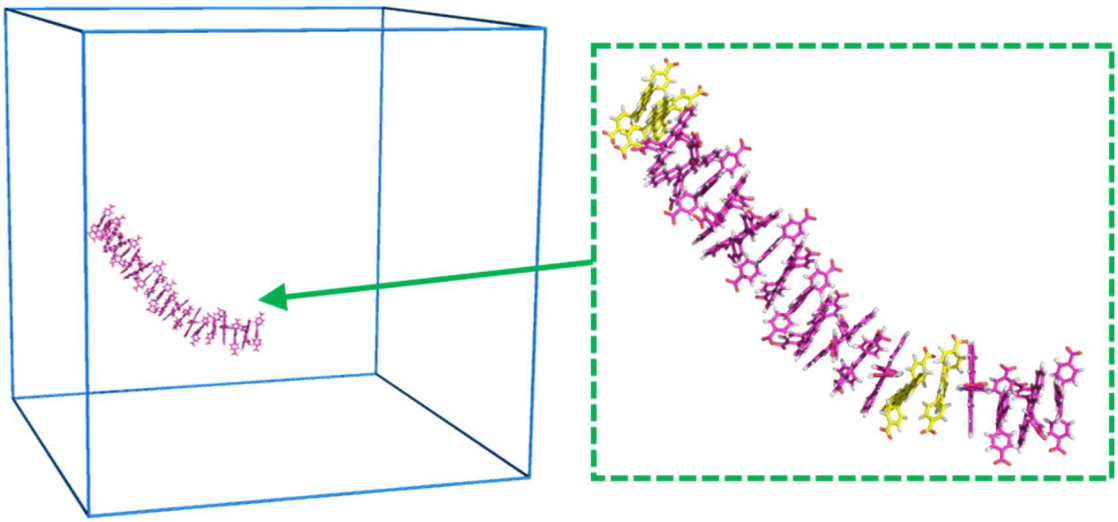

Figure 3-12. MD simulation snapshots of NaPDBA in water at 300 K. Parallel oriented dimers are shown in yellow.

To systematically change the assembly structure and excitonic interaction between the pentacene moieties while using the same NaPDBA molecule, we added β-cyclodextrin (βCD) and γ-cyclodextrin (γCD) to NaPDBA in water-glycerol. βCD and γCD are cyclic oligosaccharides with seven and eight glucose subunits, respectively, and can host various hydrophobic compounds within their hydrophobic interiors. The addition of γCD did not change the absorption spectrum of NaPDBA at room temperature with an absorption peak at 604 nm (Figure 3-13). Notably, the absorption peak of NaPDBA was further red-shifted to 612 nm and broadened by cooling to 143 K after inclusion was allowed to fully progress by letting the solution stand at 243 K in the presence of γCD (Figure. 3-8B, 3-13). This suggests that the excitonic interaction between pentacenes was enhanced by the formation of the inclusion complex between NaPDBA and γCD at low temperature.

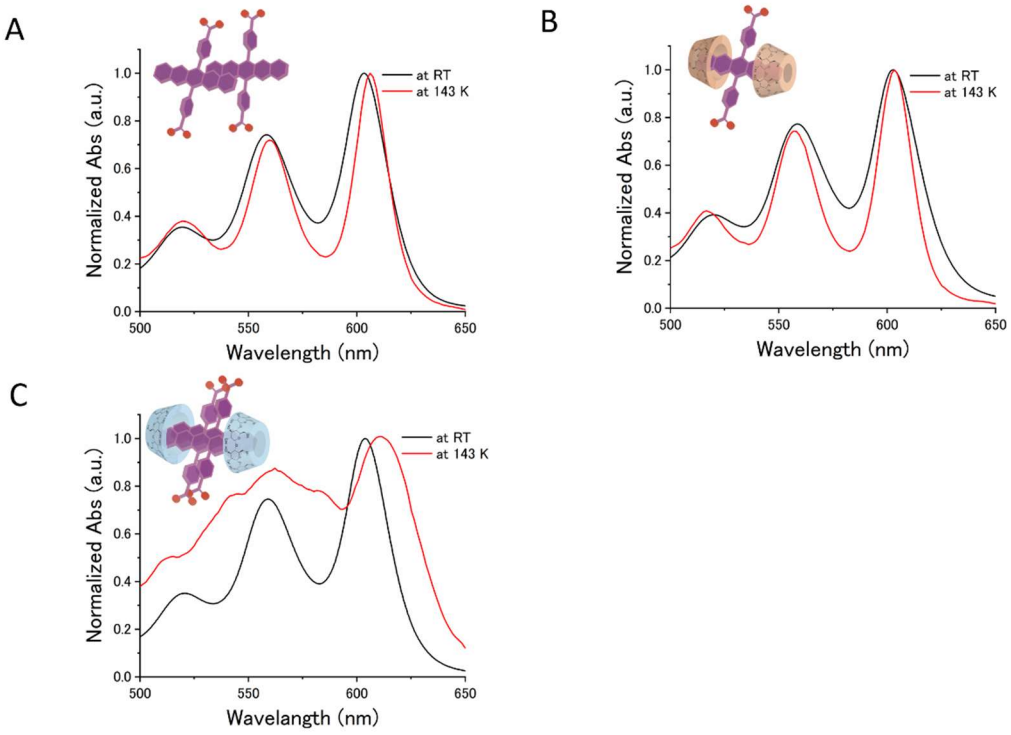

Figure 3-13. Absorption spectra of (A) NaPDBA, (B) NaPDBA and βCD, and (C) NaPDBA and γCD in water-glycerol (1:1) at room temperature (black lines) and 143 K (red lines) ([NaPDBA] = 1 mM [βCD] = 0-10 mM).

NMR studies of NaPDBA and γCD suggested that two molecules of γCD encapsulate a NaPDBA dimer, which is reasonable considering the large inner diameter of γCD and the strong excitonic interaction between pentacene moieties in the NaPDBA-γCD inclusion complex We first discuss the formation of inclusion complex of NaPDBA and βCD/γCD in water-glycerol. As the concentration of βCD was increased, the absorption peak of NaPDBA slightly blue-shifted from 604 nm to 601.5 nm while passing through the isobestic point (Figure 3-14), suggesting that the complexation of NaPDBA and βCD weakened the interaction between pentacene. Even in the presence of βCD, the absorption peak remained red-shifted from the that of molecularly dispersed NaPDBA in methanol (593.5 nm), suggesting that the inter-pentacene excitonic interaction was not completely eliminated probably due to the aggregation of the inclusion complex of NaPDBA and βCD. When the temperature was lowered to 143 K, the position of the absorption spectrum was red-shifted from 604 nm to 606 nm in the case of NaPDBA alone, whereas there was almost no peak shift in the case of NaPDBA-βCD (Figure 3-13). Therefore, NaPDBA and βCD do indeed form an inclusion complex, and the inter-chromophore interaction is weaker than in the case of NaPDBA alone, especially at low temperatures.

On the other hand, the addition of γCD did not change the absorption spectrum of NaPDBA at room temperature with an absorption peak at 604 nm (Figure 3-13). Interestingly,

the absorption peak of NaPDBA was further red-shifted to 612 nm and broadened by cooling to 143 K after allowing inclusion to fully progress by standing at 243 K in the presence of γCD Figure. 3-8B, 3-13). This suggests that the inter-pentacene excitonic interaction was enhanced by the formation of inclusion complex between NaPDBA and γCD at low temperatures.

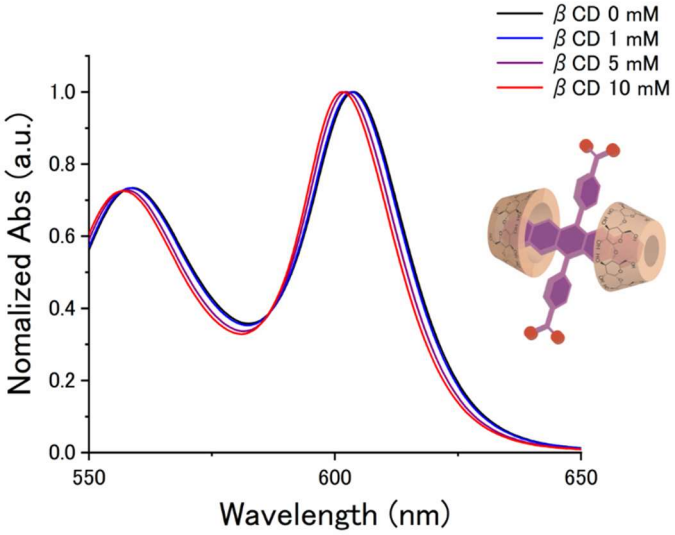

Figure 3-14. Absorption spectra of NaPDBA with different concentrations of βCD in water-glycerol (1:1) at room temperature ([NaPDBA] = 1 mM [βCD] = 0-10 mM).

The complex structures between NaPDBA and βCD/γCD were further studied by NMR measurements. The NMR spectra of NaPDBA and βCD at room temperature in water-glycerol showed a change in the chemical shift of the NaPDBA-derived peak (Figure 3-15A, B). Job plot by measuring the NMR spectra of NaPDBA and βCD at different concentrations suggested that the molar ratio of NaPDBA to βCD is 1:2 in their inclusion complex (Figure 3-15C). This result indicates that the two βCD molecules encapsulate one NaPDBA molecule.

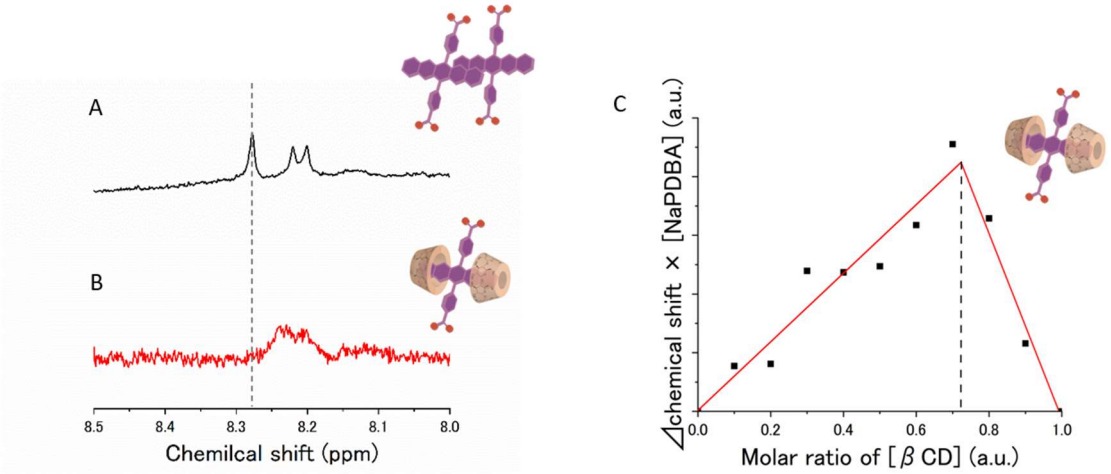

Figure 3-15. ^{1}H NMR spectra of (A) NaPDBA ([NaPDBA] = 2 mM) and (B) NaPDBA and βCD ([NaPDBA] = 0.6 mM, [βCD] = 1.4 mM) in D_2O-glycerol-d_8 (1:1) at room temperature. Sodium 3-(Trimethylsilyl)-1-propanesulfonate was used as internal standard. (C) Job plot of NaPDBA and βCD in D_2O-glycerol-d_8 (1:1). The total concentration of NaPDBA and βCD was kept as 2 mM. The shift of the peak at around 8.28 ppm is shown.

Due to the technical difficulty of obtaining NMR spectra with enough signal-to-noise ratio in viscous water-glycerol at low temperatures, we instead evaluated the complexation of NaPDBA with γCD in water at room temperature. The absorption spectrum of NaPDBA with γCD in water at room temperature showed a similar red-shift and broadening compared with that in water-glycerol at 143 K, and their peak positions were almost identical, indicating the formation of the similar inclusion complex (Figure 3-16).

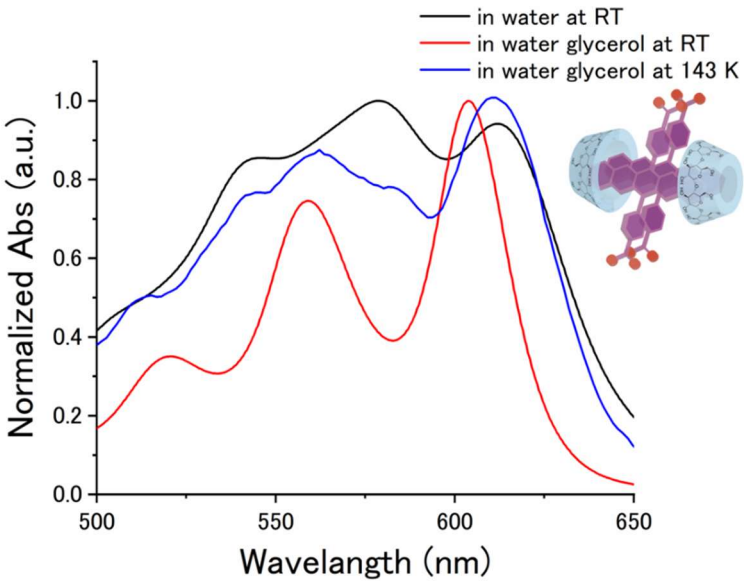

Figure 3-16. Absorption spectra of NaPDBA and γCD in water at room temperature (black line), in water-glycerol (1:1) at room temperature (red line), and in water-glycerol (1:1) at 143 K (blue line) ([NaPDBA] = 1 mM, [γCD] = 5 mM).

Nuclear Overhauser effect spectroscopy (NOESY) NMR measurements of NaPDBA and γCD in water at room temperature revealed that there are cross peaks between the protons inside the CD ring and the pentacene skeleton of NaPDBA (Figure 3-17).

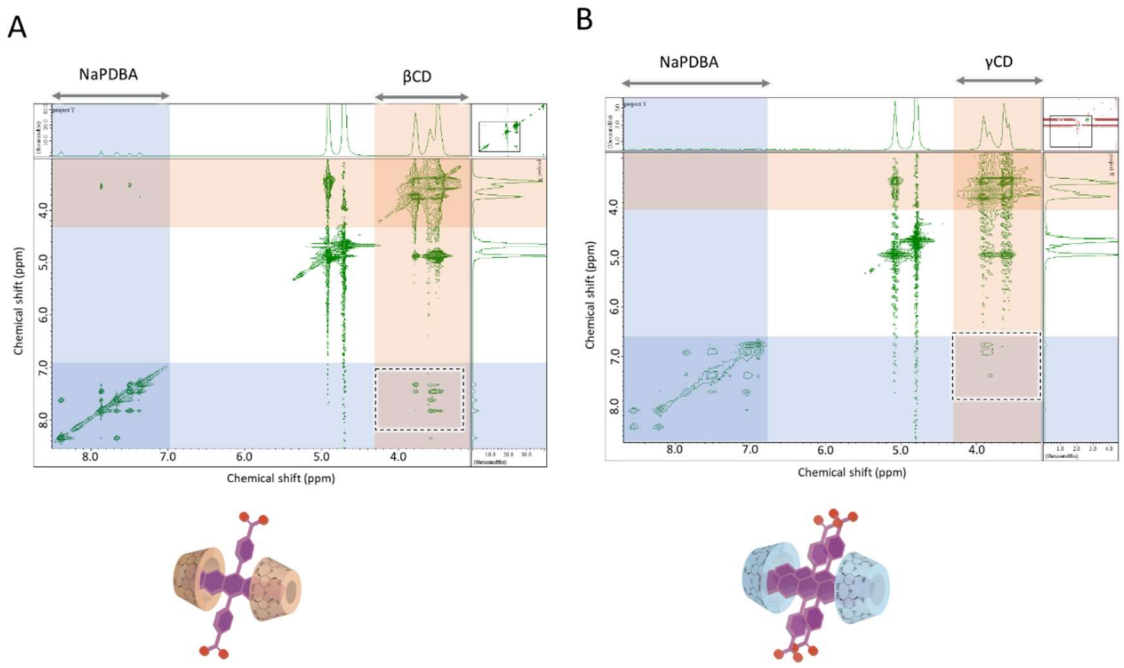

Figure 3-17. ^{1}H NOESY spectra of (A) NaPDBA and βCD ([NaPDBA] = 1 mM, [βCD] = 5 mM) and (B) NaPDBA and γCD ([NaPDBA] = 1 mM, [γCD] = 5 mM) in D_2O at room temperature. Sodium 3-(Trimethylsilyl)-1-propanesulfonate was used as internal standard.

This result indicates that the pentacene moiety of NaPDBA is incorporated into the internal space of γCD by hydrophobic interaction. Diffusion ordered spectroscopy (DOSY) measurements indicate that the mixing of NaPDBA and γCD reduced their diffusion coefficients to similar values, which supports the complexation of NaPDBA and γCD (Figure 3-18).

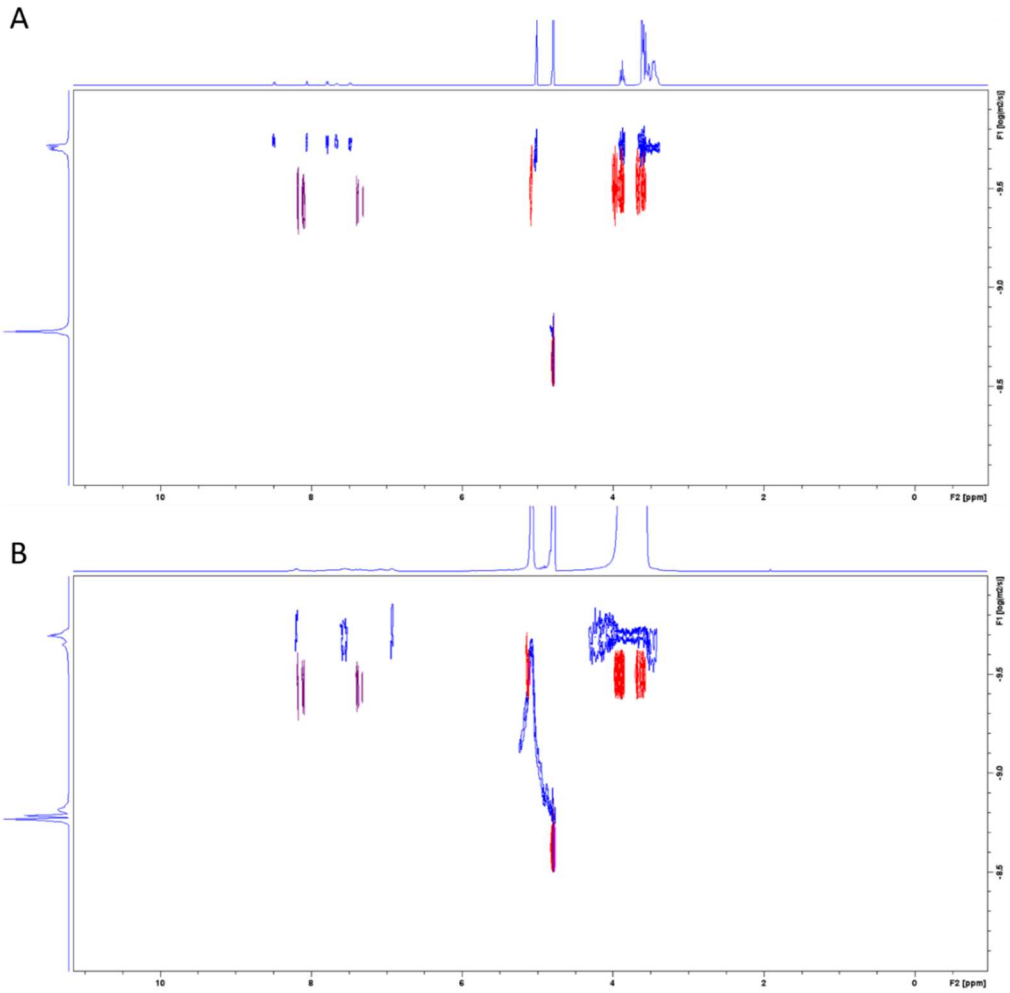

Figure 3-18. DOSY spectra of NaPDBA , CD and these mixture. (A) DOSY spectra of [NaPDBA] = 1 mM (purple), [βCD] = 2 mM (red) and a mixture of [NaPDBA] = 1 mM and [βCD] = 2 mM (blue) in D_2O at room temperature. Residual water was used as internal standard. (B) DOSY spectra of [NaPDBA] = 1 mM (purple), [γCD] = 2 mM (red) and a mixture of [NaPDBA] = 1 mM and [γCD] = 2 mM (blue) in D2O at room temperature. Residual water was used as internal standard.

Deuterated water was used as the solvent because the viscosity of the water-glycerol mixture was too high for reliable DOSY measurements. γCD-derived NMR peaks were observed around 3.5-5.0 ppm and NaPDBA-derived NMR peaks around 7.5-8.5 ppm, both showing a decrease in diffusion coefficient by the mixing of γCD and NaPDBA. The diffusion coefficient of NaPDBA decreased from 2.7×10^{-10} m^2 s^{-1} to 1.6×10^{-10} m^2 s^{-1} and that of γCD decreased from 2.2×10^{-10} m^2 s^{-1} to 2.0×10^{-10} m^2 s^{-1} upon mixing. Importantly, the diffusion coefficients of NaPDBA and γCD were almost the same after mixing, which supports that NaPDBA and γCD form a complex. Similarly, the mixing of NaPDBA and βCD resulted in the decrease of the diffusion coefficients of NaPDBA and βCD from 2.7×10^{-10} m^2 s^{-1} to 1.8×10^{-10} m^2 s^{-1} and from 2.3×10^{-10} m^2 s^{-1} to 2.0×10^{-10} m^2 s^{-1}, respectively, confirming the formation of the NaPDBA-βCD complex.

Job plot by using NMR spectra of NaPDBA and γCD in water showed that the molar ratio of NaPDBA to γCD is 1:1 (2:2) (Figure 3-19). This result suggests that two molecules of γCD encapsulate a NaPDBA dimer, which is reasonable since the inner diameter of γCD is larger than that of βCD, and strong excitonic interaction between pentacene moieties was observed in the NaPDBA-γCD inclusion complex.

The hydrophobic accommodation of NaPDBA by βCD in water at room temperature was also observed by NOESY and DOSY measurements (Figure 3-17,18). The job plot in water suggested the same 1:2 molar ratio inclusion complex of NaPDBA and βCD, similar to the case in water-glycerol (Figure 3-19).

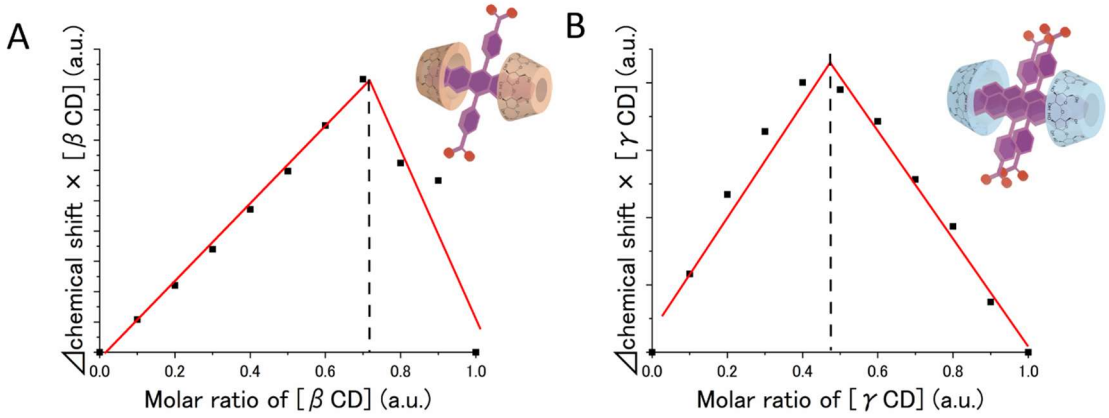

Figure 3-19. (A) Job plot of NaPDBA and βCD in D_2O. The total concentration of NaPDBA and βCD was kept as 2 mM. The shift of the peak at around 3.78 ppm is shown. (B) Job plot of NaPDBA and γCD in D_2O. The total concentration of NaPDBA and γCD was kept as 1 mM. The shift of the peak at around 3.93 ppm is shown. Sodium 3-(Trimethylsilyl)-1-propanesulfonate was used as internal standard.

Absorption spectra showed that the NaPDBA-βCD inclusion complex were molecularly dispersed in water (Figure 3-20), suggesting that and the NaPDBA-βCD complex aggregated in water-glycerol due to the reduced solubility of βCD.

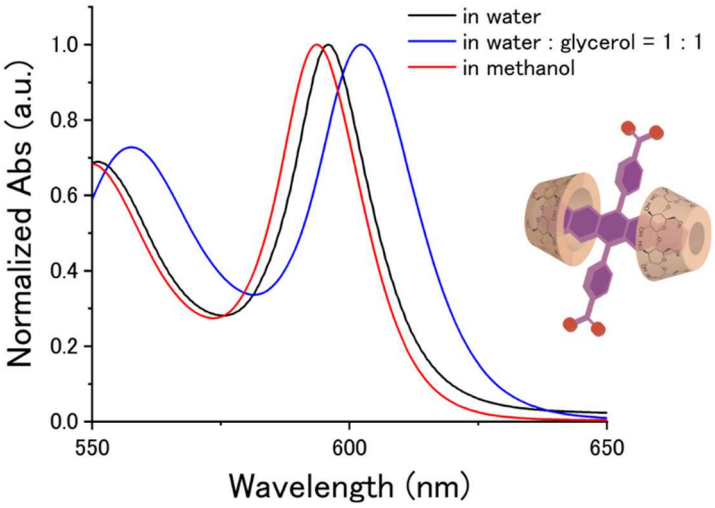

Figure 3-20. Absorption spectra of NaPDBA and βCD in water (black), in water-glycerol (1:1) (blue) and only NaPDBA in methanol (red) at room temperature ([NaPDBA] = 1 mM, [βCD] = 5 mM).

In the MD simulation, the 2:2 inclusion complex of NaPDBA-γCD was stable in water-glycerol at 243 K (Figure 3-21A,B).

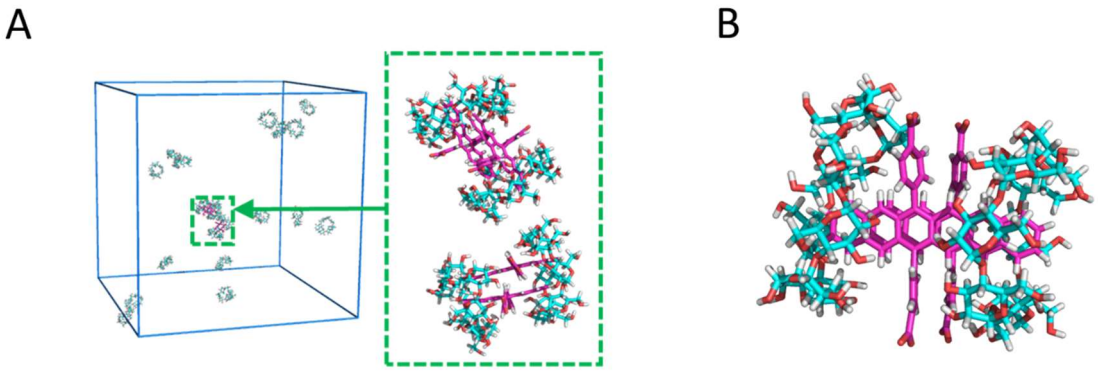

Figure 3-21. MD simulation of the supramolecular assemblies. (C,D) MD simulation snapshots of NaPDBA and γCD ([NaPDBA] = 1 mM, [γCD] = 5 mM) in water-glycerol (1:1) at 243 K.

The MD simulation results showed that both d_{COM} and θ fluctuate less in NaPDBA-γCD than in NaPDBA alone, which is reasonable since NaPDBA dimers are encapsulated in γCD (Figure 3-10). In NaPDBA-γCD, the pentacene units associate at a closer distance, causing orbital overlap between the two chromophores. In the presence of orbital overlaps, we cannot simply classify J- or H- aggregate assuming point-dipole approximation; the excitonic coupling depends sensitively on the relative geometry between the chromophores and molecular orbitals. It has been reported that a few Å displacements affect the sign of the inter-chromophore interaction, demonstrating both J-aggregate-like and H-aggregate-like spectral changes at face-to-face geometry [49]. According to our MD simulation, the shift along the long-axis of the pentacene backbones varies by a few Å. This variation would result in the simultaneous presence of J-aggregate-like and H-aggregate-like dimers in the system, resulting in the broad absorption spectra of NaPDBA-γCD. Note that the inclusion complexes of NaPDBA-γCD were unstable at room temperature in water-glycerol (Figure 3-22), which is consistent with the experimental results for complexation only by cooling (Figure 3-13).

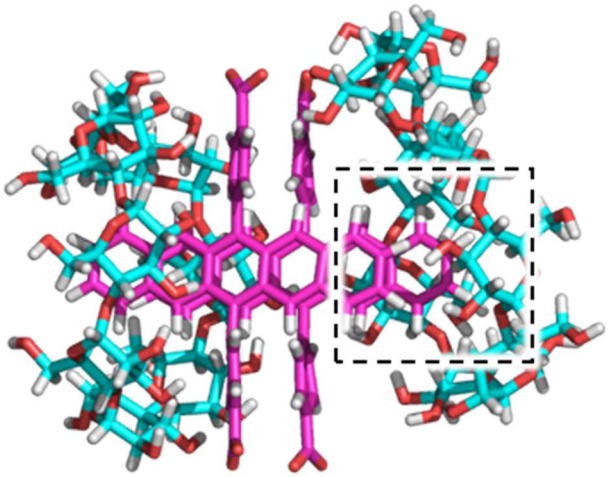

Figure 3-22. MD simulation snapshots of NaPDBA and γCD ([NaPDBA] = 1 mM, [γCD] = 5 mM) in water-glycerol (1:1) at 300 K. The dotted area shows that NaPDBA and γCD are about to be detached.

In the MD simulation, the 1:2 inclusion complex of NaPDBA-βCD was found to be stable in water-glycerol at room temperature (Figure 3-23). When the simulation was started from the initial aggregated structure of the inclusion complexes, no dispersion behavior was observed, supporting that the excitonic interaction between pentacenes observed in the absorption spectra is caused by the aggregation of the inclusion complexes.

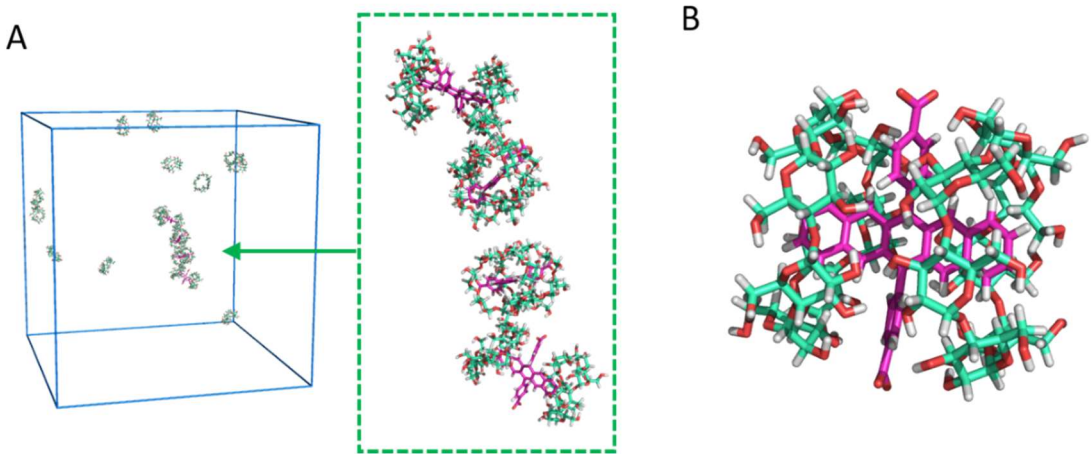

Figure 3-23. MD simulation snapshots of NaPDBA and βCD ([NaPDBA] = 1 mM, [βCD] = 5 mM) in water-glycerol (1:1) at 300 K.

The PMFs for pulling away one γCD molecule of the 2:2 inclusion complex of NaPDBA-γCD in water-glycerol until it unfolded the NaPDBA dimer were 7.9 ± 2.1 and 21.1 ± 2.4 kJ/mol. Since the thermal energy of the complex consisting of 4 molecules at 300 K can be estimated about 10 kJ/mol, the complex of NaPDBA-γCD in water-glycerol at 300 K should not be energetically stable. It indicates that some NaPDBA molecules might be dispersed in the system without forming the complex.

Both 1:2 inclusion complex of NaPDBA-βCD and 1:1 complex of NaPDBA-γCD were found to be stable and dispersed in water at room temperature in the MD simulations (Figure 3-24).

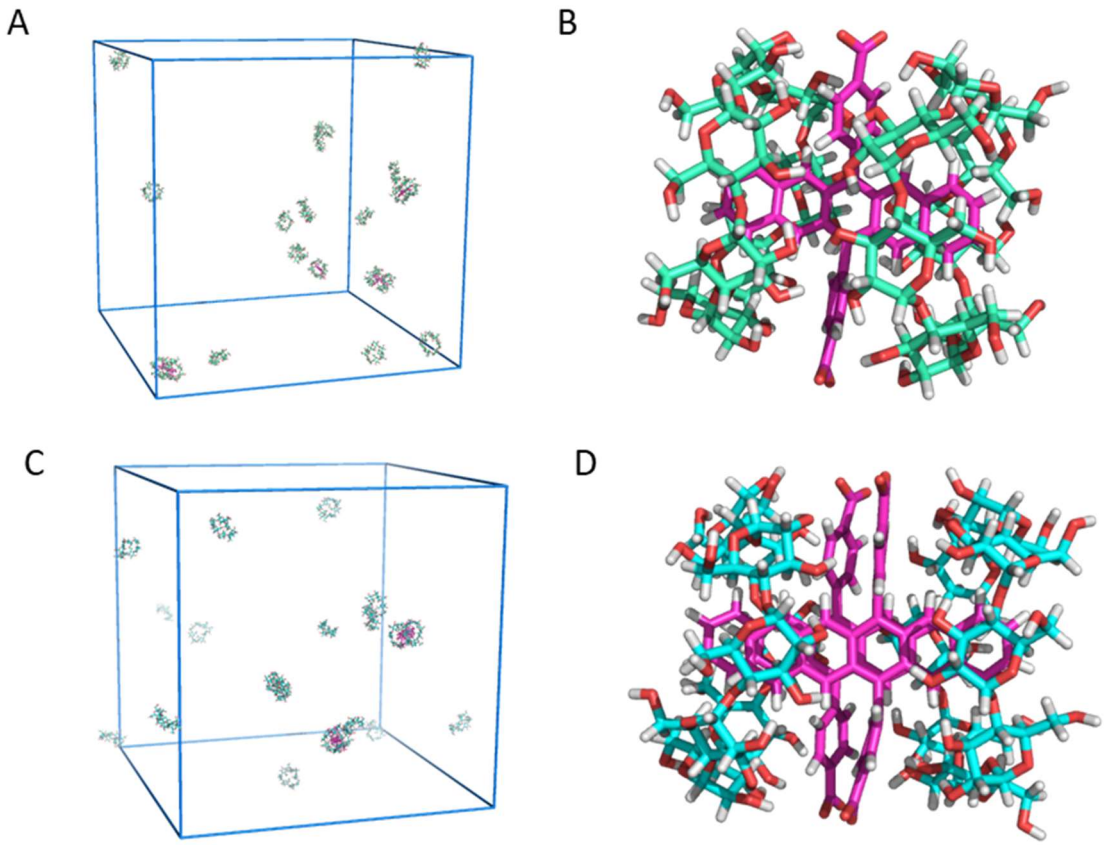

Figure 3-24. (A, B) MD simulation snapshots of NaPDBA and βCD ([NaPDBA] = 1 mM, [βCD] = 5 mM) in water at 300 K. (C, D) MD simulation snapshots of NaPDBA and γCD ([NaPDBA] = 1 mM, [γCD] = 5 mM) in water at 300 K.

The analysis of the potential of mean force (PMF) of the complexes also supported this stability difference quantitatively: the higher the PMF value of the complex, the more stable the complex. The PMFs for pulling away one γCD molecule of the 2:2 inclusion complex of NaPDBA-γCD in water-glycerol until it unfolded the NaPDBA dimer were 7.9 ± 2.1 and 21.1 ± 2.4 kJ/mol at 300 K and 243 K, respectively (Figure 3-25).

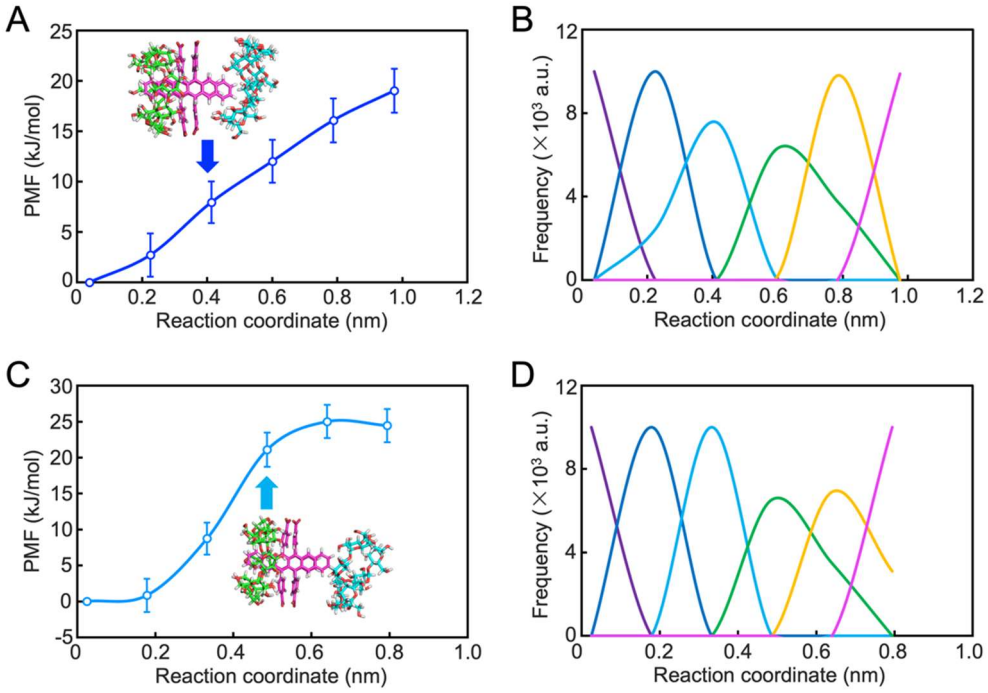

Figure 3-25. PMF profiles of 2:2 inclusion complex of NaPDBA-γCD in water-glycerol at 300 K (A) and at 243 K (C). Each inset snapshot illustrates the top view of the NaPDBA-γCD complex at the moment of its collapse. Apparent probability density of 2:2 inclusion complex of NaPDBA-γCD in water-glycerol at 300 K (B) and at 243 K (D). The curves drawn in different colors were calculated from each US simulation. The error bars depict only the statistical uncertainty from the connection of probability density by WHAM.

Therefore, it shows that the NaPDBA-γCD inclusion complex at 243 K was more stable than that at 300 K. Since the thermal energy of the complex consisting of 4 molecules at 300 K can be estimated about 10 kJ/mol, the complex of NaPDBA-γCD in water-glycerol at 300 K should not be energetically stable. The inclusion of the NaPDBA monomer by two βCD molecules was suggested by the absorption spectra, NMR measurements, and MD simulations (Figure 3-13-25). This 1:2 inclusion complex of NaPDBA-βCD without SF was used for comparison.

・3-3-2 Evidence of SF

To investigate the SF properties of these systems, we conducted femtosecond and nanosecond pump-probe TAS (fs- and ns-TAS) measurements in water-glycerol glass at 143 K, which is relevant to ESR and DNP measurements. Prior to the TAS measurements, the water-glycerol solutions of NaPDBA and NaPDBA-βCD were quenched and vitrified in liquid nitrogen after complexation at 243 K. The excitation wavelength was set at the lowest absorption edge (600-635 nm) to minimize the excess photoexcitation energy. Figure 3 shows a thorough comparison of fs-TAS measurements of the systems and the corresponding results of global analyses. The bare NaPDBA aggregates showed broad transient absorption with a peak at 430-450 nm just after photoexcitation (Figure 3-26A-C, Figure 3-27), which can be assigned to the transition from the S_1 excited state (S_1-S_n transition). For pentacene-based systems, the presence of SF can be estimated from the ultrafast growth of transient absorption around 510-520 nm typically assigned to the T_1-T_n transition of a pentacene skeleton [8]. As the peak around 450-460 nm decreased in several picoseconds, the TA around 510-520 nm became dominant. This allowed us to confirm the ultrafast generation of T_1 through SF of NaPDBA aggregates. To quantify the ultrafast SF process, we globally analyzed the observed fs-TAS assuming a sequential model with two components (Figure 3-26C-E).

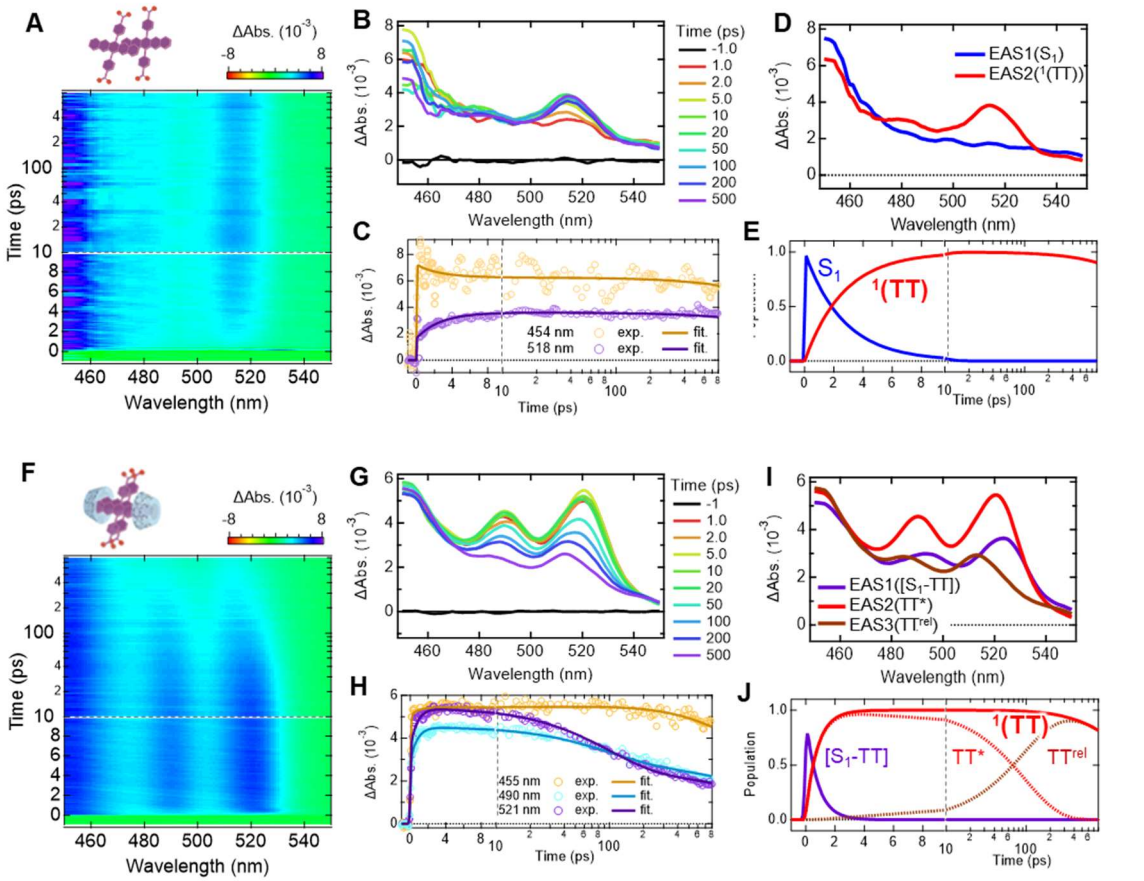

Figure 3-26. fs-TAS measurements of the supramolecular assemblies. Overview of fs-TAS analysis of (A-E) NaPDBA and (F-J) NaPDBA-γCD in water-glycerol (1:1) at 143 K ([NaPDBA] = 1 mM, [γCD] = 5 mM). (A, F) Pseudo-2D plots of experimentally observed fs-TAS (excitation: 635 nm for NaPDBA and 600 nm for NaPDBA-γCD), (B, G) spectral evolution of the TAS, and (C, H) temporal change of transient absorption at selected wavelengths and fitting curves from global analysis. (D, I) Evolution-associated spectra and (E, J) corresponding concentration kinetics obtained from global analysis based on sequential models.

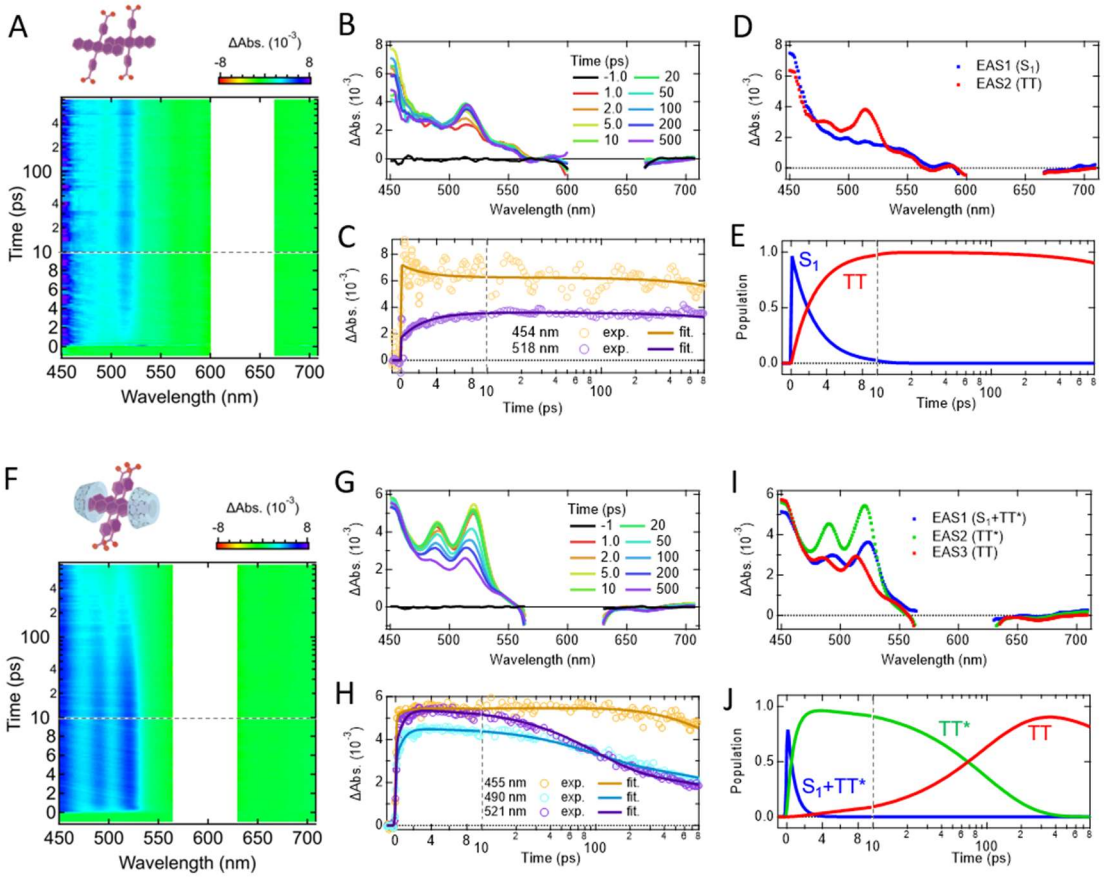

Figure 3-27. fs-TAS measurements of the supramolecular assemblies. (This figure displays the entire wavelength range of Fig. 3) Overview of fs-TAS analysis of (A-E) NaPDBA and (F-J) NaPDBA-γCD in water-glycerol (1:1) at 143 K ([NaPDBA] = 1 mM, [γCD] = 5 mM). (A, F) Pseudo-2D plots of experimentally observed fs-TAS (excitation: 635 nm for NaPDBA and 600 nm for NaPDBA-γCD), (B, G) spectral evolution of the TAS, and (C, H) temporal change of transient absorption at selected wavelengths and fitting curves from global analysis. (D, I) Evolution-associated spectra and (E, J) corresponding concentration kinetics obtained from global analysis based on sequential models.

The first component was converted to the second component with a time constant of 2.65±0.01 ps, followed by negligible decay (> 1 ns) in the current time window. Note that the first and second components of the evolution-associated spectra (EAS) can reasonably be assigned from their shapes to the spectra from S_1 and T_1, respectively. Because the transition timescale is much quicker than that of typical ISC, we concluded that the transition of the first step of SF, $S_1 \rightarrow {}^1(TT)$, in the NaPDBA aggregates occurs with a time constant of 2.65 ps.

We also observed an increase in T_1-T_n absorption for ~7 ns in ns-TAS, which was assigned to the ISC of monomolecularly dispersed NaPDBA (Figure 3-28). This implies that the system consisted of a mixture of monomeric and dimeric NaPDBA, consistent with the MD simulation.

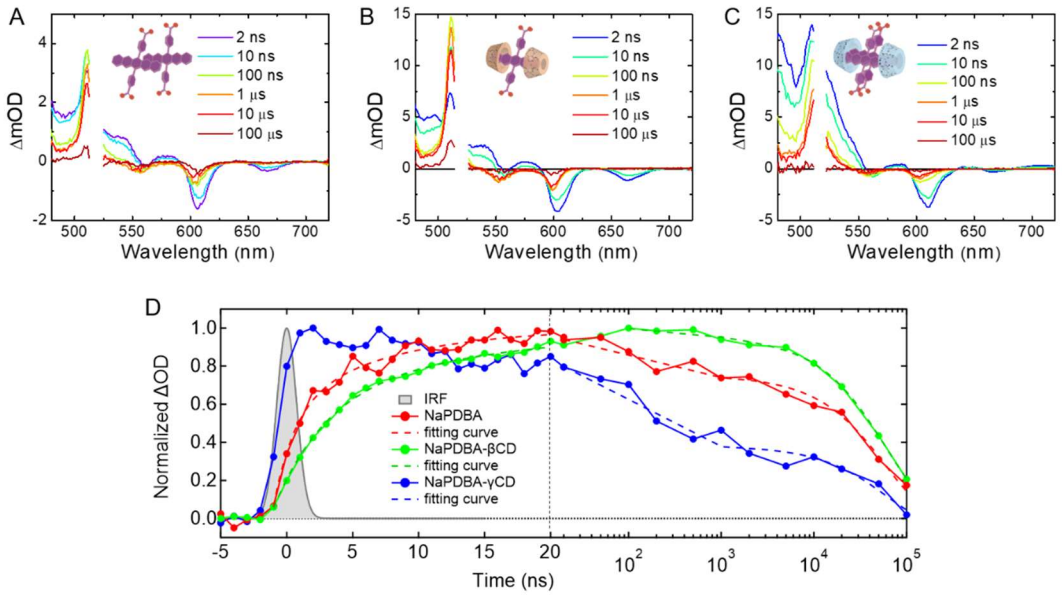

Figure 3-28. Overview of ns-TAS spectral evolution of (A) NaPDBA, (B) NaPDBA-βCD, and (C) NaPDBA-γCD (excitation: 520 nm). (D)Kinetic traces of the transient absorption at 510 nm from -10 ns to 20 μs. The time constants of the rise components of T_1-T_n absorption observed at 510 nm were 3.4±1.9 and 23±2.4 ns for NaPDBA, 5.6±0.6 and 38±5.0 ns for NaPDBA-βCD, 2.6±1.7 ns for NaPDBA-γCD. The time constants of the decay components of T_1-T_n absorption observed at 510 nm were 0.081±0.062, 2.4±3.4 and 73±2.8 μs for NaPDBA, 0.585±0.558 and 58±3.7 μs for NaPDBA-βCD, 0.010±0.007, 0.222±0.082 and 62±26 μs for NaPDBA-γCD. We confirmed that the population lifetimes were long enough to expect DNP.

For the NaPDBA-γCD complex, the TAS around 510-520 nm emerged rapidly after photoexcitation concurrently with the broad absorption around 450-500 nm (Figure 3-26F-H). This indicated prompt generation of the excited states containing ^{1}(TT) states character owing to the stronger electronic coupling between the chromophores. The spectral shape of the initial TA was also different from that observed for the bare NaPDBA aggregates. Note that a significant red-shift of the TA peaks in the ps-time range was also observed, which cannot be explained by simply assuming the inhomogeneous broadening owing to different conformers of the NaPDBA-γCD complex. These observations can be explained by the model of either (1) initial generation of the S_1-TT mixed adiabatic electronic states as suggested in

the chromophores with strong electronic interaction [50, 51], or (2) simultaneous detection of coherent and incoherent SF [52], which could result from the dynamic fluctuation and inhomogeneity of the system.

Figure 3-26H-J show the results of the global fitting of the TAS assuming a three-component sequential model. Although the third EAS resembles the spectrum of ^{1}(TT) observed in the bare NaPDBA aggregates, the first and second EAS components show different spectral shapes from the EAS in the bare NaPDBA aggregates. Given that the complexation with γCD results in the tightly packed dimer, we conclude as follows. Initial transient absorption spectrum (EAS1) contains spectroscopic characters of both S_1 and TT state because of strong electronic coupling between the adjacent pentacene moieties leading to the mixed adiabatic state of S_1 and ^{1}(TT) or rapid SF within the time resolution of our system (~ 100 fs). Note that we denote the initial component as "[S_1-TT]" to emphasize the indistinguishably mixed character of the state indicated by the spectral shape. Consequently, the transition to the hot ^{1}(TT) state ([S_1-TT] → TT*) occurs in 0.79±0.01 ps via SF. Because the timescale is likely quicker than the reorganization of the relative geometry of the paired chromophores (e.g., excimer formation), further spectral change with a time constant of 96±1 ps occurs (denoted as TT*→TT^{rel} in Fig. 3I,J). To distinguish the whole mechanisms of the SF in the NaPDBA-γCD system, more sophisticated spectroscopy, such as coherent two-dimensional electronic spectroscopy, will be needed [53], which is beyond our focus in this manuscript. Here we emphasize that the TAS successfully confirmed the generation of ^{1}(TT) accelerated by more than a factor of three compared to the bare NaPDBA system.

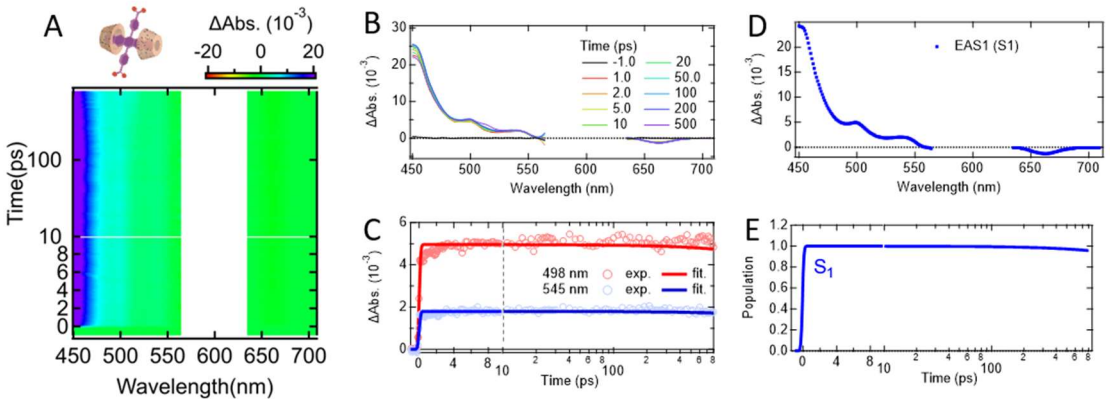

Figure 3-29. Overview of fs-TAS analysis of NaPDBA-βCD in water-glycerol (1:1) at 143 K ([NaPDBA] = 1 mM, [βCD] = 5 mM). (A) Pseudo-2D plots of experimentally observed fs-TAS (excitation: 600 nm), (B) spectral evolution of the TAS, and (C) temporal change of transient absorption at selected wavelength and fitting curve resulted from global analysis. (D) Evolution associated spectra and (E) corresponding concentration kinetics obtained from global analysis with one transient.

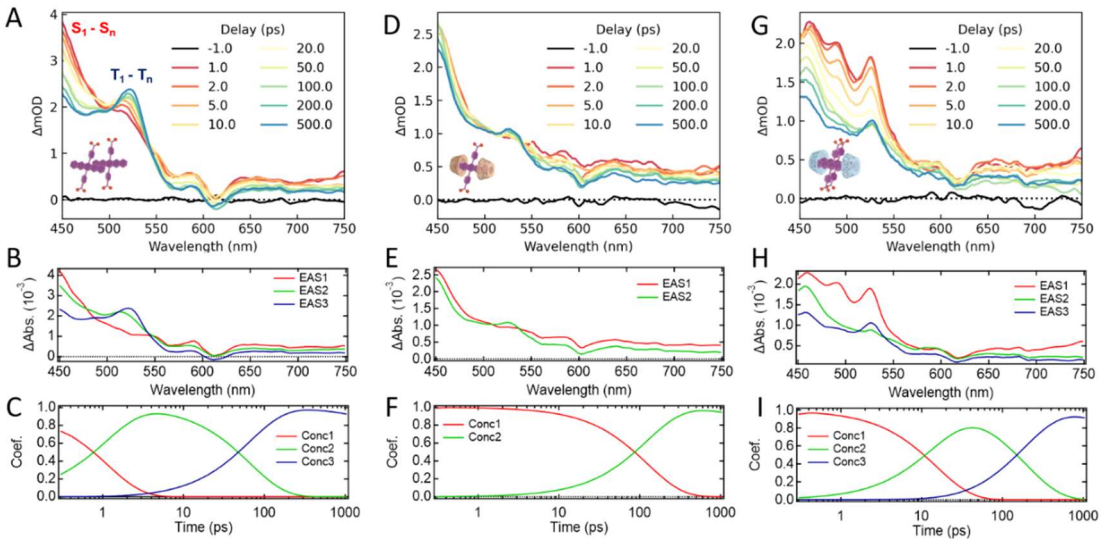

Figure 3-30. Overview of fs-TAS analysis of (A-C) NaPDBA water solution at room temperature, (D-F) NaPDBA water solution with βCD, and (G-H) NaPDBA water solution with γCD. (A, D, G) Experimentally observed fs-TAS (excitation: 400 nm). (B, E, H) Evolution associated spectra and (C, F, I) respective concentration kinetics obtained from target analysis based on sequential models. While NaPDBA water solution and one with γCD showed distinct T_1-T_n transition at 520 nm observed in a few picoseconds owing to SF, one with βCD showed negligible SF indicated by the almost S_1-like spectral feature of EAS2.

In stark contrast, negligible SF was observed in the βCD complex (Figure 3-29), consistent with the monomolecularly dispersed picture in which the inter-chromophore interactions are significantly weakened by the complexation of a single NaPDBA molecule with two βCD molecules (Figure 3-23). We also observed the behavior in NaPDBA systems in water at room temperature (Figure 3-30), confirming that the dynamics is caused by complexation with cyclodextrins.

Overall, we concluded that sub-ns T_1 generation due to SF occurs in the bare NaPDBA dimers and NaPDBA-γCD complex, while the NaPDBA-βCD complex does not show significant SF. Note that ns-TAS measurements of the NaPDBA and NaPDBA-βCD systems also showed slower T_1 generation due to ISC from S_1 to T_1 (Figure 3-28. Additionally, fs-TAS and ns-TAS showed subtle excitation wavelength dependences (details are in Figure 3-31). This suggested that both aggregated and isolated NaPDBA coexisted in the water-glycerol glass systems, and both SF-derived and ISC-derived triplets were generated with light irradiation. It would be possible to selectively make dimers or multimers by introducing functional groups to further control inter-chromophore interactions or by covalently connecting chromophore units.

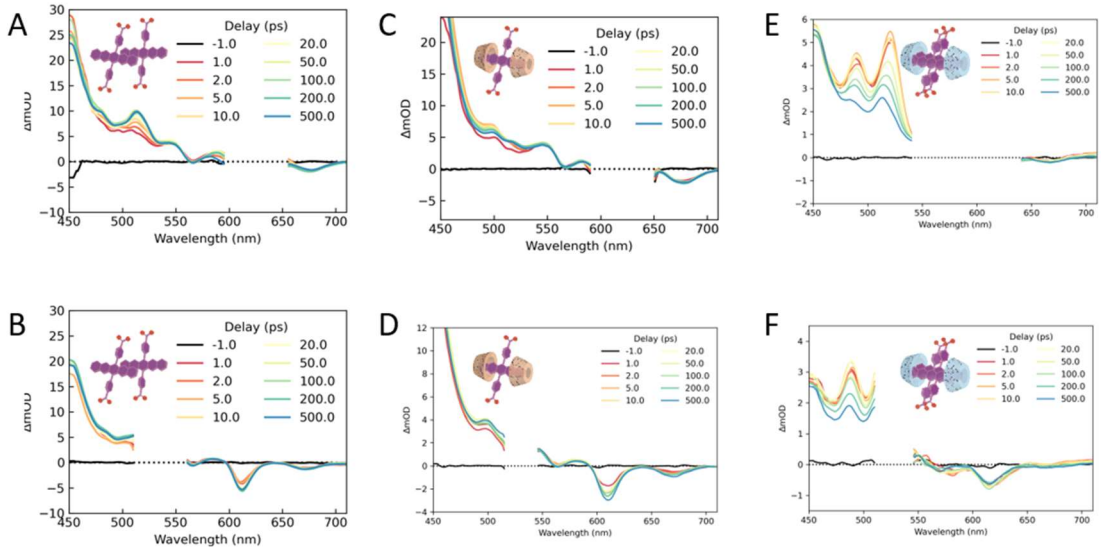

Figure 3-31. Excitation wavelength dependence of fs-TAS. Low-temperature fsTAS (143 K) analysis of the NaPDBA water-glycerol solution. ([NaPDBA] = 1 mM). (A, B) fs-TAS of NaPDBA solution excited with (A) 620 nm, and (B) 527 nm; (C, D) fs TAS of NaPDBA-βCD excited with (C) 625 nm, and (D) 527 nm; (E, F) fs-TAS of NaPDBA-γCD excited with (E) 600 nm, and (F) 527 nm. Because of strong scattering from pump pulses, TA data around the pump wavelength were not available.

・3-3-3 Generation of quintet multiexcitons

Having concrete evidence of SF, we performed time-resolved ESR measurements to evaluate the transient electron spin polarization of these supramolecular assemblies in water-glycerol glass. The samples were prepared in the same way as for the TAS measurements, except that glass capillaries were used. As expected from the SF found in the NaPDBA-only assemblies and the NaPDBA-γCD complex, a signal derived from the quintet was observed at a position where the peak width was about one-third that of the triplet (Figure 3-32) [9, 13-16].

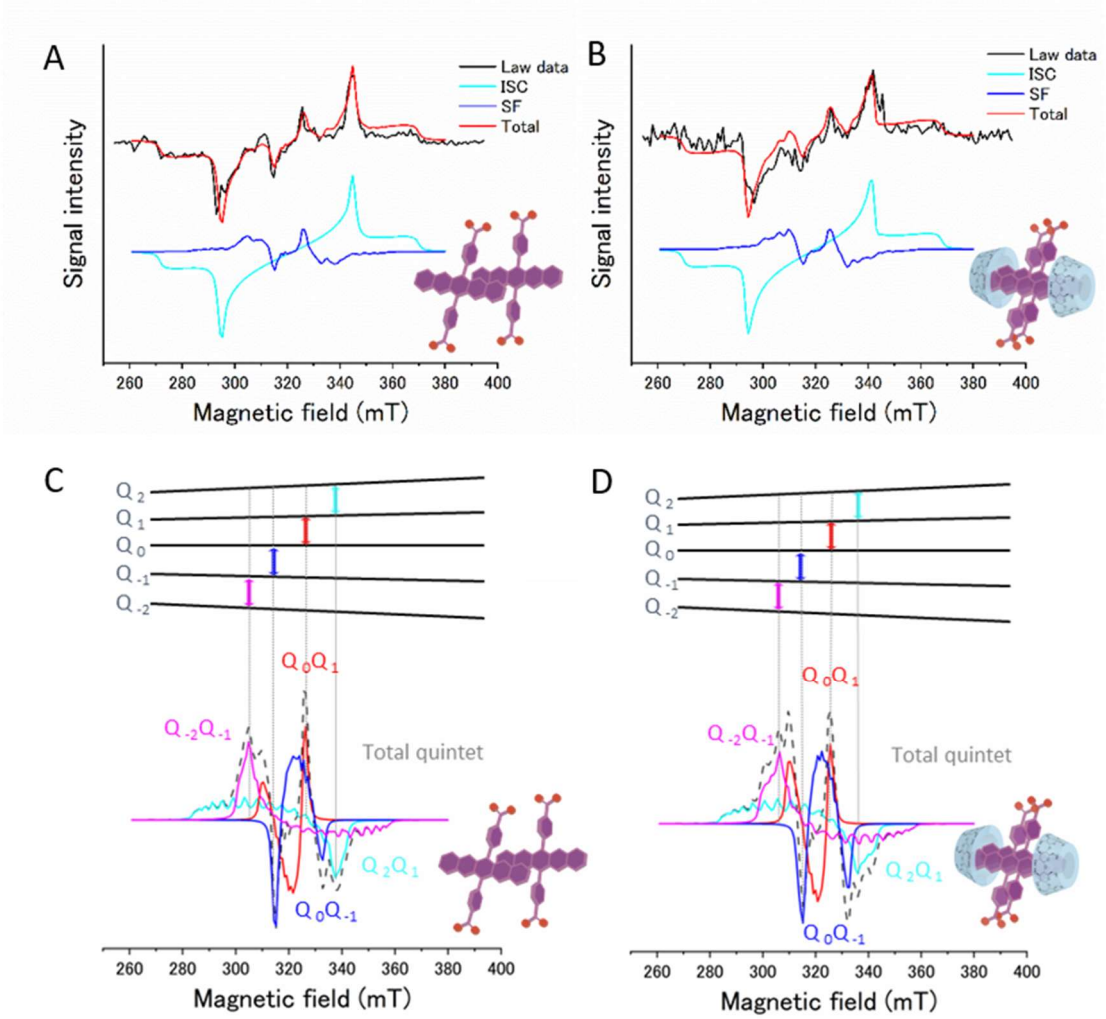

Figure 3-32. Time-resolved ESR measurements of the supramolecular assemblies. Time-resolved ESR spectra of (A) NaPDBA and (B) NaPDBA-γCD in water-glycerol (1:1) at 143 K ([NaPDBA] = 1 mM, [γCD] = 5 mM) just after photoexcitation at 527 nm and simulated spectra of (C) NaPDBA and (D) for NaPDBA-γCD, attributing transitions between each energy level of the quintet in the ESR spectra. The fitting parameters of the ISC-born triplet and SF-born quintet are summarized in Tables 3-1 and 3-2, respectively.

These ESR spectra could be fitted as a quintet-triplet superposition. The spectra were simulated using a geometric fluctuation model of the quintet multiexcitions between two strongly coupled TT conformations (TT_A and TT_B) with similar orientations with different *J*-couplings following previous reports [16, 54] We assumed the conformations of the TT_A and TT_B states to be parallel and slightly off parallel, respectively, for the vibronic effect of the *J*-coupling in the dimers. Interestingly, the pentacene moieties were found to be oriented parallel to each other to form the ^{5}(TT) dimer, which agrees well with the MD simulations. The fitting parameters are summarized in Tables S1 and S2. The $|^5(TT)_2\rangle$, $|^5(TT)_0\rangle$, and $|^5(TT)_{-2}\rangle$ sublevels were found to be preferentially populated with the states S_1 and ^{1}(TT) in both systems. The largest ESR signal was observed when the magnetic field (B_0) is parallel to the pentacene backbone (Figure 3-33).

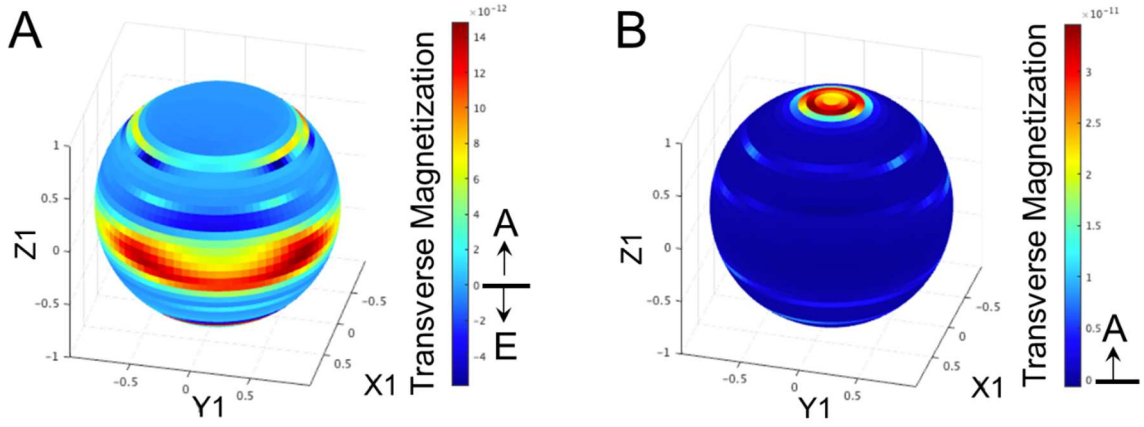

Figure 3-33. (A) Mapping of the transverse magnetization at the field strength of "X, Y" in Fig. S22A from the spin polarized ESR spectrum of ^{5}TT state. (B) Mapping of the magnetizations for the field strength of "Z" in Figure 3-34. The mappings of the magnetization were performed from the computations of electron spin polarization[16] for all possible directions of the external magnetic field as reported previously[55, 56].

In this orientation, other states such as $^5(TT)_2$ and $^5(TT)_{-2}$ are also populated, however, ESR transitions involving $^5(TT)_2$ and $^5(TT)_{-2}$ have almost no contribution to this signal. To demonstrate this point, we computed ESR spectrum of ^5TT state obtained by the powder pattern calculation with considering the spin populations in all the sublevels $^5(TT)_{+2}$, $^5(TT)_{+1}$, $^5(TT)_0$, $^5(TT)_{-1}$ and $^5(TT)_{-2}$ (Figure 3-34A) and the powder pattern with only by $^5(TT)_0 \rightarrow {}^5(TT)_{+1}$ and by $^5(TT)_0 \rightarrow {}^5(TT)_{-1}$ contributions (Figure 3-34B). At the field strengths represented by "Z" and "X, Y" in Fig. Figure 3-34A, the ESR transition intensities (transverse magnetizations) by the quintet states are dominated by the resonances from the $^5(TT)_0$ sublevels. The ESR transitions of $^5(TT)_0 \rightarrow {}^5(TT)_{+1,-1}$ occur at the outer magnetic field strengths when the B_0 is perpendicular to the aromatic planes from the electron spin polarization imaging [56] in Figure 3-33B. On the other hand, the ESR intensity at the field strength at "X, Y" in Figure 3-34A is dominated by the $^5(TT)_0 \rightarrow {}^5(TT)_{+1,-1}$ resonances for B_0 directing to the pentacene backbone (Figure 3-33A). The isolated triplet is produced by the ISC of a single pentacene unit, which also agrees well with the MD simulation and the TAS results.

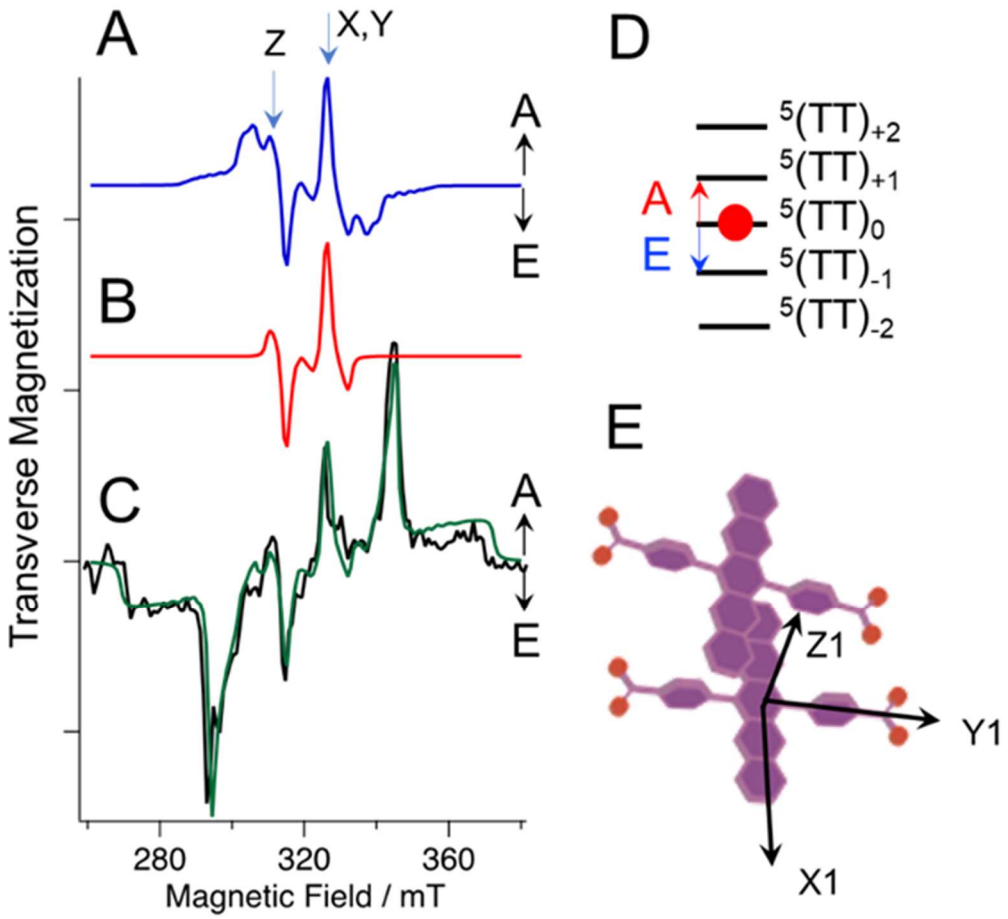

Figure 3-34. (A) Computed ESR spectrum of ^{5}TT state obtained by the powder pattern calculation with considering the computed spin sublevel populations in $^5(TT)_{+2}$, $^5(TT)_{+1}$, $^5(TT)_0$, $^5(TT)_{-1}$ and $^5(TT)_{-2}$ in (D) both of TT_A and TT_B states, by using the reported method[16]. (B) Computed ESR spectrum of ^{5}TT state obtained by the powder pattern calculation only by $^5(TT)_0 \rightarrow {}^5(TT)_{+1}$ and by $^5(TT)_0 \rightarrow {}^5(TT)_{-1}$ contributions in (D). (C) Experimental ESR spectrum of NaPDBA (black line) and simulated ESR spectrum (green line) composed of the blue line in (A) and of the isolated triplet state generated by the ISC. (E) Conformations of the TT_A and TT_B states undergoing the mutual J-modulation between J_A = -5.0 T and J_B = -0.8 T in the TT_A and TT_B, respectively in the exchange-coupling (J). This model is used for the present calculations in the spin sublevel populations and the magnetizations.

On the other hand, even a few microseconds after the generation of ^{5}(TT), no ^{3}(TT)-like ESR signal was observed, and the triplet retained its ISC-derived spectral shape. The ISC-derived triplet and the ^{3}(TT) signal are expected to be observed at similar magnetic field, but the single-exponential decay of the triplet signal suggests that no observable amount of ^{3}(TT) was generated (Figure 3-35).

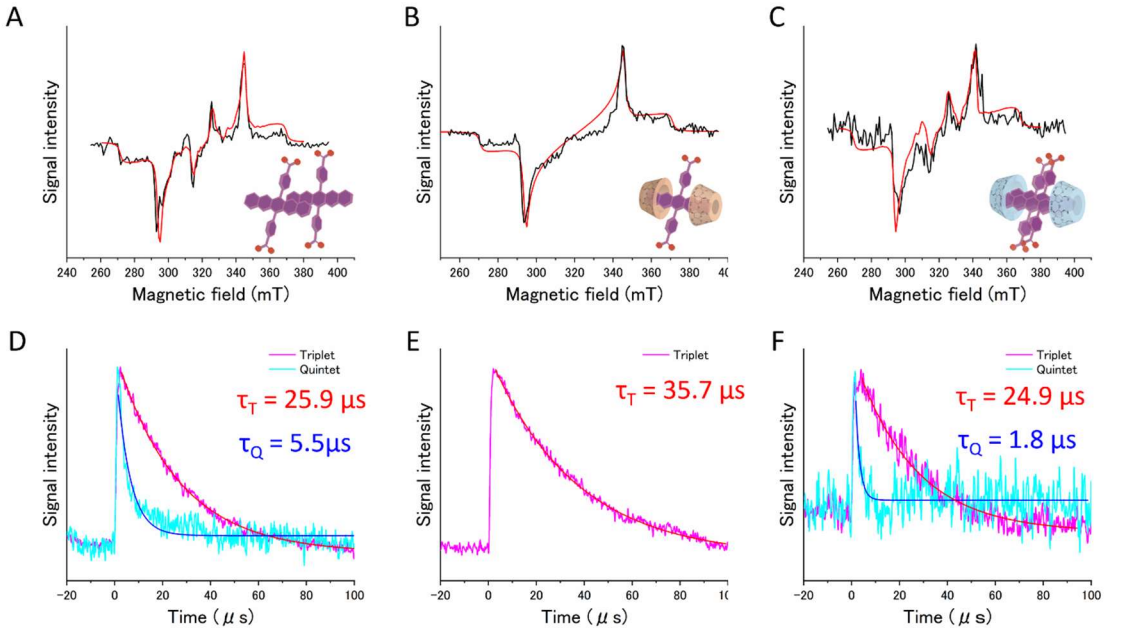

Figure 3-35. Time-resolved ESR spectra (A-C) and decays (D-F) of (A, D) NaPDBA, (B, E) NaPDBA-βCD, and (C, F) NaPDBA-γCD in water-glycerol (1:1) at 143 K ([NaPDBA] = 1 mM, [βCD] = [γCD] = 5 mM) just after photoexcitation at 527 nm. Fitting parameters of simulated spectra (red lines in A-C) for ISC-born triplet and SF-born quintet are summarized in Table 3-1 and 3-2, respectively. The results of single exponential fitting is shown in D-E with corresponding decay times.

The absence of ^{3}(TT) was also supported by the calculated matrix elements of the absolute magnitudes of the spin Hamiltonian based upon the TT geometry (Table 3-4).

	$^5TT_{+2}$	$^5TT_{+1}$	$^5TT_0$	$^5TT_{-1}$	$^5TT_{-2}$	$^3TT_{+1}$	$^3TT_0$	$^3TT_{-1}$	^1TT
$^5TT_{+2}$	3.9231	0.0004	0.0001	0.0000	0.0000	0.0010	0.0007	0.0000	0.0345
$^5TT_{+1}$	0.0004	3.3931	0.0002	0.0001	0.0000	0.0016	0.0007	0.0005	0.0019
$^5TT_0$	0.0001	0.0002	2.8395	0.0002	0.0001	0.0012	0.0000	0.0012	0.0343
$^5TT_{-1}$	0.0000	0.0001	0.0002	2.2637	0.0004	0.0005	0.0007	0.0015	0.0018
$^5TT_{-2}$	0.0000	0.0000	0.0001	0.0004	1.6676	0.0000	0.0007	0.0010	0.0379
$^3TT_{+1}$	0.0010	0.0016	0.0012	0.0005	0.0000	2.2371	0.0003	0.0001	0.0000
$^3TT_0$	0.0007	0.0007	0.0000	0.0007	0.0007	0.0003	2.8485	0.0003	0.0000
$^3TT_{-1}$	0.0000	0.0005	0.0012	0.0015	0.0010	0.0001	0.0003	3.3665	0.0000
^1TT	0.0345	0.0019	0.0343	0.0018	0.0379	0.0000	0.0000	0.0000	5.6349

Table 3-4. Matrix elements of the magnitudes (10^{11} rad/s) of the spin Hamiltonian of [abs($\mathbf{H}_{TTB}$)] calculated for the TT_B state with the B_0 direction of (θ_B, ϕ = (90°, 45°)) of the external magnetic field in the (X1, Y1, Z1) coordinate in Figure R1 in the presence of the exchange coupling of J_B = -0.8 T.

While the interaction between the ^{5}TT and ^{1}TT is large for generating $^5TT_{\pm2}$ and $^5TT_0$ with the coupling values of 3.5×10^9 rad/s, the interactions between ^{3}TT and ^{1}TT is zero. Also, the interactions between ^{5}TT and ^{3}TT minor being ca. 10^8 rad/s. Thus, the generations of the ^{3}TT states are neglected in the present multiexciton. It is thus concluded that the ^{3}TT is not created from the quintet multiexciton in the presence of the strong exchange coupling.

The ESR spectra in Figure 4 did not show the characteristic A/E/A/E spin polarization pattern of the triplet dissociated from $^5(TT)_0$ [57], suggesting that the contribution of the dissociated triplet is almost negligible. This is consistent with the DLS and MD simulation results that NaPDBA forms dimers in water-glycerol and does not form larger aggregates. The polarization lifetime of the quintet of NaPDBA aggregates and the NaPDBA-γCD complex were 5.5 and 1.8 μs, respectively (Figure 3-35D, F), and was determined by the deactivation of the multiexcitons as observed in the ns-TAS (Figure 3-28D). This time constant is sufficient to transfer the polarization to the nuclear spins by microwave irradiation. It is notable that the SF-derived polarization was long enough in the water-glycerol glass, the most important matrix towards the biological applications of DNP. The ESR spectrum of the NaPDBA-βCD complex showed only the ISC-derived triplet signal and no quintet signal (Figure 3-35B).

・3-3-4 DNP using quintet electron spin polarization

DNP was then performed using the polarized electron spins produced in these supramolecular assemblies. The integrated solid effect (ISE) sequence was used for the DNP experiments (see Figure. 3-1B, C, 3-36) [31, 58].

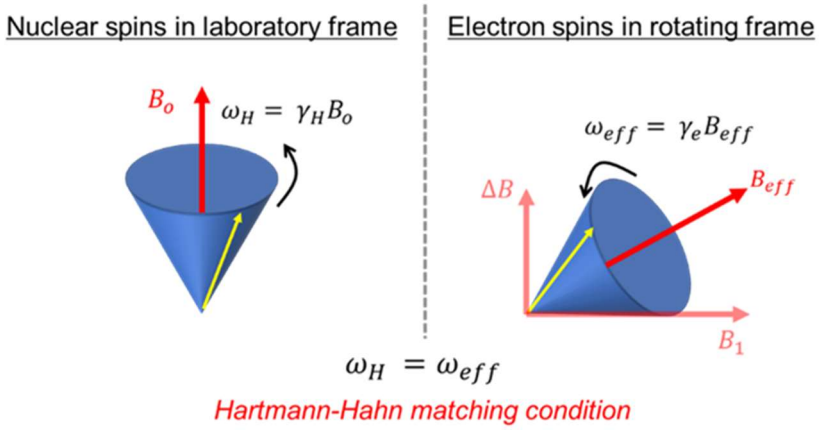

Figure 3-36. Schematic illustration of the Hartmann-Hahn matching condition. The nuclear spins precess with the Larmor frequency ω_H around the external magnetic field B_o in the laboratory frame. The electron spins precess around the effective magnetic field $B_{eff} = \sqrt{{B_1}^2 + \Delta B^2}$ with the frequency $\omega_e = \gamma_e B_{eff}$ in the rotating frame, where B_1 is the power of the irradiated microwave perpendicular to the external magnetic field, ΔB is the offset between ω_{e0} and ω_{MW} ($\Delta B = (\omega_{e0} - \omega_{MW})/\gamma_e$). When the Hartmann–Hahn matching condition $\omega_H = \omega_{eff}$ is satisfied, the polarization transfer occurred most efficiently [31, 58-60].

The sequence starts from laser irradiation to produce the polarized electron spins. Then, microwave and magnetic field sweep are applied simultaneously. By matching the Rabi frequency of electron spins and the Larmor frequency of nuclear spins (proton in this experiment) under the microwave irradiation, the electron spin polarization can be transferred to nuclear spins. This is called as Hartmann-Hahn condition ($\gamma_e B_1 = \gamma_H B_0$), where γ_e, γ_H is the gyromagnetic ratio of the electron and proton spin, respectively. B_0 is the external magnetic field, and B_1 is the oscillating magnetic field by microwave irradiation. Note that B_1 is applied perpendicular to B_0, and proportional to the square root of microwave power. Due to the broadening of ESR linewidth by hyperfine coupling and different molecular orientations, only a small fraction of spin packets can satisfy the Hartmann-Hahn condition at a time. One of the solutions of this problem is to use the ISE sequence that sweeps the external magnetic field during the microwave irradiation, so that

more spin packets can be used for the polarization transfer. The transferred polarization is automatically diffused throughout the sample by dipolar interaction between proton spins. By repeating the above sequence, the proton polarization builds up while balancing with the spin-lattice relaxation.

The samples were prepared in a similar way as for the TAS and ESR measurements using a 5-mm ESR tube. To selectively polarize protons of water molecules and extend the spin-lattice relaxation time of ^{1}H, we used a solvent mixture of deuterated glycerol, D_2O, and H_2O in the volume ratio 5:4:1. The DNP sequence shown in Figure. 3-1C was performed with a central magnetic field of 629 mT, the field corresponding to the quintet ESR peak. The sweep range of the magnetic field was about 10 mT (Figure 3-7). We note that different magnetic fields were used for ESR and DNP. ESR was measured at a resonance frequency of 9.0 GHz to compare with common X-band data, while DNP was measured at 17.3 GHz, the frequency at which microwave amplifiers are available as high as possible to increase the T_1 of ^{1}H. Remarkably, an increase in the ^{1}H NMR signal intensity was clearly observed for the NaPDBA-only assemblies and the NaPDBA-γCD complex at a position corresponding to the $^5(TT)_0 \rightarrow {}^5(TT)_1$ ESR peak (Figure 3-37A-D ,3-38). However, this enhancement was not observed in the NaPDBA-βCD complex, which did not show the quintet-derived signal. Since ISE sequence was carried out for 10 μs, the ESR spectrum integrated for 10 μs after photoexcitation was compared to the DNP profile. With NaPDBA and NaPDBA-γCD, signal enhancement of 30% and 46% was observed in the magnetic field (629 mT) corresponding to the quintet ESR peak compared to the magnetic field of 641 mT for NaPDBA and 639 mT for NaPDBA-γCD corresponding to the triplet ESR peak, respectively (Figure 3-37C, D). On the other hand, with NaPDBA-βCD, this ratio was remarkably low (7%), supporting the absence of quintet-induced DNP (Figure 3-37). The emissive enhanced NMR peaks were observed by using emissive quintet ESR peak for NaPDBA and NaPDBA-γCD. Meanwhile, no emissive NMR peak was observed for NaPDBA-βCD at the magnetic field corresponding to the emissive quintet ESR peak. There was an approximate correlation between ESR and DNP profiles, confirming that DNP was performed using triplets and quintets, respectively. Although triplet gave the larger DNP effect than quintet in the present system, it is possible to suppress the formation of triplet by selectively synthesizing dimers, and it would be possible to improve the quintet DNP performance more by selectively generating $^5(TT)_0$ among the quintet sublevels by controlling the orientation of the dimers relative to the magnetic field [21].These results indicate that nuclear hyperpolarization of water molecules was successfully achieved using SF-derived quintet electron polarization for the first time.

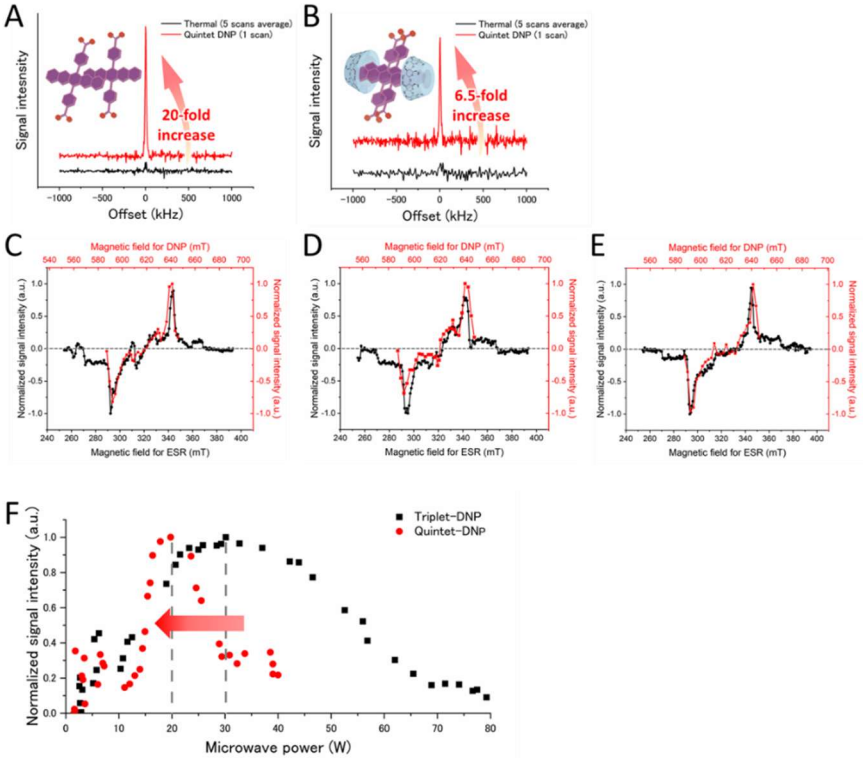

Figure 3-37. DNP using SF-born quintet electron spin polarization.

(A), (B) ^{1}H-NMR signals under thermal conditions (black lines, 5 scans every 10 min) and after quintet-DNP (red lines, ISE sequence for 5 min, 1 scan) of water-glycerol (glycerol-*d*$_8$:D_2O:H_2O = 5:4:1) containing (A) NaPDBA and (B) NaPDBA-γCD at 100 K ([NaPDBA] = 1 mM, [γCD] = 5 mM). The photo-excitation wavelength and frequency were 527 nm and 500 Hz, respectively. DNP was performed by matching the magnetic field to the quintet peaks. The microwave power and frequency were 20 W and 17.30 GHz, respectively, the laser powers were 2.7 W for (A) and 1.5 W for (B). The magnetic field sweep width was 10 μs. Magnetic field dependence of the signal intensity of the ^{1}H NMR by DNP and time-resolved ESR spectra in water-glycerol containing (C) NaPDBA, (D) NaPDBA-γCD, and (E) NaPDBA-βCD ([NaPDBA] = 1 mM, [βCD] = [γCD] = 5 mM). Water-glycerol glass (glycerol-*d*$_8$:D_2O:H_2O = 5:4:1) was used for the DNP measurement at 100 K. ISE sequence for 20 s (C, E) and 30 s (D) and 1 scan; microwave power and frequency were 20 W and 17.25 GHz, respectively; laser power: 1.5 W; magnetic field sweep width: 10 μs. Water-glycerol glass (glycerol:H_2O = 5:5) was used for the time-resolved ESR measurements at 143 K. ESR spectra were integrated for 10 μs after photoexcitation in order to compare the DNP profile with the ISE sequence for 10 μs. (F) Microwave power dependence of DNP enhancement. The gray dashed line indicates the microwave power when the ^{1}H-NMR signal is at its maximum. The red arrow indicates the peak top shift from triplet-DNP to quintet-DNP. Triplet-DNP was performed at 27.4 MHz (ISE sequence for 10 s and 4 scans with a laser power of 2.7 W, microwave frequency of 17.30 GHz and sweep width of 25 μs). Quintet-DNP was performed at 26.9 MHz (ISE sequence for 10 s and 10 scans with a laser power of 2.7 W, microwave frequency of 17.30 GHz and sweep width of 10 μs).

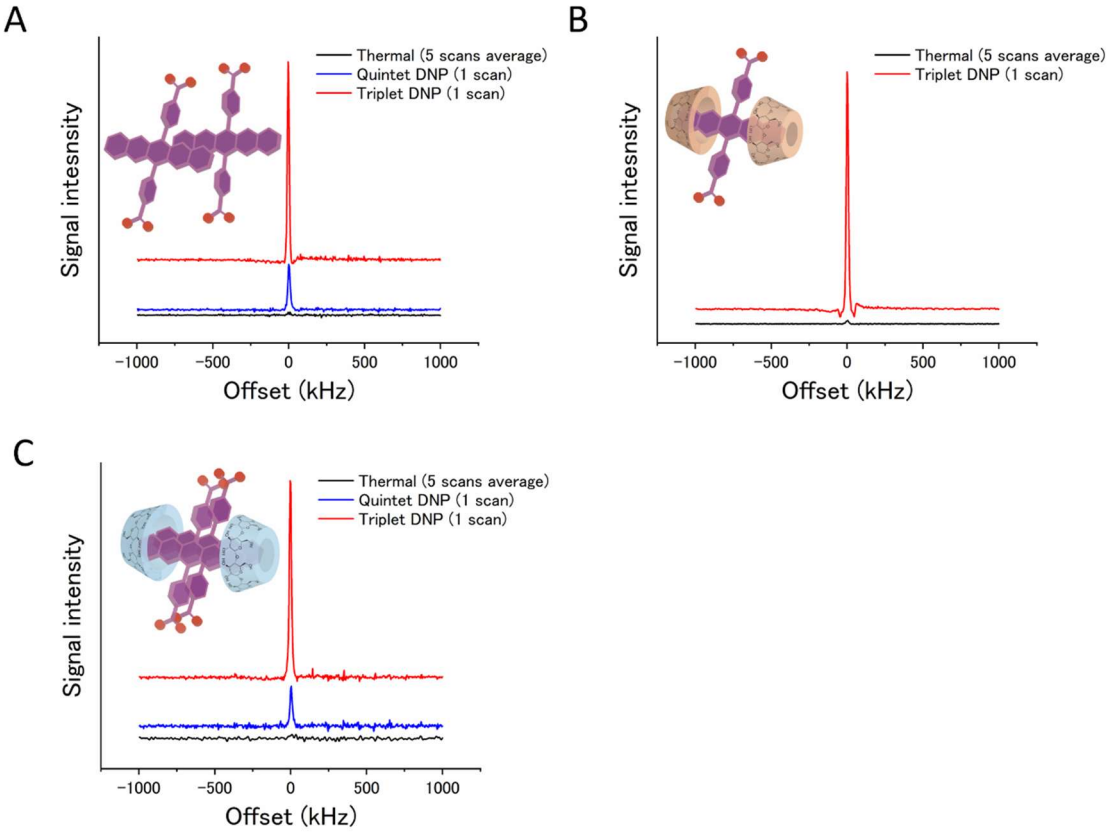

Figure 3-38. ^{1}H-NMR signals of under thermal conditions (black lines, 5 scans every 10 min), after quintet-DNP (blue lines, ISE sequence for 5 min, 1 scan), and after triplet-DNP (red lines, ISE sequence for 5 min, 1 scan) of water-glycerol (glycerol-*d*$_8$:D_2O:H_2O = 5:4:1) containing (A) NaPDBA, (B) NaPDBA-βCD, and (C) NaPDBA-γCD at 100 K ([NaPDBA] = 1 mM, [βCD] = [γCD] = 5 mM). Photo-excitation wavelength and frequency were 527 nm and 500 Hz, respectively. DNP was performed by matching the magnetic field to the triplet (27.4 MHz (A,B), 27.3 MHz (C)) and quintet peaks(26.9 MHz (A, C)), respectively. Microwave power: 40 W (triplet), 20 W(quintet); laser power: 2.7 W (A, B), 1.5 W (C); magnetic field sweep width: 25 μs (triplet), 10 μs (quintet).

The difference in the obtained ^{1}H polarization enhancement depends on several factors including the generation efficiency and polarization ratio, the polarization lifetime, and the spin-lattice relaxation of the nuclear spins around the polarizing agents. In the NaPDBA-only sample, there was a 20-fold enhancement at the quintet ESR peak (Figure 3-37A). A smaller enhancement of 6.5-fold was observed for the NaPDBA-γCD complexes (Figure 3-37B). The signal-to-noise ratio of the ESR spectra of NaPDBA and NaPDBA-γCD is very different, which suggests that the ESR intensity mainly affects the enhancement factor, but

the difference in polarization lifetime may also have an effect. The lower enhancement factor of the NaPDBA-γCD complex was probably due to the triplet deactivation caused by triplet-triplet annihilation (TTA) between neighboring pentacenes, as observed in ns-TAS (Figure 3-28). The fact that the ESR could be fitted using similar rate constants also supports this inference. This indicates the importance of proper arrangement and interaction between pentacene units. Further support for this is that the build-up time was slowed down to the same level as the spin-lattice relaxation time only for the NaPDBA-γCD complex (Figure 3-39, 3-40). This suggests that not enough electron spin polarization was produced for DNP, as shown by the lower ESR signal-to-noise ratio compared with the NaPDBA-only sample, showing that many triplets are deactivated in the strongly interacting pentacene dimer (Figure 3-35A,C).

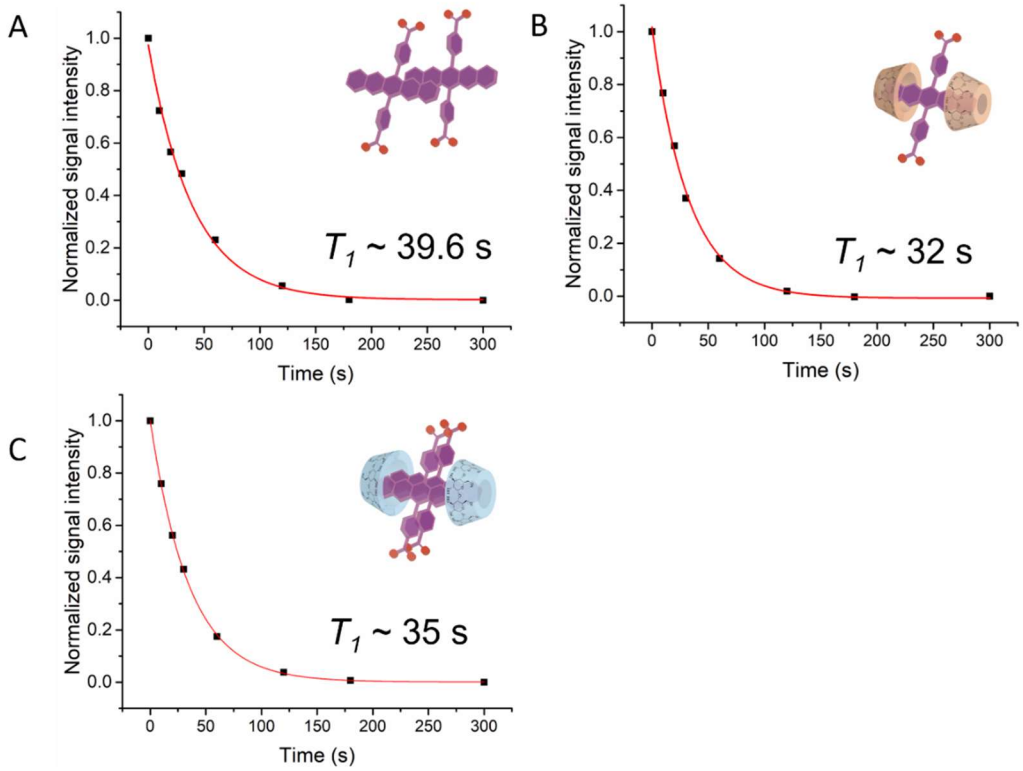

Figure 3-39. Decay of ^{1}H NMR signal after triplet-DNP of water-glycerol (glycerol-d_8:D_2O:H_2O = 5:4:1) containing (A) NaPDBA, (B) NaPDBA-βCD, and (C) NaPDBA-γCD at 100 K ([NaPDBA] = 1 mM, [βCD] = [γCD] = 5 mM). Triplet-DNP was performed at 27.4 MHz (ISE sequence for 30 s and 1 scan; microwave power: 40 W; laser power: 1.5 W; magnetic field sweep width: 25 μs). The results of single-exponential fitting are shown as red lines.

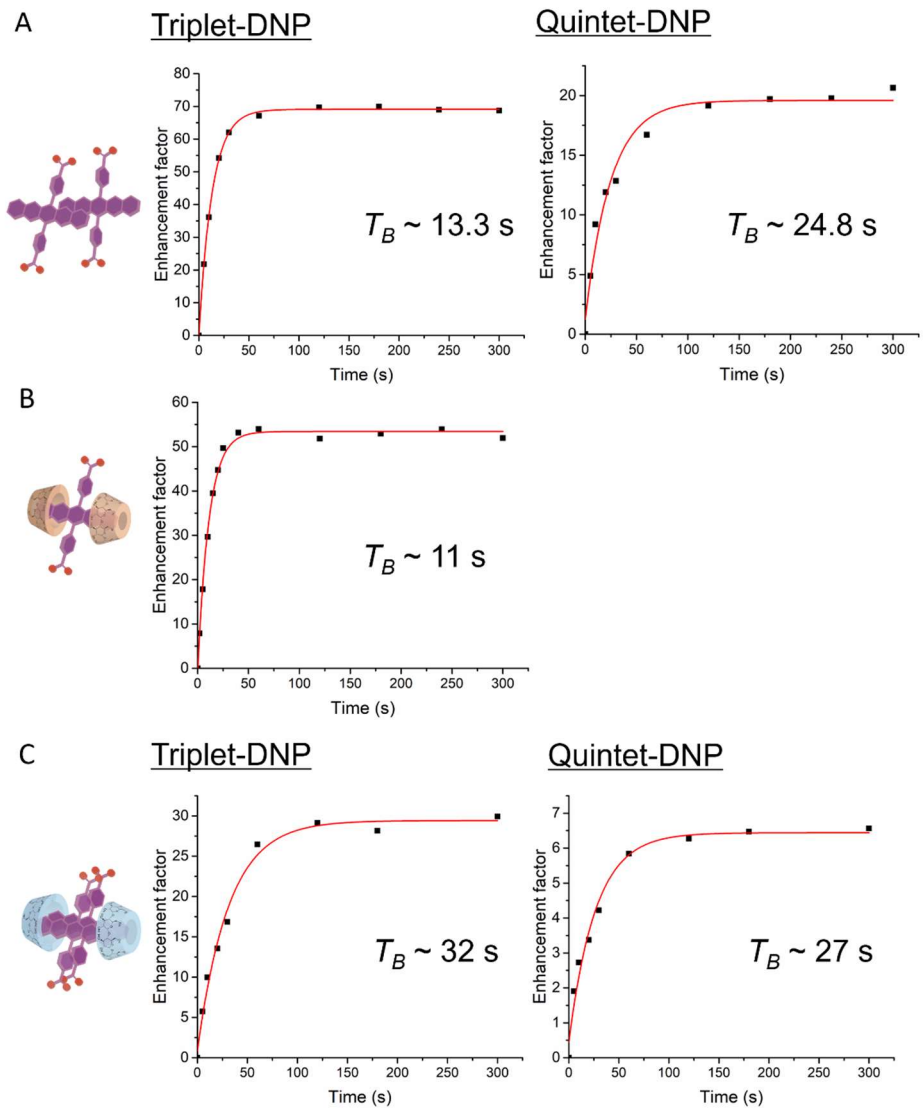

Figure 3-40. Polarization build-up curves of triplet-DNP and quintet-DNP of water-glycerol (glycerol-d_8:D_2O:H_2O = 5:4:1) containing (A) NaPDBA, (B) NaPDBA-βCD, and (C) NaPDBA-γCD at 100 K ([NaPDBA] = 1 mM, [βCD] = [γCD] = 5 mM). Photo-excitation wavelength and frequency were 527 nm and 500 Hz, respectively. Triplet-DNP was performed at 27.4 MHz (A, B) and 27.3 MHz (C) (1 scan; microwave power: 40 W; laser power: 2.7 W (A, B), 1.5 W (C); magnetic field sweep width: 25 μs). Quintet-DNP was performed at 26.9 MHz (1 scan; microwave power: 20 W; laser power: 2.7 W (A, B), 1.5 W(C); magnetic field sweep width: 10 μs). The results of single-exponential fittings are shown as red lines.

We then checked the dependence of the microwave intensity irradiated during the DNP sequence using the quintet and triplet electron spin polarizations (Figure 3-37F). The NMR signal was found to be maximized at a weaker microwave intensity with the quintet than with the triplet. This is because the Rabi frequency of electrons in the quintet state is $\sqrt{3}$ times higher than that in the triplet state [17], and the Hartmann-Hahn condition is accordingly shifted. This result further confirmed that the SF-derived polarized quintet state is successfully utilized for the DNP application.

3-4 Conclusion

In this study, we have demonstrated the potential of SF as a "polarized spin generator" in DNP of water molecules. We have created three supramolecular systems with different interactions between pentacene units using the identical complex of NaPDBA with β/γCD. SF was observed for the NaPDBA-only assemblies and the NaPDBA-γCD complex in water-glycerol glass, where the pentacene skeletons are close to each other. The promising potential of SF as a polarization source was indicated by the preferential population of the $|^5(TT)_0\rangle$ sublevel at a particular resonance magnetic field strength. The magnetic field dependence and microwave intensity dependence of DNP ensure that nuclear polarization was enhanced using quintet-derived polarization. Our findings indicate that the enhancement factor of DNP varies with assembly structure, indicating the direction of further optimizations. The remaining challenge for selective formation of the $^5(TT)_0$ state is to orient the chromophores with respect to the magnetic field, which would be achieved by using an orienting agent or by orienting dispersed nanocrystals [61, 62]. Until now, the application of SF has been mainly limited to the field of energy. This study opens a new potential application of SF to quantum biotechnology, and will accelerate the development of quantum sensing and quantum information science based on the unique multiexcitons exhibited by organic chromophores.

3-5 References

1. M. A. Baldo, D. F. O'Brien, Y. You, A. Shoustikov, S. Sibley, M. E. Thompson and F. S. R., *Nature* 1998, **395**, 151-154.
2. J. J. Burdett, A. M. Muller, D. Gosztola and C. J. Bardeen, *J. Chem. Phys.*, 2010, **133**, 144506.
3. M. B. Smith and J. Mich, *Chem. Rev.*, 2010, **110**, 6891-6936.
4. W.-L. Chan, M. Ligges, A. Jailaubekov, L. Kaake, L. Miaja-Avila and X.-Y. Zhu, *Science*, 2011, **334**, 1541-1545.
5. D. N. Congreve, J. Lee, N. J. Thompson, E. Hontz, S. R. Yost, P. D. Reusswig, M. E. Bahlke, S. Reineke, T. V. Voorhis and M. A. Baldo, *Science*, 2013, **340**, 334-337.
6. S. W. Eaton, L. E. Shoer, S. D. Karlen, S. M. Dyar, E. A. Margulies, B. S. Veldkamp, C. Ramanan, D. A. Hartzler, S. Savikhin, T. J. Marks and M. R. Wasielewski, *J. Am. Chem. Soc.*, 2013, **135**, 14701-14712.
7. A. J. Musser, M. Al-Hashimi, M. Maiuri, D. Brida, M. Heeney, G. Cerullo, R. H. Friend and J. Clark, *J. Am. Chem. Soc.*, 2013, **135**, 12747-12754.
8. S. N. Sanders, E. Kumarasamy, A. B. Pun, M. T. Trinh, B. Choi, J. Xia, E. J. Taffet, J. Z. Low, J. R. Miller, X. Roy, X. Y. Zhu, M. L. Steigerwald, M. Y. Sfeir and L. M. Campos, *J. Am. Chem. Soc.*, 2015, **137**, 8965-8972.
9. G. D. Scholes, *J. Phys. Chem. A*, 2015, **119**, 12699-12705.
10. J. Zirzlmeier, D. Lehnherr, P. B. Coto, E. T. Chernick, R. Casillas, B. S. Basel, M. Thoss, R. R. Tykwinski and D. M. Guldi, *Proc. Natl. Acad. Sci. U. S. A.*, 2015, **112**, 5325-5330.
11. A. A. Bakulin, S. E. Morgan, T. B. Kehoe, M. W. Wilson, A. W. Chin, D. Zigmantas, D. Egorova and A. Rao, *Nat. Chem.*, 2016, **8**, 16-23.
12. K. Miyata, F. S. Conrad-Burton, F. L. Geyer and X. Y. Zhu, *Chem. Rev.*, 2019, **119**, 4261-4292.
13. M. J. Y. Tayebjee, S. N. Sanders, E. Kumarasamy, L. M. Campos, M. Y. Sfeir and D. R. McCamey, *Nat. Phys.*, 2016, **13**, 182-188.
14. L. R. Weiss, S. L. Bayliss, F. Kraffert, K. J. Thorley, J. E. Anthony, R. Bittl, R. H. Friend, A. Rao, N. C. Greenham and J. Behrends, *Nat. Phys.*, 2016, **13**, 176-181.
15. B. S. Basel, J. Zirzlmeier, C. Hetzer, B. T. Phelan, M. D. Krzyaniak, S. R. Reddy, P. B. Coto, N. E. Horwitz, R. M. Young, F. J. White, F. Hampel, T. Clark, M. Thoss, R. R. Tykwinski, M. R. Wasielewski and D. M. Guldi, *Nat. Commun.*, 2017, **8**, 15171.
16. Y. Kobori, M. Fuki, S. Nakamura and T. Hasobe, *J. Phys. Chem. B*, 2020, **124**, 9411-9419.
17. S. L. Bayliss, L. R. Weiss, F. Kraffert, D. B. Granger, J. E. Anthony, J. Behrends and R. Bittl, *Phys. Rev. X*, 2020, **10**, 021070.
18. R. M. Jacobberger, Y. Qiu, M. L. Williams, M. D. Krzyaniak and M. R. Wasielewski, *J. Am. Chem. Soc.*, 2022, **144**, 2276-2283.

19. K. E. Smyser and J. D. Eaves, *Sci. Rep.*, 2020, **10**, 18480.
20. D. Lubert-Perquel, E. Salvadori, M. Dyson, P. N. Stavrinou, R. Montis, H. Nagashima, Y. Kobori, S. Heutz and C. W. M. Kay, *Nat. Commun.*, 2018, **9**, 4222.
21. B. K. Rugg, K. E. Smyser, B. Fluegel, C. H. Chang, K. J. Thorley, S. Parkin, J. E. Anthony, J. D. Eaves and J. C. Johnson, *Proc. Natl. Acad. Sci. U. S. A.*, 2022, **119**, e2201879119.
22. D. A. Hall, D. C. Maus, G. J. Gerfen, S. J. Inati, L. R. Becerra, F. W. Dahlquist and R. G. Griffin, *Science*, 1997, **279**, 930-932.
23. J. H. Ardenkjær-Larsen, B. Fridlund, A. Gram, G. Hansson, L. Hansson, M. H. Lerche, R. Servin, M. Thaning and K. Golman, *Proc. Natl. Acad. Sci. U. S. A.*, 2003, **100**, 10158-10163.
24. S. E. Day, M. I. Kettunen, F. A. Gallagher, D. E. Hu, M. Lerche, J. Wolber, K. Golman, J. H. Ardenkjaer-Larsen and K. M. Brindle, *Nat. Med.*, 2007, **13**, 1382-1387.
25. J. M. Franck, A. Pavlova, J. A. Scott and S. Han, *Prog. Nucl. Magn. Reson. Spectrosc.*, 2013, **74**, 33-56.
26. H. Nonaka, R. Hata, T. Doura, T. Nishihara, K. Kumagai, M. Akakabe, M. Tsuda, K. Ichikawa and S. Sando, *Nat. Commun.*, 2013, **4**, 2411.
27. A. J. Rossini, A. Zagdoun, M. Lelli, A. Lesage, C. Copéret and L. Emsley, *Acc. Chem. Res.*, 2013, **46**, 1942-1951.
28. A. Ajoy, K. Liu, R. Nazaryan, X. Lv, P. R. Zangara, B. Safvati, G. Wang, D.Arnold, G. Li, A. Lin, P. Raghavan, E.Druga, S. Dhomkar, D. Pagliero, J. A. Reimer, D. Suter, C. A. Meriles and A. Pines, *Sci. Adv.*, 2018, **4**, eaar5492.
29. Q. Stern, S. F. Cousin, F. Mentink-Vigier, A. C. Pinon, S. J. Elliott, O. Cala and S. Jannin, *Sci. Adv.*, 2021, **7**, eabf5735.
30. S. J. Nelson, J. Kurhanewicz, D. B. Vigneron, P. E. Z. Larson, A. L. Harzstark, M. Ferrone, M. van Criekinge, J. W. Chang, R. Bok, I. Park, G. Reed, L. Carvajal, E. J. Small, P. Munster, V. K. Weinberg, J. H. Ardenkjær-Larsen, A. P. Chen, R. E. Hurd, L. Odegardstuen, F. J. Robb, J. Tropp and J. A. Murray, *Sci. Transl. Med.*, 2013, **5**, 198ra108.
31. A. Henstra, J. Schmidt, T.-S. Lin and W. T. Wenckebach, *Chem. Phys. Lett.*, 1990, **165**, 6-10.
32. S. Bogatko, P. D. Haynes, J. Sathian, J. Wade, J.-S. Kim, K.-J. Tan, J. Breeze, E. Salvadori, A. Horsfield and M. Oxborrow, *J. Phys. Chem. C*, 2016, **120**, 8251-8260.
33. E. M. M. Del Valle, *Process Biochem.*, 2004, **39**, 1033-1046.
34. S. Fujiwara, M. Hosoyamada, K. Tateishi, T. Uesaka, K. Ideta, N. Kimizuka and N. Yanai, *J. Am. Chem. Soc.*, 2018, **140**, 15606-15610.
35. S. Fujiwara, N. Matsumoto, K. Nishimura, N. Kimizuka, K. Tateishi, T. Uesaka and N. Yanai, *Angew. Chem., Int. Ed.*, 2022, **134**, e202115792.
36. K. Takeda, *J. Magn. Reson.*, 2008, **192**, 218-229.
37. J. Wang, R. M. Wolf, J. W. Caldwell, P. A. Kollman and D. A. Case, *J. Comput. Chem.*, 2004,

25, 1157-1174.

38. H. W. Horn, W. C. Swope, J. W. Pitera, J. D. Madura, T. J. Dick, G. L. Hura and T. Head-Gordon, *J. Chem. Phys.*, 2004, **120**, 9665-9678.
39. C. I. Bayly, P. Cieplak, W. D. Cornell and P. A. Kollman, *J. Phys. Chem.*, 1993, **97**, 10269-10280.
40. H. J. C. Berendsen, J. P. M. Postma, W. F. van Gunsteren, A. DiNola and J. R. Haak, *J. Chem. Phys.*, 1984, **81**, 3684-3690.
41. S. Nosé, *Mol. Phys.*, 1984, **52**, 255-268.
42. M. Parrinello and A. Rahman, *J. Appl. Phys.*, 1981, **52**, 7182-7190.
43. B. Hess, H. Bekker, H. J. C. Berendsen and J. G. E. M. Fraaije, *J. Comput. Chem.*, 1997, **18**, 1463-1472.
44. T. Darden, D. York and L. Pedersen, *J. Chem. Phys.*, 1993, **98**, 10089-10092.
45. S. Yoneda, T. Saito, D. Nakajima and G. Watanabe, *Proteins*, 2021, **89**, 811-818.
46. S. Kumar, D. Bouzida, R. H. Swendsen, P. A. Kollman and J. M. Rosenberg, *J. Comput. Chem.*, 1992, **13**, 1011-1021.
47. J. S. Hub, B. L. de Groot and D. van der Spoel, *J. Chem. Theory Comput.*, 2010, **6**, 3713-3720.
48. F. Würthner, T. E. Kaiser and C. R. Saha-Möller, *Angew. Chem., Int. Ed.*, 2011, **50**, 3376-3410.
49. H. Yamagata, C. M. Pochas and F. C. Spano, *J. Phys. Chem. B*, 2012, **116**, 14494-14503.
50. R. M. Young and M. R. Wasielewski, *Acc. Chem. Res.*, 2020, **53**, 1957-1968.
51. X. Zhao, J. P. O'Connor, J. D. Schultz, Y. J. Bae, C. Lin, R. M. Young and M. R. Wasielewski, *J. Phys. Chem. B*, 2021, DOI: 10.1021/acs.jpcb.1c02476.
52. K. Miyata, Y. Kurashige, K. Watanabe, T. Sugimoto, S. Takahashi, S. Tanaka, J. Takeya, T. Yanai and Y. Matsumoto, *Nat. Chem.*, 2017, **9**, 983-989.
53. A. Mandal, M. Chen, E. D. Foszcz, J. D. Schultz, N. M. Kearns, R. M. Young, M. T. Zanni and M. R. Wasielewski, *J. Am. Chem. Soc.*, 2018, **140**, 17907-17914.
54. J. D. Schultz, J. Y. Shin, M. Chen, J. P. O'Connor, R. M. Young, M. A. Ratner and M. R. Wasielewski, *J. Am. Chem. Soc.*, 2021, **143**, 2049-2058.
55. M. Hasegawa, H. Nagashima, R. Minobe, T. Tachikawa, H. Mino and Y. Kobori, *J. Phys. Chem. Lett.*, 2017, **8**, 1179-1184.
56. Y. Kobori, T. Ako, S. Oyama, T. Tachikawa and K. Marumoto, *J. Phys. Chem. C*, 2019, **123**, 13472-13481.
57. S. Matsuda, S. Oyama and Y. Kobori, *Chem. Sci.*, 2020, **11**, 2934-2942.
58. K. Nishimura, H. Kouno, Y. Kawashima, K. Orihashi, S. Fujiwara, K. Tateishi, T. Uesaka, N. Kimizuka and N. Yanai, *Chem. Commun.*, 2020, **56**, 7217-7232.
59. A. Henstra, P. Ducksen, J. Schmidt and W. T. Wenckebach, *J. Magn. Reson.*, 1988, **77**, 389-

393

60. A. Henstra and W. T. Wenckebach, *Mol. Phys.*, 2008, **106**, 859-871.
61. P. Krebs and E. Sackmann, *J. Magn. Reson.* , 1976, **22**, 359-373.
62. Y. Kaneko, T. Onodera, H. Kasai, S. Okada, H. Oikawa, H. Nakanishi, T. Fukuda and H. Matsuda, *J. Mater. Chem.*, 2005, **15**, 253–255

Chapter4

Conclusion

4-1 Conclusion of all the chapters

The first chapter of this thesis provided an introduction to the principles and research background of the various unique properties of photoexcited triplet state and the various functions such as TTA-UC, triplet-DNP, and singlet fission using these properties. In these fields, many physicists have made great efforts, but there have been limited examples that focuses on supramolecular systems rather than single molecular units to utilize these functions. In this paper, we discuss the concept of applying supramolecular chemistry to these triplet functions to solve various problems involving triplet state.

Chapters 2 describes the supramolecular system that incorporates the functions of TTA-UC. Chapter 2 describes the first TTA-UC from visible light to UV light under practical conditions of air-saturated water. In this system, a dense supramolecular assembly of amphiphilic acceptors, donors, and fatty acids prevents the inactivation of the triplet state by preventing the diffusion of oxygen molecules.

Chapter 3 describes the first example of water molecule hyperpolarization based on electron spin polarization generated by singlet fission. In this system, we focused on the pentacene skeleton, which is used in both triplet-DNP and singlet fission. In triplet-DNP, dispersion of pentacene derivatives is usually required, while in singlet fission, aggregation is required. In this study, the pentacene skeleton, which is insoluble in water, is dispersed in an aqueous solvent by imparting hydrophilicity to it, and the aggregation structure is controlled by the addition of cyclodextrin. The supramolecular assemblies of pentacene derivatives obtained in this way were subjected to ESR measurements in a glass of aqueous solvent, and in addition to the triplet-derived peak, a quintet-derived peak suggestive of a singlet fission was observed. By transferring the electron spin polarization of the triplet and quintet to the nuclear spin of the water molecule by DNP, we succeeded in sensitizing the NMR signal of the water molecule nearly 70-fold. Furthermore, the electron spin Rabi frequency of the quintet is larger than that of the triplet, indicating that DNP can be performed at a weaker microwave intensity than conventional triplet-DNP.

4-2 future remarks

TTA-UC

We have succeeded in solving some of the problems in the practical application of TTA-UC, such as the deactivation of TTA-UC luminescence in the presence of oxygen and the aggregation of donor molecules in solids, by using a supramolecular approach. As typified by donors and acceptors, TTA-UC is a process via multiple components, and therefore, material design based on supramolecular chemistry, which combines and controls multiple molecules, is proved to be effective. The molecular structure of the dye itself is being further studied by many researchers, and materials that exhibit high quantum yields and low I_{th} in various wavelength ranges are being developed. It is expected that the supramolecular chemistry approach will be actively pursued for these materials in the future.

Triplet-DNP

We used a supramolecular approach to disperse pentacene derivatives in aqueous solvents and successfully sensitize the NMR signal of water molecules. The mixture of water and glycerol used in this study is widely used in the bio-application of DNP based on radicals, and this is the first time that triplet-DNP has been successfully applied in this mixture. This is the first time that triplet-DNP has been successfully demonstrated in this solvent mixture. This result is an important advance in the application of triplet-DNP to biological fields such as MRI and protein analysis.

Singlet fission

The supramolecular approach was used to control the aggregation state of pentacene derivatives in aqueous solvents, and the singlet fission was successfully observed. In this system, the electron polarization generated by the singlet fission is evaluated using time-resolved ESR. By using the observed quintet-derived electron polarization for DNP, we succeeded in DNP with weaker microwave intensity than conventional triplet DNP. This result is of great significance for the use of the singlet fission process for DNP. There are very few examples of the application of singlet fission to DNP, and it is expected that the fusion of these fields will be greatly developed in the future.